Cosmogenic Activation of TeO_2 in the Neutrinoless Double-Beta Decay Experiment CUORE

by

Barbara Sue Wang

A dissertation submitted in partial satisfaction of the
requirements for the degree of
Doctor of Philosophy

in

Engineering - Nuclear Engineering

in the

GRADUATE DIVISION
of the
UNIVERSITY OF CALIFORNIA, BERKELEY

Committee in charge:
Professor Eric B. Norman, Chair
Doctor Nicholas D. Scielzo
Professor Yury Kolomensky
Professor Kai Vetter

Spring 2014

Cosmogenic Activation of TeO_2 in the Neutrinoless Double-Beta Decay Experiment CUORE

Abstract

Cosmogenic Activation of TeO_2 in the Neutrinoless Double-Beta Decay Experiment CUORE

by

Barbara Sue Wang
Doctor of Philosophy in Engineering - Nuclear Engineering

University of California, Berkeley

Professor Eric B. Norman, Chair

The Cryogenic Underground Observatory for Rare Events (CUORE) is an experiment that will search for neutrinoless double-beta ($0\nu\beta\beta$) decay of ^{130}Te and other rare processes. Observing $0\nu\beta\beta$ decay would establish that neutrinos are massive Majorana fermions, demonstrate that lepton number is not conserved, and constrain the neutrino mass scale and hierarchy. The CUORE detector, currently being constructed underground at the Gran Sasso National Laboratory in Italy, is an array of 988 high-resolution TeO_2 bolometers. Each bolometer is comprised of a thermistor and a TeO_2 crystal that serves as both the source and the detector of $0\nu\beta\beta$ decay. The $0\nu\beta\beta$ decay signature for ^{130}Te is a peak at the Q-value 2528 keV. Observation of $0\nu\beta\beta$ decay requires that the background at the peak be ultra-low. Background-source identification and characterization are therefore extremely important.

One source of background that is poorly characterized is activation of the TeO_2 crystals by sea-level cosmic-ray neutrons. This process, known as cosmogenic activation, produces long-lived radioisotopes that can obscure the $0\nu\beta\beta$ peak. Existing cross-section data is insufficient to estimate this background; therefore, an additional cross-section measurement has been performed in which a TeO_2 target was irradiated with a neutron-spectrum similar to that of cosmic-ray neutrons at sea-level. Analysis of the radionuclides produced reveals that ^{110m}Ag will dominate the cosmogenic activation background in CUORE. Estimations using the measured cross section for ^{110m}Ag indicate this source will be negligible compared with other contributions to the CUORE background.

To my family

Contents

List of Figures

List of Tables

Acknowledgments

First and foremost, I thank Dr. Eric (Rick) Norman, for his advice, expertise, and insight, as well as for providing a working environment that allowed me to thrive and pursue both theoretical and experimental aspects of nuclear physics in a comfortable and enjoyable setting. I also thank Dr. Nicholas (Nick) Scielzo, who effectively served as my secondary advisor at Lawrence-Livermore National Laboratory (LLNL). Thanks also go to Dr. Kai Vetter and Dr. Yury Kolomensky for their advice and insight as part of my dissertation committee.

I have been exceedingly lucky to have had the opportunity to work with many esteemed professionals and respected colleagues in the field of nuclear physics and detection. My work was made possible through the CUORE Collaboration and the good people at Gran Sasso National Laboratory in Italy. I would particularly like to thank Dr. Maura Pavan for hosting me and providing support. I thank Dr. Silvia Capelli for her advice in my research. I am grateful to Dr. Luca Gironi and colleagues from the University of Milan, Bicocca, for making my stay in Italy enjoyable and fostering an environment that allowed me to learn a great deal more than I could have hoped. Thanks also go to Dr. Alan Smith and Mr. Keenan Thomas of Lawrence-Berkeley National Laboratory (LBL) for providing the gamma-counting facilities and expertise, as well as Dr. Steve Wender of Los Alamos National Laboratory (LANL) for providing the neutron-irradiation capabilities necessary for this study via the accelerator at the Los Alamos Neutron Science Center (LANSCE). Lastly, I thank Dr. Craig Wiegert and Dr. Steven Lewis at the University of Georgia from my undergraduate years for originally exciting me about the prospects of physics.

I am grateful to the University of California, Berkeley, Graduate Division for providing financial support through the Chancellor's Fellowship. I also thank the committee for the Nuclear Forensics Graduate Fellowship for providing me with financial support through my final years at Berkeley. I am also grateful to the Nuclear Science Security Consortium (NSSC) for additional financial support. Thanks also go to the administrative staff at Berkeley for ensuring my term went smoothly. I especially thank Ms. Lisa Zemelman for her guidance.

Finally, I thank my family and close friends that have supported me over the years. In particular, I am grateful to Susan Chung and Amy Coffer for providing emotional support and the necessary breaks from the constant stress of graduate life. I thank my parents for their love and support. My father, Chris Wang, continues to foster an environment in which I can vigorously question and search for answers, and my mother, Sue Wang, has always anchored me when I strayed too far, constantly going further than necessary to make my life easier. Lastly, I thank my domestic partner, Manuel Thomas Aldan, for continuously providing support where I need it most, and for providing a forum where we can both grow and become better people together.

Chapter 1

Introduction

In 1930, W. Pauli postulated the existence of a new electrically neutral particle as a "desperate remedy" to the apparent nonconservation of energy in beta decay. This particle was also theorized to be weakly interacting and extremely light, or massless, making it particularly elusive and difficult to study experimentally. In 1933, E. Fermi named the particle the "neutrino" and included it in his theory of beta decay. It was not until 1956 that neutrinos were first observed in an experiment by C. Cowan and F. Reines that looked for neutrinos (or more specifically, antineutrinos) from a nuclear reactor. Since that time, great strides have been made in characterizing neutrinos; however, major questions about their nature still remain.

Currently, one of the most pertinent questions is whether the neutrino is a Dirac particle or a Majorana particle. A Dirac particle is distinct from its own antiparticle, whereas a Majorana particle is identical to its own antiparticle. The ability to distinguish between the two types depends on the masses of neutrinos. If neutrinos are massless there is no physical difference between the Dirac and the Majorana cases. On the other hand, if neutrinos are massive, their Dirac or Majorana nature can be deduced [1].

Recent experiments detecting neutrino fluxes from the sun, the atmosphere, nuclear reactors, and particle accelerators have provided convincing evidence of neutrino oscillation, the transformation of one neutrino flavor (electron, muon, or tau) into another. Oscillation is a consequence of neutrinos having non-zero mass, and its observation has put the issue of whether neutrinos are Dirac or Majorana particles at the forefront of particle and nuclear physics. The only practical way to answer this question is to search for a second-order nuclear weak process known as double-beta decay. In the most studied form of this decay, a nucleus (A, Z) transitions to a nucleus $(A, Z+2)$ with the emission of two electrons. This decay is allowed by the Standard Model if two electron (anti)neutrinos are also emitted in the transition: $(A, Z) \rightarrow (A, Z+2) + 2e^- + 2\bar{\nu}_e$. This process, known as two-neutrino double-beta ($2\nu\beta\beta$) decay, was first observed in 1987 for ^{82}Se [2] and has since been seen for 11 different isotopes [3, and references therein]. If (and only if) neutrinos are massive Majorana particles, then another decay mode is possible in which the two electron (anti)neutrinos are not emitted: $(A, Z) \rightarrow (A, Z+2) + 2e^-$. This mode, known as neutrinoless double-beta ($0\nu\beta\beta$) decay, violates lepton-number conservation by two units and is therefore not allowed by the Standard Model. Observation of $0\nu\beta\beta$ decay would prove that neutrinos are Majorana particles, as well as show that lepton number is not conserved.

In addition to probing the particle nature of neutrinos, searching for $0\nu\beta\beta$ decay

can also help answer fundamental questions about the masses of neutrinos. Current theory states that the three neutrino flavor eigenstates ν_e, ν_μ, and ν_τ are superpositions of the three neutrino mass eigenstates ν_1, ν_2, and ν_3 that have definite masses of m_1, m_2, and m_3, respectively. Neutrino oscillation experiments and direct neutrino-mass measurements have been able to measure mass differences and set mass limits; however, they have been unable to pin down the exact values of the masses as well as their ordering, or hierarchy. Of particular interest is whether the masses follow the normal hierarchy, i.e., $m_1 < m_2 << m_3$, or the inverted hierarchy, i.e., $m_3 << m_1 < m_2$. It turns out that measuring or setting a limit on the $0\nu\beta\beta$ decay half-life will provide a constraint on the neutrino masses and hierarchy.

The Cryogenic Underground Observatory for Rare Events (CUORE) is one of the leading next-generation $0\nu\beta\beta$ decay experiments. It is currently being constructed underground at the Gran Sasso National Laboratory (LNGS) in Gran Sasso, Italy, and it plans to start operation by the end of 2014. CUORE seeks to observe $0\nu\beta\beta$ decay of ^{130}Te, i.e., $^{130}\text{Te} \rightarrow {}^{130}\text{Xe} + 2e^-$, using an array of 988 high-resolution, low-background cryogenic bolometers. Each bolometer consists of an unenriched $5 \times 5 \times 5$ cm^3 TeO_2 crystal with a thermal sensor attached to one of the surfaces. In total, the crystals contain 206 kg of ^{130}Te and serve as both sources and detectors of $0\nu\beta\beta$ decay. The crystals are enclosed in copper frames that are cooled to approximately 10 mK. The frames serve as both mechanical supports and a thermal bath for the crystals. When a particle interaction occurs in a crystal, the resulting temperature rise is measured by the thermal sensor and used to obtain the energy deposition in the crystal.

In $0\nu\beta\beta$ decay, all of the decay energy, or Q-value, goes to the two electrons and the recoil nucleus. In CUORE, the three particles will be captured in a crystal approximately 87% of the time [4], resulting in an energy deposition equivalent to the full Q-value. The Q-value for ^{130}Te is 2528 keV [5], and therefore, the signature of $0\nu\beta\beta$ decay in CUORE is a peak at 2528 keV. Because $0\nu\beta\beta$ decay is expected to be extremely rare, it is essential that background sources that can mimic the decay signal be minimized. CUORE is aiming for a 1σ $0\nu\beta\beta$ decay half-life sensitivity of 1.6×10^{26} y [4], which can be obtained with a background rate of 10^{-2} counts/(keV·kg·y) at the decay peak and a live-time of five years.

Achieving and maintaining a sufficiently low background rate requires comprehensive knowledge of all possible background sources. The CUORE Collaboration has successfully identified and analyzed a number of these [6–8]; however there are still a few sources that require further study. One of these is activation of the TeO_2 crystals by sea-level cosmic-ray neutrons. This process, known as cosmogenic activation, occurs while the crystals are transported by ship from their production site in Shanghai, China to the experiment site at LNGS. The radioisotopes produced during this time constitute an intrinsic contamination in the crystals that cannot be removed or shielded during counting. Any radioisotopes with long half-lives and Q-values greater than 2528 keV will be problematic because they will still be present when CUORE begins counting and they can contribute events to the $0\nu\beta\beta$ decay peak. A detailed study of the cosmogenic activation background is therefore essential.

For CUORE, focus has been placed on cosmogenic neutrons because at sea-level, activation is primarily caused by the hadronic component of the cosmic-ray flux, which is dominated by neutrons [9]. The impact of crystal activation on CUORE can be understood by examining the production rates of all radioisotopes that can be cosmogenically

produced in TeO_2. This task requires reliable cross sections that span a wide range of energies, from thermal up to several GeV. Experimentally measured cross-section data is currently sparse for the interactions of interest. Some data exist for neutron interactions with individual tellurium isotopes; however, only neutron energies up to approximately 20 MeV have been previously studied [10]. From 800 MeV to tens of GeV, measured proton-activation data exist for natural tellurium [11]. This information can be used for neutron studies because at such high energies (i.e., much greater than the Coulomb barrier between a proton and a nucleus), activation cross sections for neutrons and protons are approximately equal. For the intermediate energies between 20 MeV and 800 MeV, no cross-section measurements have been performed. Some of the cross sections in this region can be evaluated using computer codes such as ACTIVIA [12], YIELDX, and COSMO, which are based on semiemperical formulas by Silberberg and Tsao [13,14]. Although these codes are meant for proton interactions with nuclei, at proton energies $\gtrsim$100 MeV, the calculated cross sections can be assumed equivalent to those for neutrons. For activation of tellurium, these codes are limited, however. The calculated cross sections have typically been within a factor 2 of the measured values for proton energies 800 MeV and higher [11]. Additional cross-section measurements are therefore needed to cover the intermediate energy region, and the results can be used to further benchmark the calculations.

At the end of February 2012, a sample of TeO_2 powder was brought to the Los Alamos Neutron Science Center (LANSCE) and irradiated with a "white" neutron beam with energies 0-800 MeV that resembles the cosmic-ray neutron flux. Following the exposure, the sample was sent to Lawrence Berkeley National Laboratory's Low Background Facility and gamma-counted with a high-purity germanium detector. Cross-sections averaged over the neutron spectrum were obtained with the data. These were used to calculate radionuclide-production rates during transportation of the TeO_2 crystals from Shanghai to LNGS.. The rates were then combined with Monte Carlo simulations of the CUORE detector to get an estimate of the background contribution in CUORE from crystal activation.

This dissertation describes the cross-section measurement carried out at LANSCE (Chapter 5) and explains the background analysis performed to investigate the impact cosmogenic activation of TeO_2 will have on CUORE (Chapter 6). Before delving into the details, I will first discuss neutrinos (Chapter 2), double-beta decay (Chapter 3), the CUORE detector (Chapter 4), and the various background sources in CUORE (Chapter 4). Conclusions are provided in Chapter 7.

Chapter 2

Neutrinos

A neutrino is an electrically neutral, spin-1/2 particle that interacts only through the weak and gravitational forces. In the Standard Model of particle physics, there are three left-handed neutrinos, ν_{eL}, $\nu_{\mu L}$, and $\nu_{\tau L}$, that are respectively coupled to the three charged leptons e, μ, and τ via a W boson. Each neutrino also has a right-handed antineutrino associated with it: $\bar{\nu}_{eR}$, $\bar{\nu}_{\mu R}$, and $\bar{\nu}_{\tau R}$, respectively. In the Standard Model, no right-handed neutrinos (or left-handed antineutinos) exist, which results in neutrinos being theoretically massless [1]. Recent experiments have demonstrated, however, that neutrinos are not massless. Observations of neutrino oscillations, discussed in Section 2.1, suggest that at least two neutrinos have nonzero mass. The existence of massive neutrinos has lead to the question of whether neutrinos are Dirac particles ($\nu \neq \bar{\nu}$) or Majorana particles ($\nu = \bar{\nu}$).

2.1 Neutrino oscillations

Neutrinos can be expressed in terms of mass eigenstates $|\nu_i\rangle$ that have definite masses m_i. A consequence of neutrinos having mass is the possibility for neutrinos to oscillate from one flavor (e, μ, or τ) into another. Oscillation occurs because the flavor eigenstates ν_l can be expressed as linear combinations of mass eigenstates:

$$|\nu_l\rangle = \sum_{i=1}^{n} U_{li}^{*} |\nu_i\rangle , \qquad l \in \{e, \mu, \tau\} , \tag{2.1}$$

where n is the number of light neutrino-mass-eigenstates and U is known as the Pontecorvo-Maki-Nakagawa-Sakata (PMNS) mixing matrix. The value of n is generally taken to be 3 (for three light mass-eigenstates ν_1, ν_2, ν_3 with distinct and definite masses m_1, m_2, m_3, respectively), which means that U can be written as a 3×3 matrix:

$$U = \begin{pmatrix} c_{12}c_{13} & s_{12}c_{13} & s_{13}e^{-i\delta} \\ -s_{12}c_{23} - c_{12}s_{23}s_{13}e^{i\delta} & c_{12}c_{23} - s_{12}s_{23}s_{13}e^{i\delta} & s_{23}c_{13} \\ s_{12}s_{23} - c_{12}c_{23}s_{13}e^{i\delta} & -c_{12}s_{23} - s_{12}c_{23}s_{13}e^{i\delta} & c_{23}c_{13} \end{pmatrix} \begin{pmatrix} e^{i\alpha_1/2} & 0 & 0 \\ 0 & e^{i\alpha_2/2} & 0 \\ 0 & 0 & 1 \end{pmatrix} , \tag{2.2}$$

where s_{ij} and c_{ij} refer to $\sin(\theta_{ij})$ and $\cos(\theta_{ij})$. The mixing matrix contains six parameters: the mixing angles θ_{12}, θ_{23}, and θ_{13}; a CP-violating phase δ; and two Majorana phases α_1 and α_2. The phases α_1 and α_2 have physical consequences only if neutrinos are Majorana particles and can participate in processes that violate lepton number.

The first signs of neutrino oscillation were observed by R. Davis in the Homestake Experiment that ran from 1970 until 1994. Davis was using the inverse beta-decay reaction $\nu_e + {}^{37}\mathrm{Cl} \to {}^{37}\mathrm{Ar} + e^-$ to measure the total (electron-)neutrino flux produced by the sun. The experiment ended up detecting only about one-third of the flux predicted by solar models. This discrepancy became known as the *solar neutrino problem* and was confirmed by many subsequent radiochemical [15, 16] and water Cherenkov [17] experiments. Experiments looking at neutrinos produced in the atmosphere observed a similar phenomenon. For example, the Kamiokande II detector measured the ratio of muon neutrinos to electron neutrinos, ν_μ/ν_e, and compared it with the ratio predicted by theory. The results indicated a deficit in the measured number of muon neutrinos. This deficit in addition to the one observed for solar neutrinos hinted that the neutrinos were oscillating into other flavors before reaching the detectors.

The first experimental evidence for (atmospheric-)neutrino oscillations was announced by the Super-Kamiokande (SK) Collaboration in 1998. In addition to measuring the ν_μ/ν_e ratio, they also compared the flux of upward-going neutrinos to that of downward-going neutrinos. The results differed significantly from prediction when neutrino oscillations were ignored, but agreed well with prediction when two-flavor $\nu_\mu \leftrightarrow \nu_\tau$ oscillations were considered.

In 2001, the Sudbury Neutrino Observatory (SNO) solved the solar neutrino problem by providing clear evidence of neutrino oscillations. SNO was the first experiment that could detect all three flavors of neutrinos. It could also distinguish electron neutrinos from muon and tau neutrinos, but could not distinguish muon and tau neutrinos from each other. The SNO detector was a water Cherenkov detector that used heavy water, $\mathrm{D_2O}$, as the target. It was sensitive to three different interactions:

$$\begin{aligned} \nu_e + d &\to p + p + e^- && \text{(charged current, CC)}, \\ \nu_l + d &\to p + n + \nu_l && \text{(neutral current, NC)}, \\ \nu_l + e^- &\to \nu_l + e^- && \text{(elastic scattering, ES)}, \end{aligned}$$

where $l \in \{e, \mu, \tau\}$. The CC interaction is sensitive only to electron neutrinos; the NC interaction is equally sensitive to all three neutrino flavors; and the ES interaction is sensitive to all flavors, but is dominated by electron neutrinos. The total flux from all neutrino flavors was measured using the NC interactions. The flux obtained agreed well with the value predicted by solar models for ν_e production in the sun. Combined with the reduced flux observed for ν_e, the NC results demonstrate that electron neutrinos produced in the sun oscillate into other flavors while traveling to the earth.

In most analyses of neutrino oscillation experiments, it has been assumed that only two neutrino flavors participate in mixing instead of three. If there are only two flavors, α and β, the corresponding states ν_α and ν_β can be expressed as linear combinations of two mass states ν_i and ν_j with masses m_i and m_j. The probabilities for flavor mixing and flavor survival over a distance L are then given by

$$P(\overset{(-)}{\nu}_\alpha \to \overset{(-)}{\nu}_\beta) = \sin^2 2\theta \sin^2 \left(1.27 \Delta m^2 \frac{L}{E} \frac{\mathrm{GeV}}{\mathrm{eV^2 km}} \right), \qquad \beta \neq \alpha \tag{2.3}$$

and

$$P(\overset{(-)}{\nu}_\alpha \to \overset{(-)}{\nu}_\alpha) = 1 - \sin^2 2\theta \sin^2 \left(1.27 \Delta m^2 \frac{L}{E} \frac{\mathrm{GeV}}{\mathrm{eV^2 km}} \right), \tag{2.4}$$

respectively, where θ is the mixing angle, E is the neutrino energy, and $\Delta m^2 \equiv m_i^2 - m_j^2$.

The Kamioka Liquid scintillator Anti-Neutrino Detector (KamLAND) in central Japan provided further direct evidence of neutrino oscillations by actually measuring the electron-antineutrino survival-probability as a function of L/E. The antineutrinos came from 55 Japanese nuclear power plants and were detected using the inverse beta-decay reaction $\bar{\nu}_e + p \rightarrow e^+ + n$, which has a 1.8 MeV threshold. The results are shown in Figure 2.1. The parameter $E_{\bar{\nu}_e}$ in the plot is the antineutrino energy and L_0 is the average distance between the KamLAND detector and the nuclear power plants; L_0 was determined to be 180 km. The data agrees well with the expectation based on neutrino oscillations.

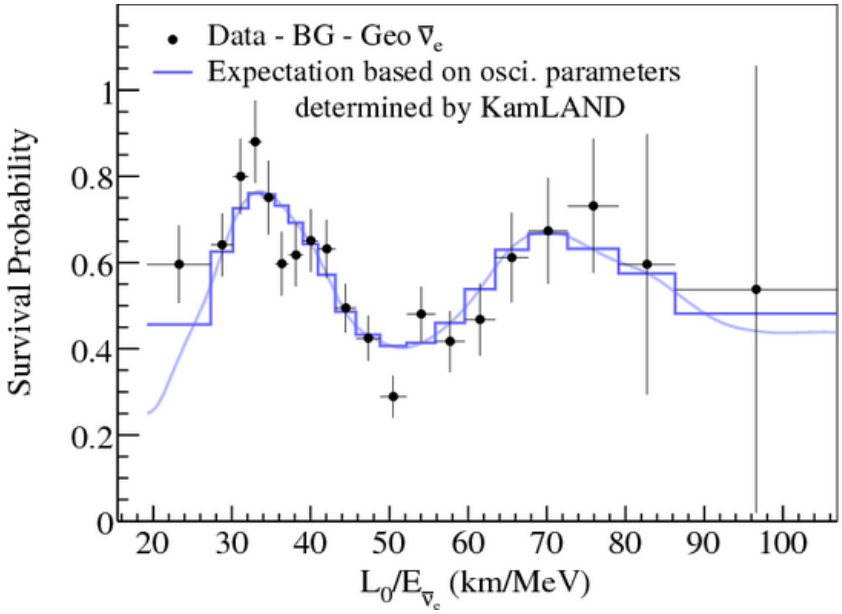

Figure 2.1: Neutrino-oscillation results from KamLAND. Figure was taken from Ref. [18].

Collectively, oscillation experiments have been able to measure the following parameters of neutrino mixing: two mass splittings, $\delta m^2 \equiv m_2^2 - m_1^2$ and $\Delta m^2 \equiv m_3^2 - (m_1^2 + m_2^2)/2$, and three mixing angles, θ_{12}, θ_{23}, and θ_{13}. Solar neutrino experiments together with KamLAND are sensitive to δm^2 and θ_{12}. Atmospheric neutrino experiments, such as SK, along with long-baseline accelerator experiments, including K2K ($\nu_\mu \rightarrow \nu_\tau$ oscillation) [19] and MINOS ($\nu_\mu \rightarrow \nu_\mu$ survival) [20], give the parameters $|\Delta m^2|$ and θ_{23}. Finally, θ_{13} has been measured by two recent short-baseline reactor experiments Daya Bay [21] and RENO [22], which both obtained θ_{13} by looking at the survival probability of electron antineutrinos from nuclear reactors. Measured values of the mixing parameters, obtained from a global analysis [23] of the experiments discussed above, are presented in Table 2.1.

At the moment, oscillation experiments have not been able to determine the sign of the mass splitting Δm^2. Thus, there are two possible hierarchies for the neutrino masses: the normal hierarchy (NH), if $\Delta m^2 > 0$, and the inverted hierarchy (IH), if $\Delta m^2 < 0$; both are illustrated in Figure 2.2. Also indicated in the figure by two question marks is the fact that the values of the masses m_1, m_2, and m_3 are not known. Constraints on the masses have been obtained from direct neutrino-mass measurements and from cosmological data. One constraint comes from the Troitsk tritium beta-decay experiment [24]:

$$m_{\bar{\nu}_e} < 2.05 \text{ eV}, \qquad 95\%\text{C.L.}, \tag{2.5}$$

where the electron antineutrino mass, $\bar{\nu}_e$, is a linear combination of m_1, m_2, and m_3. Another constraint is produced by combining the Cosmic Microwave Background data of the WMAP experiment with supernovae and galaxy-clustering data [25]. Depending on the model used, the following is obtained for the sum of the definite neutrino masses [25]:

$$\sum_{i=1}^{3} m_i \lesssim (0.3 - 1.3)\ \text{eV}, \qquad 95\%\text{C.L.} \tag{2.6}$$

The neutrino hierarchy also affects the mixing parameters; the values will be slightly different depending on whether the NH or the IH is assumed. These differences are indicated in Table 2.1.

Table 2.1: Measured values of neutrino mixing parameters from the global three-neutrino oscillation analysis of Ref. [23]. The results are shown for both the normal hierarchy (NH) and the inverted hierarchy (IH).

Parameter	Best fit	1σ confidence interval
δm^2 (NH or IH)	7.54×10^{-5} eV^2	$(7.32 - 7.80) \times 10^{-5}$ eV^2
$\lvert\Delta m^2\rvert$ (NH)	2.43×10^{-3} eV^2	$(2.33 - 2.49) \times 10^{-3}$ eV^2
$\lvert\Delta m^2\rvert$ (IH)	2.42×10^{-3} eV^2	$(2.31 - 2.49) \times 10^{-3}$ eV^2
$\sin^2\theta_{12}$ (NH or IH)	0.307	$0.291 - 0.325$
$\sin^2\theta_{23}$ (NH)	0.386	$0.365 - 0.410$
$\sin^2\theta_{23}$ (IH)	0.392	$0.370 - 0.431$
$\sin^2\theta_{13}$ (NH)	0.0241	$0.0216 - 0.0266$
$\sin^2\theta_{13}$ (IH)	0.0244	$0.0219 - 0.0267$

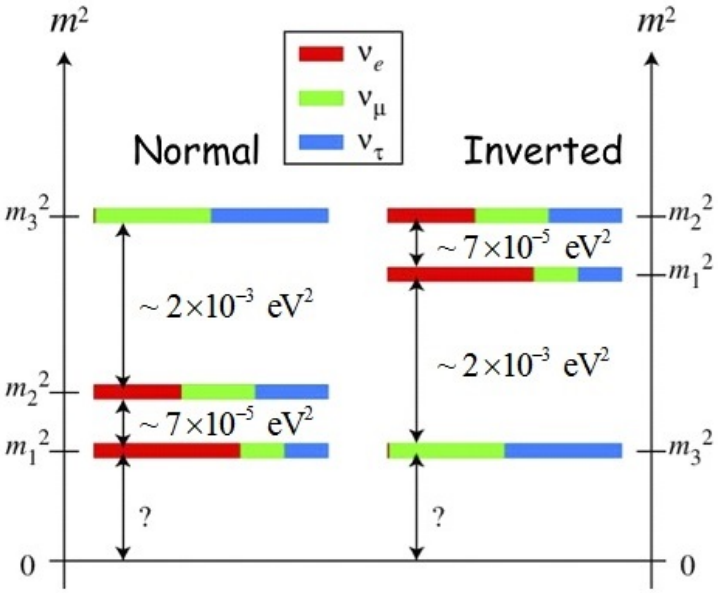

Figure 2.2: Two orderings of the neutrino masses are possible depending on the sign of Δm^2: the normal hierarchy (left) and the inverted hierarchy (right). The two question marks in the figure indicate that the values of the masses are currently unknown. The three colors red, green, and blue correspond to the neutrino flavors e, μ, and τ, respectively, and are used to illustrate the flavor mixing that occurs for each mass eigenstate.

Chapter 3

Double-beta decay

Double-beta ($\beta\beta$) decay is an extremely rare second-order weak process in which a nucleus (A, Z) transitions to a nucleus $(A, Z \pm 2)$. According to the Standard Model, this decay can theoretically occur in the following ways:

(1) with the emission of two electrons and two electron antineutrinos,
(2) with the emission of two positrons and two electron neutrinos (if the Q-value is at least 2.044 MeV, i.e., four electron masses),
(3) with the capture of two atomic electrons and the emission of two electron neutrinos (also known as double-electron capture), and
(4) with the capture of one atomic electron and the emission of one positron and two electron neutrinos (if the Q-value is at least 1.022 MeV, i.e., two electron masses).

Modes (2) and (4) have not yet been seen experimentally, and Mode (3) has been inferred for ^{130}Ba using geochemical methods [26]. Mode (1), also known as two-neutrino double-beta ($2\nu\beta\beta$) decay, is by far the most studied form of $\beta\beta$ decay. $2\nu\beta\beta$ decay and its lepton-number-violating form, neutrinoless double-beta decay, will be the focus of the rest of this chapter.

3.1 Two-neutrino and neutrinoless double-beta decay

Two-neutrino double-beta decay was first predicted in a paper by Maria Goeppert-Mayer in 1935 [27] and has since been observed for 11 different isotopes [3, and references therein]. Figure 3.1a shows the $2\nu\beta\beta$ decay Feynman diagram, which can be interpreted as two simultaneous single-beta decays. $2\nu\beta\beta$ decay can occur as long as the nucleus $(A, Z + 2)$ is lighter than the nucleus (A, Z). However, if single-beta decay to $(A, Z + 1)$ is also energetically allowed, as is the case for odd-A nuclei (Figure 3.2a), then measuring $2\nu\beta\beta$ decay will be practically impossible because of the overwhelming background rate from single-beta decay. Therefore, an ideal candidate for $2\nu\beta\beta$ decay studies is an isotope for which the transition to $(A, Z+1)$ is energetically forbidden. This criterion is satisfied by any even-even nucleus that, due to the nuclear pairing force, is lighter than the odd-odd $(A, Z + 1)$ nucleus (Figure 3.2b). ^{130}Te, used in the CUORE experiment, is one such isotope, and its decay scheme is given in Figure 3.3. Other possible candidates

are isotopes such as ^{48}Ca for which single-beta decay is energetically allowed but greatly suppressed because of a large change in nuclear spin during the decay.

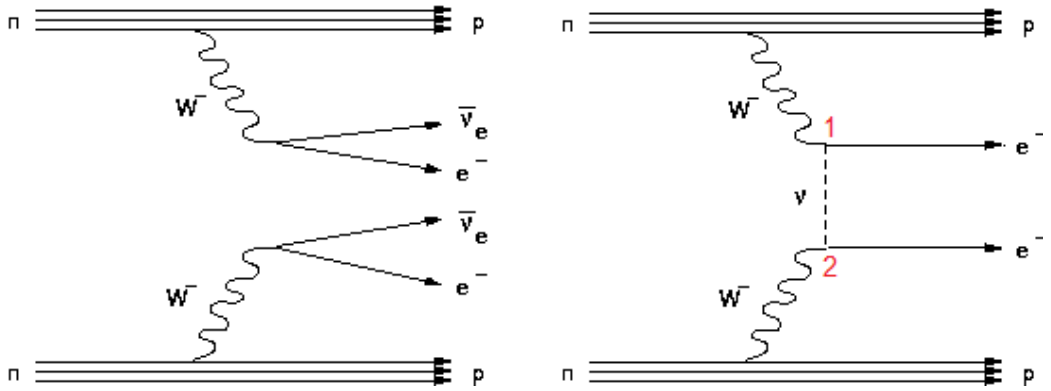

(a) Two neutrino double-beta decay.

(b) Neutrinoless double-beta decay.

Figure 3.1: Two possible modes for double-beta decay.

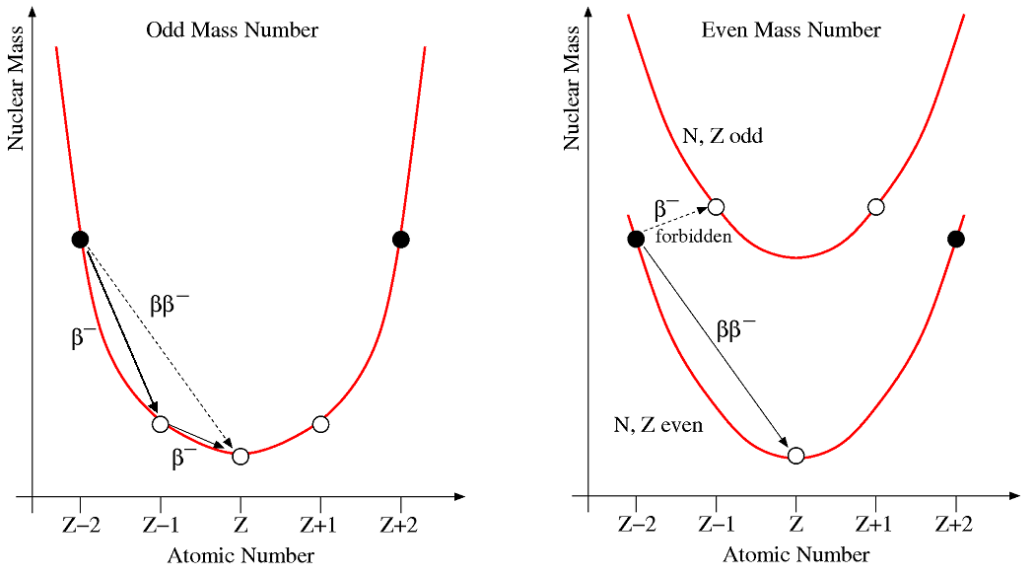

(a) Nuclear mass versus atomic number for odd-A nuclei.

(b) Nuclear mass versus atomic number for even-A nuclei.

Figure 3.2: In plot (a), both single-beta decay and double-beta decay from the Z-2 state are energetically allowed. In this case, the single-beta decay rate will be too overwhelming to practically observe double-beta decay. In plot (b), single-beta decay to the Z-1 state is not energetically allowed; however, double-beta decay to the Z state is. This scenario is ideal for observing double-beta decay.

Since $2\nu\beta\beta$ decay is second-order in the weak interaction, nuclei that undergo the transition have very long half-lives, on the order of $10^{19} - 10^{24}$ years. Measured $2\nu\beta\beta$ decay partial half-lives are given in Table 3.1 for several isotopes [29, 30]. The values listed come from direct measurements of the decay as well as from geochemical and radiochemical experiments.

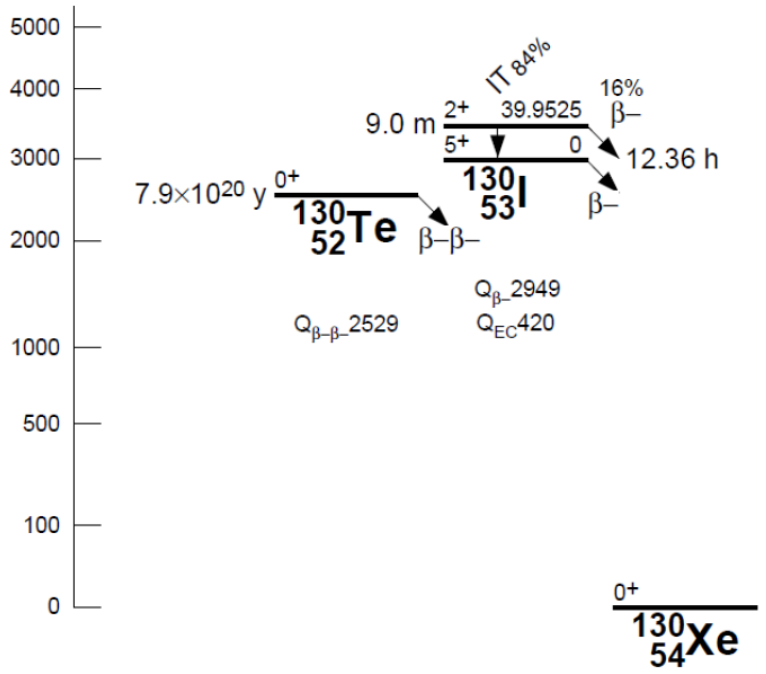

Figure 3.3: Decay scheme for ^{130}Te double-beta decay [28].

Table 3.1: Measured $2\nu\beta\beta$ decay partial half-lives [29, 30].

Nuclide	$T_{1/2}^{2\nu\beta\beta}$ (y)
^{48}Ca	$4.4^{+0.6}_{-0.5} \times 10^{19}$
^{76}Ge	$(1.5 \pm 0.1) \times 10^{21}$
^{82}Se	$(9.2 \pm 0.7) \times 10^{19}$
^{96}Zr	$(2.3 \pm 0.2) \times 10^{19}$
^{100}Mo	$(7.1 \pm 0.4) \times 10^{18}$
^{116}Cd	$(2.8 \pm 0.2) \times 10^{19}$
^{128}Te	$(1.9 \pm 0.4) \times 10^{24}$
^{130}Te	$6.8^{+1.2}_{-1.1} \times 10^{20}$
^{136}Xe	$(2.38 \pm 0.14) \times 10^{21}$
^{150}Nd	$(8.2 \pm 0.9) \times 10^{18}$
^{238}U	$(2.0 \pm 0.6) \times 10^{21}$

If and only if neutrinos are massive Majorana fermions, then another mode of double-beta decay is possible in which the two neutrinos from $2\nu\beta\beta$ decay are not emitted, i.e., $(A, Z) \rightarrow (A, Z+2) + 2e^-$. This transition, known as neutrinoless double-beta ($0\nu\beta\beta$) decay, is a lepton-number-violating process and therefore not allowed by the Standard Model. No experiment has yet observed $0\nu\beta\beta$ decay, except for one controversial claim of discovery by a subset of the HEIDELBERG-MOSCOW Collaboration [31]. From the Feynman diagram in Figure 3.1b, one can view the transition as two simultaneous single-beta decays where the two electron antineutrinos (emitted at vertices 1 and 2 in the diagram), being their own antiparticles, pair annihilate with each other and transfer the energy to the two electrons. Another interpretation would be that an antineutrino is produced at vertex 1 in the diagram and absorbed as a neutrino at vertex 2.

The $0\nu\beta\beta$ decay rate is obtained using Fermi's Golden Rule and can be written as [32]

$$\frac{1}{T_{1/2}^{0\nu\beta\beta}} = G_{0\nu\beta\beta}(Q, Z)|M_{0\nu\beta\beta}|^2 \langle m_{\beta\beta}\rangle^2 , \tag{3.1}$$

where $T_{1/2}^{0\nu\beta\beta}$ is the partial half-life for $0\nu\beta\beta$ decay; $G_{0\nu\beta\beta}(Q, Z)$ is a phase-space factor that is a function of the Q-value, Q, and the number of protons, Z; $M_{0\nu\beta\beta}$ is a nuclear matrix element (NME) representing the overlap between the initial and final nuclear states; and $\langle m_{\beta\beta}\rangle$, called the "effective" Majorana mass, is a linear combination of the neutrino masses:

$$\langle m_{\beta\beta}\rangle \equiv \left| \sum_{i=1}^{3} U_{ei}^2 m_i \right| , \tag{3.2}$$

where U is the PMNS mixing matrix from Equations 2.1 and 2.2. The factor $G_{0\nu\beta\beta}$ is calculable and is proportional to Q^5. The NME $M_{0\nu\beta\beta}$ is obtained using computational methods based on nuclear structure theory. The large number of particles in any double-beta decaying nucleus makes the exact evaluation of a NME a very difficult problem. Various approximation methods have been developed to simplify the computation; however depending on the method used, the results will be different. More discussion on the calculation of NMEs is provided in Section 3.2.

Information about the neutrino-mass hierarchy can be extracted from the effective Majorana mass by expressing $\langle m_{\beta\beta}\rangle$ in terms of the lightest neutrino mass. For the normal hierarchy (NH), m_1 is the lightest and

$$\begin{aligned}
\langle m_{\beta\beta}\rangle &\equiv \left| U_{e1}^2 m_1 + U_{e2}^2 m_2 + U_{e3}^2 m_3 \right| \\
&\simeq \left| U_{e1}^2 m_1 + U_{e2}^2 \sqrt{\delta m^2 + m_1^2} + U_{e3}^2 \sqrt{|\Delta m^2| + m_1^2} \right| \\
&= \Big| \cos^2\theta_{12}\cos^2\theta_{13} e^{i\alpha_1} m_1 + \sin^2\theta_{12}\cos^2\theta_{13} e^{i\alpha_2}\sqrt{\delta m^2 + m_1^2} \\
&\quad + \sin^2\theta_{13} e^{-2i\delta}\sqrt{|\Delta m^2| + m_1^2} \Big| .
\end{aligned} \tag{3.3}$$

A similar expression can also be obtained for the inverted hierarchy (IH). In Figure 3.4 [33], $\langle m_{\beta\beta}\rangle$ is plotted as a function of the lightest neutrino mass (m_1 for the NH and m_3 for the IH). Experimentally measured values for the mixing parameters [21, 34] have

been used, and the two unknown Majorana phases have been allowed to vary between 0 and 2π, producing wide bands for the NH and IH regions. The blue bands in the plot are the result of also including 1σ experimental errors in the mixing parameters. For 2σ and 3σ errors, the bands widen to include the purple and orange regions, respectively. At neutrino masses above ~ 0.1 eV, the NH and IH merge. This is known as the quasi-degenerate (QD) region, where the three neutrino masses are approximately equal:

$$\begin{aligned} m_1 \lesssim m_2 \lesssim m_3 \qquad & \text{(NH)}, \\ m_3 \lesssim m_1 \lesssim m_2 \qquad & \text{(IH)}. \end{aligned}$$

The cosmological limit in the figure comes from the restriction on the sum of the three neutrino masses. Future cosmological data and future direct neutrino-mass measurements, such as KATRIN, should push the bound on the lightest neutrino mass to even smaller energies. It is expected that cosmological observations will be sensitive to $\sum_i m_i$ in the range of $(6 \times 10^{-3} - 10^{-1})$ eV (see, for example, ref. [35]), and KATRIN, a tritium beta-decay experiment, hopes to achieve a limit on the electron-antineutrino mass of $m_{\bar{\nu}_e} < 0.2$ eV [36, 37].

The effective Majorana mass is not a directly measurable quantity. However, by measuring the partial half-life of $0\nu\beta\beta$ decay and using Equation 3.1, the value of $\langle m_{\beta\beta} \rangle$ can be extracted. So far, experiments have not observed $0\nu\beta\beta$ decay, and in those cases, a lower limit on the half-life is obtained, allowing an upper bound to be set for $\langle m_{\beta\beta} \rangle$. The most stringent upper bounds are currently set by the ^{136}Xe $0\nu\beta\beta$ decay experiments EXO-200 [38] and KamLAND-Zen [30]:

$$\begin{aligned} \langle m_{\beta\beta} \rangle < (0.140 - 0.380)\ \text{eV} \qquad & \text{(EXO-200)}, \\ \langle m_{\beta\beta} \rangle < (0.3 - 0.6)\ \text{eV} \qquad & \text{(KamLAND-Zen)}. \end{aligned}$$

A range of values is given because depending on the method used to calculate the nuclear matrix element, a different limit on $\langle m_{\beta\beta} \rangle$ will be obtained.

There are three techniques used to observe double-beta decay: geochemical, radiochemical, and direct detection. In geochemical experiments, a sample of ore containing the parent nuclide is dated using a geochronological method such as potassium-argon, lead-lead, or rubidium-strontium dating. Then, the daughter atoms are chemically extracted and isotopically assayed, for example, with a mass spectrometer. Once the number of daughter nuclei in the sample is determined, the double-beta decay half-life can be obtained. Geochemical techniques are only effective if the daughter nuclei make a measureable change in the isotopic composition of the daughter element. In practice, detection of double-beta decay is experimentally feasible mainly when noble gases are the daughter product (e.g., decay of ^{130}Te to ^{130}Xe). This is because noble gases are normally present in extremely low concentrations in terrestrial materials [39].

Radiochemical methods are used to measure double-beta decay half-lives for isotopes whose daughters are radioactive (e.g., ^{238}U, which decays to ^{238}Pu). The daughters are chemically isolated from a sample containing the parent and then counted with a particle detector. The number of daughter nuclei is obtained and compared with the number of parent nuclei, allowing the double-beta decay half-life to be determined.

Geochemical and radiological experiments are not able to differentiate between the various double-beta decay channels. Direct counting is currently the only method that

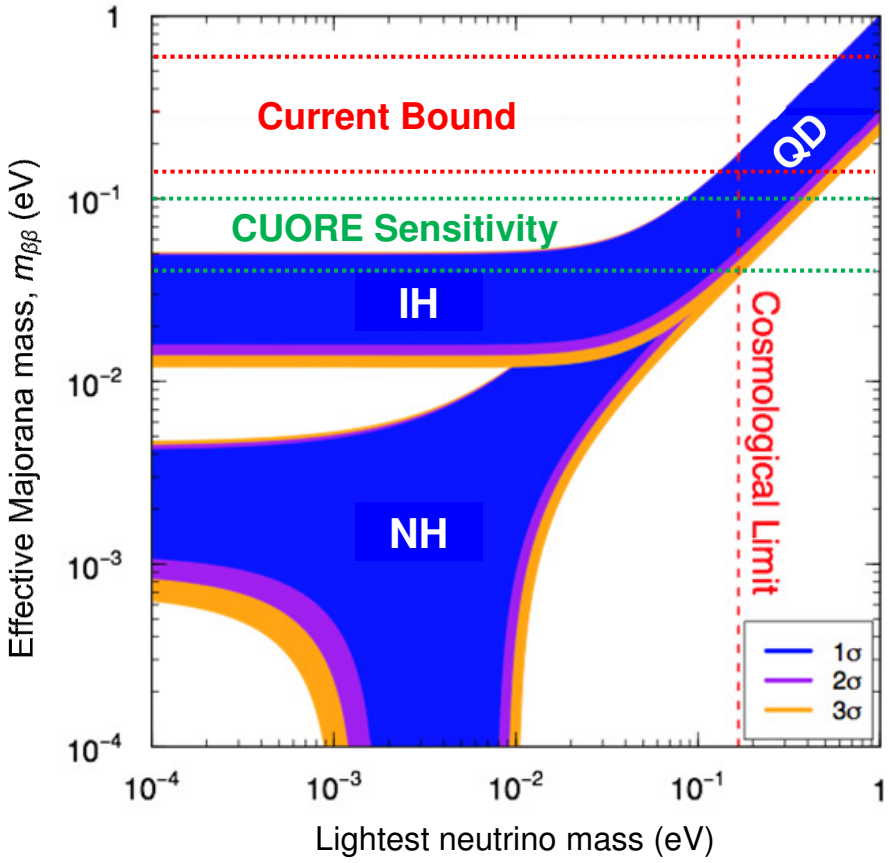

Figure 3.4: Allowed values for the effective Majorana mass as a function of the lightest neutrino mass, which is m_1 for the normal hierarchy (NH) and m_3 for the inverted hierarchy (IH); the figure was adapted from Ref. [33]. The two unknown Majorana phases have been allowed to vary between 0 and 2π, resulting in wide bands for the NH and IH regions. The blue bands are the result of including 1σ experimental errors in the mixing parameters. For 2σ and 3σ errors, the bands widen to include the purple and orange regions, respectively. At neutrino masses above ~ 0.1 eV, the NH and IH regions merge, forming the quasidegenerate (QD) region. An upper limit on the lightest neutrino mass has been obtained from cosmological data, ruling out most of the QD region. The current bound on the effective Majorana mass is set by the EXO-200 and KamLAND-Zen experiments. The CUORE experiment hopes to push this limit down to the region in the figure bound by two dotted green lines.

can distinguish $2\nu\beta\beta$ decay from $0\nu\beta\beta$ decay. In double-beta decay, the Q-value is shared among the final particles. Direct counting experiments measure the summed energy of the two electrons and, in some experiments, the energy of the recoil nucleus as well. In double-beta decay, the recoil nucleus is emitted with negligible kinetic energy because it is so much heavier than the electrons (and the antineutrinos in the case of $2\nu\beta\beta$ decay). In $0\nu\beta\beta$ decay, essentially all of the Q-value is given to the two electrons. In the spectrum of summed electron (and nuclear recoil) energies, the signature of $0\nu\beta\beta$ decay is therefore a monoenergetic peak at the Q-value. The peak will be spread only by the energy resolution of the detector. In $2\nu\beta\beta$ decay, the Q-value, minus the tiny recoil energy, is distributed among the two electrons and the two antineutrinos, which have a negligible probability of being detected. The decay will therefore produce a continuum from 0 up to the Q-value in the summed energy spectrum. The two double-beta decay signatures are illustrated in Figure 3.5. Specific direct counting experiments for $0\nu\beta\beta$ decay will be discussed in detail in Section 3.3.

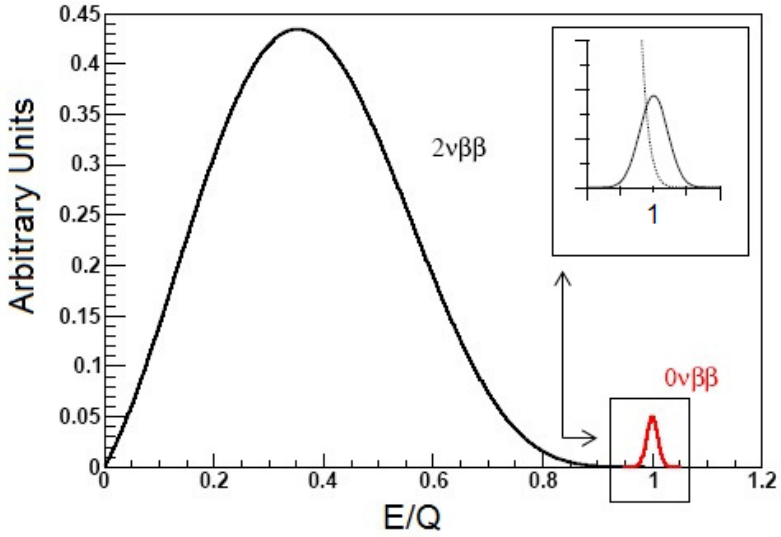

Figure 3.5: $2\nu\beta\beta$ and $0\nu\beta\beta$ decay signatures in the summed energy (E) spectrum. Q is the Q-value of double-beta decay. The inset shows that due to the resolution of the detector, the $2\nu\beta\beta$ decay region overlaps with the $0\nu\beta\beta$ peak. $2\nu\beta\beta$ decay is therefore considered a background in $0\nu\beta\beta$ decay searches.

3.2 Nuclear matrix elements

There is a large uncertainty in translating the measured half-life limits of $0\nu\beta\beta$ decay experiments into limits on $\langle m_{\beta\beta}\rangle$. This uncertainty is due to the difficulty in calculating the nuclear matrix elements $M_{0\nu\beta\beta}$. Five methods are currently used to calculate the NMEs for $0\nu\beta\beta$ decay: the Quasi-Particle Random Phase Approximation (QRPA), the Large-Scale Shell Model (LSSM), the Energy Density Functional method (EDF), the Projected Hartree-Fock-Bogoliubov approach (PHFB), and the Interacting Boson Model-2 (IBM-2) [33, and references therein]. Matrix elements obtained with each of these methods are plotted in Figure 3.6 for different isotopes.

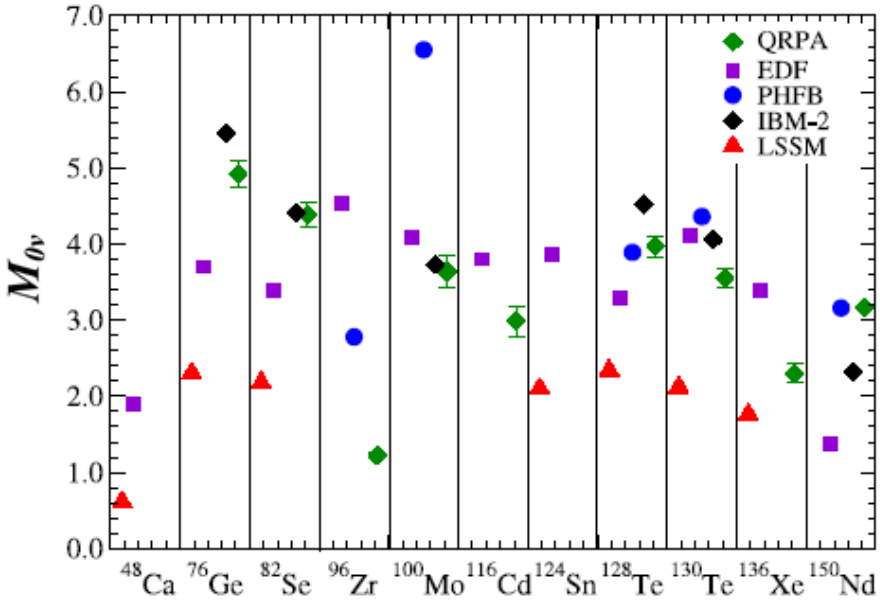

Figure 3.6: $0\nu\beta\beta$ decay nuclear matrix elements for different isotopes that were obtained using various computational methods based on nuclear structure theory. $M_{0\nu}$ in the plot is the same as $M_{0\nu\beta\beta}$. Figure was taken from Ref. [33].

3.3 Neutrinoless double-beta decay direct counting experiments

In direct counting experiments, the signature of $0\nu\beta\beta$ decay is a monoenergetic peak, spread only by the detector resolution, in the spectrum of summed electron (and sometimes nuclear recoil) energies. Experimentally observing the peak requires an extremely low background rate in the peak region and a high detector-resolution to decrease the overlap between the $2\nu\beta\beta$ decay continuum and the $0\nu\beta\beta$ decay peak (refer to insert in Figure 3.5). Several candidate isotopes are available for neutrinoless double-beta decay searches, and the ones that have been studied in past experiments are listed in Table 3.2. The choice of isotope is guided by the candidate isotope's $0\nu\beta\beta$ decay Q-value, nuclear matrix element, and natural isotopic abundance. A large Q-value is desirable because ideally, it is best if the $0\nu\beta\beta$ decay peak is above the natural gamma background, which extends up to 2615 keV. Since the phase space factor $G_{0\nu\beta\beta}(Q, Z)$ scales as Q^5, a larger Q-value also means a larger number of expected $0\nu\beta\beta$ decay events. Likewise, a higher matrix element is important because it too results in a higher number of expected events. The natural isotopic abundance of a candidate isotope can greatly affect the cost of an experiment. $0\nu\beta\beta$ decay experiments require a large population of double-beta decaying nuclei, but to keep the experimental apparatus dimensions within practical limits, the isotope of interest must make up a significant fraction of the total source-mass. For most candidate isotopes, which have small natural abundances, this must be achieved through isotopic enrichment, which adds to the cost of the experiment. ^{130}Te, the isotope chosen for CUORE, is a notable exception because it has a large natural abundance of 34.2%, allowing natural tellurium to be used as the source. Q-values and natural abundances of candidate $0\nu\beta\beta$ decaying isotopes are given in Table 3.2.

Table 3.2: Limits on $T_{1/2}^{0\nu\beta\beta}$ are given at the 90% C.L. for a selection of completed $0\nu\beta\beta$ decay experiments. Q-values for the $0\nu\beta\beta$ decay transitions, natural abundances (a) of the decaying isotopes, and $\langle m_{\beta\beta}\rangle$ limits obtained from the $T_{1/2}^{0\nu\beta\beta}$ are also listed. Unless otherwise stated, the natural isotopic abundances are taken from Ref. [28].

$\beta\beta$ decay reaction	Q (keV)	a (%)	$T_{1/2}^{0\nu\beta\beta}$ (y)	$\langle m_{\beta\beta}\rangle$ limit (eV)	Experiment
^{48}Ca $\rightarrow$ ^{48}Ti	4274 [40]	0.2	$> 5.8 \times 10^{22}$ [41]	$< 3.5 - 22$ [41]	ELEGANT VI [41]
^{76}Ge $\rightarrow$ ^{76}Se	2039 [42]	7.4	$> 1.9 \times 10^{25}$ [43]	$< 0.21 - 0.53$ [44]	HEIDELBERG-MOSCOW [43]
^{82}Se $\rightarrow$ ^{82}Kr	2996 [45]	8.7	$> 1.0 \times 10^{23}$ [46]	$< 1.7 - 4.9$ [46]	NEMO 3 [46]
^{96}Zr $\rightarrow$ ^{96}Mo	3348 [40]	2.8	$> 9.2 \times 10^{21}$ [47]	$< 7.2 - 19.5$ [47]	NEMO 3 [47]
^{100}Mo $\rightarrow$ ^{100}Ru	3034 [48]	9.6	$> 4.6 \times 10^{23}$ [46]	$< 0.7 - 2.8$ [46]	NEMO 3 [46]
^{116}Cd $\rightarrow$ ^{116}Sn	2814 [49]	7.5	$> 1.7 \times 10^{23}$ [50]	$< 1.22 - 2.30$ [44]	Solotvina [50]
^{124}Sn $\rightarrow$ ^{124}Te	2288 [40]	5.8	—	—	—
^{128}Te $\rightarrow$ ^{128}Xe	866 [5]	31.8 [51]	—	—	—
^{130}Te $\rightarrow$ ^{130}Xe	2528 [52]	34.2 [51]	$> 3.0 \times 10^{24}$ [53]	$< 0.19 - 0.68$ [53]	CUORICINO [53]
^{136}Xe $\rightarrow$ ^{136}Ba	2458 [54]	8.9	$> 1.2 \times 10^{24}$ [55]	$< 1.1 - 2.9$ [55]	DAMA [55]
^{150}Nd $\rightarrow$ ^{150}Sm	3368 [40]	5.6 [56]	$> 1.8 \times 10^{22}$ [57]	$< 4.0 - 6.3$ [57]	NEMO 3 [57]

An essential part of designing a double-beta decay experiment is determining what $0\nu\beta\beta$ decay partial half-life the experiment will be sensitive to. For a half-life of $T_{1/2}$, the expected number of *detected* $0\nu\beta\beta$ decay events, $S_{0\nu\beta\beta}$, observed during a live time t is

$$S_{0\nu\beta\beta} = N\left[1 - \exp\left(-\ln(2)\frac{t}{T_{1/2}}\right)\right] B_{0\nu\beta\beta}\epsilon \simeq N\ln(2)\frac{t}{T_{1/2}^{0\nu\beta\beta}}\epsilon, \tag{3.4}$$

where N is the total number of double-beta decaying nuclei in the source, $B_{0\nu\beta\beta}$ is the branching ratio for $0\nu\beta\beta$ decay (as a fraction of 100%), ϵ is the efficiency for detecting a $0\nu\beta\beta$ decay event, and $T_{1/2}^{0\nu\beta\beta} = T_{1/2}/B_{0\nu\beta\beta}$. The approximation in the second half of Equation 3.4 can be made because t is much smaller than $T_{1/2}$. For the case in which $0\nu\beta\beta$ decay is not conclusively observed (i.e. decay rate is statistically consistent with 0), a lower limit on $T_{1/2}^{0\nu\beta\beta}$ can be set. This lower limit is referred to as the "half-life sensitivity" of the experiment. For "source = detector" experiments, such as CUORE, in which the double-beta decaying source is part of the active region of the detector, the half-life sensitivity is often estimated by making the following assumptions: (1) the background rate scales linearly with the mass of the source, (2) the maximum number of detected $0\nu\beta\beta$ decay events is equivalent to a $n_\sigma\sigma$ fluctuation in the background. In (2), the background is assumed to follow Gaussian statistics with a standard deviation of σ, and n_σ is the desired significance level in terms of number of σ. Assumption (1) is only true in the case that background events come only from uniform intrinsic contaminations of the source material. In CUORE, for example, background events will also come from contaminations on the surfaces of the bolometers and from contaminations of detector components surrounding the bolometers. In this case, the background rate does not exactly scale linearly with the source mass; however, (1) is still useful for obtaining a first-order approximation of the half-life sensitivity.

Using assumption (1), the number of background counts, $B(\delta E)$, in an energy window δE centered at the $0\nu\beta\beta$ decay Q-value can be expressed as

$$B(\delta E) = b \cdot M \cdot \delta E \cdot t \tag{3.5}$$

where b is the background rate per unit source-mass per energy-interval (commonly in units of counts/(keV·kg·y)) and M is the total source mass. Assumption (2) then gives

$$S_{0\nu\beta\beta} \cdot f(\delta E) \leq n_\sigma \cdot \sigma = n_\sigma \sqrt{B(\delta E)}, \tag{3.6}$$

where $f(\delta E)$ is the fraction of detected $0\nu\beta\beta$ events that fall within δE. If the signal peak is a Gaussian centered at the Q-value and with an energy resolution (i.e., FWHM) of ΔE, then

$$f(\delta E) = \text{erf}\left(\frac{\delta E}{\Delta E} \cdot \sqrt{ln(2)}\right). \tag{3.7}$$

If N from Equation 3.4 is rewritten as

$$N = \frac{M}{W} N_A \cdot \eta \cdot a, \tag{3.8}$$

where W is the molar mass of the source, N_A is the Avogadro constant, η is the stoichiometric coefficient for the element of the double-beta decaying isotope, and a is the natural abundance of the isotope, then the half-life sensitivity is

$$T_{1/2}^{0\nu\beta\beta} \geq \frac{\ln(2)}{n_\sigma} \frac{N_A \cdot \eta \cdot a \cdot \epsilon}{W} \sqrt{\frac{M \cdot t}{b \cdot \delta E}} \cdot f(\delta E). \tag{3.9}$$

Equation 3.9 is useful in determining if any parameters can be reasonably tweaked in an experiment to achieve the desired sensitivity.

Past experiments have used various detection techniques to search for $0\nu\beta\beta$ decay. HEIDELBERG-MOSCOW [43, 58, 59] was a source = detector experiment that searched for the $0\nu\beta\beta$ decay of ^{76}Ge by measuring the energy deposited in the detector by the two electrons and the recoil nucleus. The experiment utilized five p-type high-purity germanium (HPGe) detectors that had a total mass of 11 kg and were isotopically enriched to 86% in ^{76}Ge. The experiment took place underground at the Gran Sasso National Laboratory (LNGS) and counted from 1990 to 2003. In 2001, a subset of the HEIDELBERG-MOSCOW Collaboration led by Klapdor-Kleingrothaus claimed that $0\nu\beta\beta$ decay had been observed [31] with a half-life of $(0.8 - 18.3) \times 10^{25}$ y (95% C. L.) with a best value of 1.5×10^{25} y, and using that half-life, they deduced an effective Majorana mass of $0.11 - 0.56$ eV (95% C. L.) with a best value of 0.39 eV. This claim of observation, was not supported by the rest of the collaboration who set a limit of $> 1.9 \times 10^{25}$ y for the half-life and a limit of $0.21 - 0.53$ eV for $\langle m_{\beta\beta} \rangle$. At the moment, no other experiment has confirmed the claim of observation.

The NEMO (Neutrino Ettore Majorana Observatory) 3 experiments [46,47,57], which took place in the Fréjus Underground Laboratory, searched for $0\nu\beta\beta$ decay by using a combination of charged-particle tracking and calorimetry to measure the energy of the two electrons. Double-beta decaying sources were placed on thin foils. A particle emitted from the foils was three-dimensionally tracked with a wire chamber made of 6180 drift cells in a mixture of 95% helium, 4% ethyl alcohol, 1% argon, and 0.1% water. A particle that passed through the wire chamber had its residual energy measured by a calorimeter made of 1940 plastic scintillator blocks coupled to low activity photomultiplier tubes. The

tracking information along with the energy measured by the calorimeter gives the energy of the particle. Due to the source being separate from the detector, NEMO 3 has been able to set $0\nu\beta\beta$ decay half-life limits on several different isotopes (refer to Table 3.2).

CUORICINO [53] was another source = detector experiment that took place at LNGS from 2003 until 2008. It used an array of 62 cryogenic TeO_2 bolometers to measure the $0\nu\beta\beta$ decay half-life of ^{130}Te. The detector contained 40.7 kg of TeO_2, of which 11 kg was ^{130}Te. Each bolometer was a single TeO_2 crystal, with dimensions of either $5 \times 5 \times 5$ cm^3 or $3 \times 3 \times 6$ cm^3, that had a neutron transmutation doped germanium thermistor attached to its surface. The crystals were operated at a base temperature between 8 and 10 mK. When particles interacted in a crystal, the energy deposition was determined by measuring the temperature rise in the crystal with the thermistor. CUORICINO was able to achieve a background rate of 0.18 counts/(keV·kg·y) in the energy region around the ^{130}Te Q-value of 2528 keV, and it set a $0\nu\beta\beta$ decay half-life limit of $> 3.0\times10^{24}$ y. Table 3.2 shows the half-life results for the HEIDELBERG-MOSCOW, NEMO 3, and CUORICINO experiments, as well as results from other completed $0\nu\beta\beta$ decay experiments. Limits on the effective Majorana mass are also provided.

Current and future experiments are moving toward using sources containing approximately a ton or more of the double-beta decaying isotope. Ton-scale searches will be able to push the limit on $\langle m_{\beta\beta}\rangle$ down into the inverted hierarchy region. Some of the major experiments include:

EXO (Enriched Xenon Observatory) [38]
EXO-200 is an experiment that started taking data in late May 2011 and is still running. It is searching for the $0\nu\beta\beta$ decay of ^{136}Xe using a time projection chamber (TPC) filled with 200 kg of liquid xenon (LXe) enriched to 80% in ^{136}Xe. When a particle deposits energy in the LXe, it ionizes nearby xenon atoms by removing electrons. Some of the electrons are drifted toward wire grids by an electric field applied across the LXe. The position of the electrons on the grid provides the 2-D location of the event, and the number of electrons arriving at the grid is related to the energy of the particle. The rest of the electrons produced by the particle interaction recombine with xenon ions, which become excited and relax by scintillating ultraviolet light. The light is then collected with avalanche photodiodes. The time between the light signal, which arrives at the photodiodes almost instanteously, and the ionization signal can be combined with the 2-D grid information to obtain the full 3-D location of the event. The ability to reconstruct 3-D locations allows the detector to discriminate between single-site events, such as $0\nu\beta\beta$ decay, and multi-site background events, such as multiple compton scattering of gamma rays. In 2012, the EXO Collaboration reported a $0\nu\beta\beta$ decay half-life of $T_{1/2}^{0\nu\beta\beta} > 1.6 \times 10^{25}$ y (90% C. L.) for ^{136}Xe and $\langle m_{\beta\beta}\rangle$ less than $0.14 - 0.38$ eV. The next-stage EXO experiment, dubbed nEXO, is currently being designed. It will be a multi-ton-scale experiment that uses the same detector technology as EXO-200 to search for $0\nu\beta\beta$ decay of ^{136}Xe. The goal is to improve the half-life sensitivity by more than a hundredfold and probe the inverted hierarchy region.

KamLAND-Zen (KamLAND ZEro Neutrino double-beta decay) [30]
KamLAND-Zen is another experiment searching for the $0\nu\beta\beta$ decay of ^{136}Xe. It started taking data in October 2011 and is still in operation. KamLAND-Zen is a modification of the original KamLAND detector. The source is 13 tons of Xe-loaded liquid scintillator

(Xe-LS) held inside a 3.08-m-diameter, spherical inner balloon (IB) that is made of 25-μm-thick, transparent nylon film; the Xe-LS contains $\sim$300 kg of ^{136}Xe. The IB is suspended at the center of the KamLAND detector by 12 nylon film straps and is surrounded by 1 kton of liquid scintillator held in a 13-m-diameter, spherical outer balloon (OB) made of 135-μm-thick nylon/EVOH (ethylene vinyl alcohol copolymer) composite film. The OB is surrounded by buffer foil and contained inside a spherical stainless steel tank (SST). Scintillation light is measured by 1325 17-inch and 554 20-inch photomultiplier tubes mounted on the SST, which is also surrounded by a 3.2-kton water-Cherenkov detector. The amount of scintillation light produced in an event is related to the energy deposition in the detector. KamLAND-Zen looks for $0\nu\beta\beta$ decay by measuring the summed energy of the two electrons. In 2012, KamLAND-Zen reported $T_{1/2}^{0\nu\beta\beta} > 5.7 \times 10^{24}$ y (90% C. L.) for ^{136}Xe and $\langle m_{\beta\beta} \rangle < 0.3 - 0.6$ eV. KamLAND-Zen's next step is to move to a ton-scale Xe-loaded experiment.

GERDA (GERmanium Detector Array) [60, 61]
GERDA is searching for the $0\nu\beta\beta$ decay of ^{76}Ge. Phase I of the experiment is currently installed at LNGS and started operation in November 2011. In Phase I, eight bare HPGe detectors, enriched to 86% in ^{76}Ge, have been submerged in a cryostat filled with liquid argon, which both cools the detectors and serves as a shield against external radioactivity. All of the detectors are standard p-type and have been taken from the completed HEIDELBERG-MOSCOW and IGEX [62, 63] experiments. In September 2013, GERDA reported a half-life limit of $T_{1/2}^{0\nu\beta\beta} > 2.1 \times 10^{25}$ y (90% C. L.) for ^{76}Ge; the total counting time was 21.6 kg·y. Combining with results from previous experiments with ^{76}Ge gives $T_{1/2}^{0\nu\beta\beta} > 3.0 \times 10^{25}$ y (90% C. L.) and $\langle m_{\beta\beta} \rangle < 0.2 - 0.4$ eV. The GERDA results are currently the most stringent for ^{76}Ge. In addition, they also reject the HEIDELBERG-MOSCOW claim of observation at the 99% level. A future one-ton experiment may be able to provide sensitivities down to the 0.01 eV mass range for $\langle m_{\beta\beta} \rangle$.

MAJORANA Demonstrator [64]
The MAJORANA Demonstrator is the first stage of the MAJORANA project, which, in collaboration with GERDA, plans to search for the $0\nu\beta\beta$ decay of ^{76}Ge with a ton-scale detector. The Demonstrator, currently being constructed at the Sanford Underground Research Facility in South Dakota, is a research and development experiment that will test the feasibility of building and operating a ton-scale detector with a goal background rate of 1 count/(ton·y) in a 4-keV region around the 2039-keV $0\nu\beta\beta$ decay peak. The Demonstrator will consist of several p-type, point contact HPGe detectors [65, 66] that have a total mass of 40 kg. Up to 30 kg of the detectors will be enriched to 86% in ^{76}Ge. With $\sim$30 kg·y of exposure, the Demonstrator should be able to either confirm or refute the HEIDELBERG-MOSCOW claim.

CUORE (Cryogenic Underground Observatory for Rare Events) [67]
The CUORE experiment will search for the $0\nu\beta\beta$ decay of ^{130}Te. A description of the detector has already been given in Chapter 1. Further details can be found in Chapter 4.

SNO+ (Sudbury Neutrino Observatory +) [68, 69]
The SNO+ detector is currently being constructed 2 km underground at the Creighton

mine near Sudbury, Ontario, Canada. It is a kton-scale liquid scintillator (LS) detector that will be used to study neutrinos. At the center of the detector is a 12-m-diameter, 5.5-cm-thick, spherical acrylic vessel (AV) filled with ∼800 tons of linear alkylbenzene LS. The AV floats in an ultra-pure water bath and is surrounded by ∼9500 8-inch photomultiplier tubes. In 2013, the SNO+ Collaboration decided to search for $0\nu\beta\beta$ decay of ^{130}Te by loading the LS with natural tellurium. SNO+ plans to counterbalance its lower energy-resolution with its ability to insert a large mass of ^{130}Te into the LS. Loading the LS with 0.3% natural tellurium, which corresponds to 800 kg of ^{130}Te, would allow the detector to probe effective Majorana masses approaching the range of the inverted hierarchy. Loading with 3% natural tellurium, which corresponds to 8 tons of ^{130}Te, would give SNO+ the potential to probe the majority of the inverted hierarchy region.

SuperNEMO [70]
SuperNEMO is a $0\nu\beta\beta$ decay experiment that is currently being constructed at the Laboratoire Souterrain de Modane in France. It will be applying the particle tracking and calorimetry techniques of the NEMO 3 experiments to search for $0\nu\beta\beta$ decay in a range of isotopes. ^{82}Se is the first isotope that will be studied, and its mass in the target will be $100 - 200$ kg. SuperNEMO plans to reach a half-life sensitivity greater than 10^{26} y, which will yield an upper limit on the effective Majorana mass of $50 - 100$ meV.

Chapter 4

The CUORE experiment

CUORE is a bolometric $0\nu\beta\beta$ experiment that is currently being constructed underground at the Gran Sasso National Laboratory (LNGS) in Italy. CUORE will search for the $0\nu\beta\beta$ decay of ^{130}Te using an array of 988 high-resolution, low-background cryogenic bolometers. The experiment is on schedule to begin some time in 2015, and it will run for 5 years.

4.1 Bolometers

A bolometer is a type of low temperature particle detector that typically consists of an energy absorber (e.g., crystal, thin piece of metal), a thermal sensor, and a heat bath that holds the entire system at a constant base temperature T_0. A particle is detected when it interacts in the absorber and deposits some amount of energy ΔE. The resulting temperature rise, ΔT, is measured by the thermal sensor and can, to good approximation, be expressed as

$$\Delta T = T - T_0 = \Delta E / C(T), \tag{4.1}$$

where T and $C(T)$ are respectively the temperature and heat capacity of the absorber immediately following the particle interaction. For dielectric, diamagnetic crystal absorbers, such as the ones used in CUORE, the heat capacity is given by the Debye law:

$$C = \frac{12\pi^4}{5}\frac{m}{M}N_A k_B \left(\frac{T}{\theta_D}\right)^3, \tag{4.2}$$

where m is the mass of the crystal, M is the molar mass of the chemical element/compound that makes up the crystal, N_A is the Avogadro constant, k_B is the Boltzmann constant, and θ_D is the Debye temperature of the crystal [71]. ΔT can be measured with high precision when $C(T)$ is sufficiently small. This can be achieved by cooling the crystal to a very low temperature, on the order of 10 mK.

When a particle interacts with an absorber, it transfers energy by scattering with nuclei and electrons in the material. Most of this energy eventually devolves into lattice vibrations (or phonons). If one ignores energy losses due to excitation of metastable states in the lattice, the theoretical resolution of a bolometer is limited only by statistical flucuations in the number of phonons exchanged with the heat bath. Considering that at a temperature T, the average energy needed to create a single phonon is approximately

$$\epsilon = k_B T, \tag{4.3}$$

the number of phonons generated in an absorber with energy E is approximately

$$N = \frac{E}{\epsilon} = \frac{C(T)T}{k_B T}. \tag{4.4}$$

Assuming N fluctuates according to Poisson statistics, the uncertainty in the energy can be expressed as

$$\delta E = \sqrt{N} \cdot \epsilon = \sqrt{k_B C(T) T^2}, \tag{4.5}$$

which does not vary significantly with energy. Plugging in typical values for CUORE bolometers ($C(T) \approx 1$ MeV/0.1 mK and $T \approx 10$ mK) gives $\delta E \approx 10$ eV. This corresponds to an energy resolution of $\sim$24 eV (i.e., $2.355 \cdot \delta E$), which is well below the resolutions of standard detectors (a few keV and higher). It should be noted that 24 eV is only a thermodynamic limit. During operation, a bolometer's resolution will be degraded by various sources of noise in the system. For CUORE bolometers, the energy resolution is typically 5-6 keV around the $0\nu\beta\beta$ decay peak.

4.2 CUORE detector

Figure 4.1a shows a sketch of a CUORE bolometer. The absorber is a $5 \times 5 \times 5$ cm^3 TeO_2 crystal; the thermal sensor, glued to the surface of the crystal with epoxy, is a neutron transmutation doped (NTD) germanium thermistor; and the heat bath is a copper frame held within a cryostat at a temperature of $\sim$10 mK. The crystal is mounted inside the copper frame using Teflon (or PTFE) supports (Figure 4.1b). The temperature signal from the thermistor is read out by front-end electronics located outside the cryostat. The thermistor is connected to these electronics via gold wires bonded to a Cu-PEN (Copper traces on a Polyethylene 2, 6-Naphthalate substrate) cable [72], which is mounted on the side of the copper frame. The PTFE supports and thermistor provide a thermal coupling between the crystal and the frame.

Figure 4.1b shows four bolometers arranged together in a module. In CUORE, 13 of these modules will be stacked on top of each other to form a single tower. Then, 19 of these towers will be combined to form an array (Figure 4.1c).

4.2.1 Thermistors

The NTD germanium thermistors used in CUORE are extremely reproducible and were made by irradiating natural germanium wafers with reactor neutrons [73]. Dopants are produced via the following reactions:

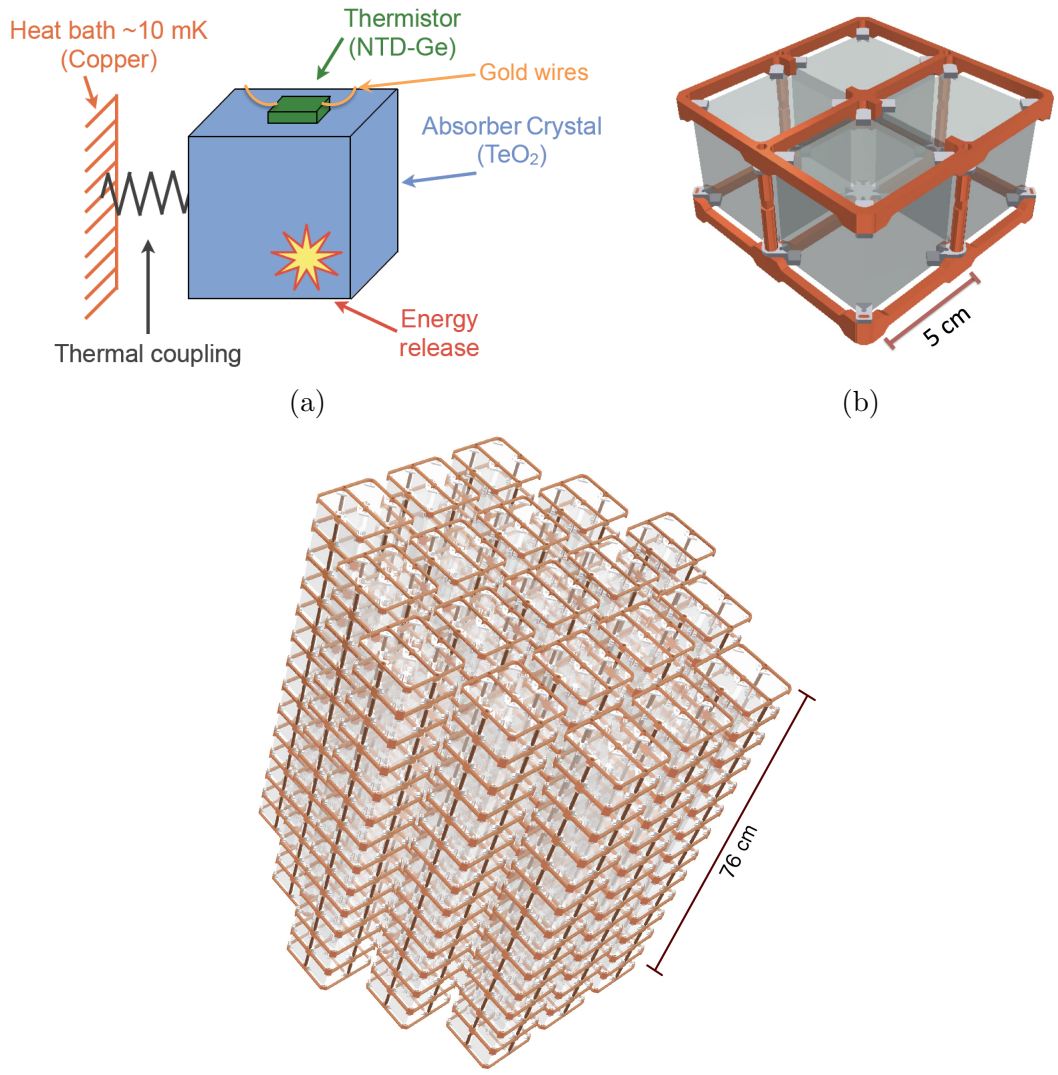

Figure 4.1: (a) Sketch of a CUORE bolometer. A $5 \times 5 \times 5$ cm^3 TeO_2 crystal serves as the absorber. A NTD germanium thermistor is glued to the surface of the crystal to measure the temperature. A copper frame held at ∼10 mK serves as the heat bath. The crystal is thermally coupled to the copper via PTFE supports and the thermistor. (b) A module of four CUORE bolometers. Each crystal is held in the copper frame (red) by PTFE supports (white). In CUORE, 13 of these modules are stacked to form a single tower. (c) Illustration of the planned 19-tower CUORE detector array.

$$
\begin{aligned}
^{70}\text{Ge (21\%)} + \text{n} &\rightarrow {}^{71}\text{Ge } (t_{1/2} = 11.43 \text{ d}) \\
^{71}\text{Ge} &\rightarrow {}^{71}\text{Ga (Acceptor)} \qquad (4.6) \\
^{74}\text{Ge (37\%)} + \text{n} &\rightarrow {}^{75}\text{Ge } (t_{1/2} = 82.78 \text{ m}) \\
^{75}\text{Ge} &\rightarrow {}^{75}\text{As (Donor)} \qquad (4.7) \\
^{76}\text{Ge (7.7\%)} + \text{n} &\rightarrow {}^{77}\text{Ge } (t_{1/2} = 11.3 \text{ h}) \\
^{77}\text{Ge} &\rightarrow {}^{77}\text{As } (t_{1/2} = 38.83 \text{ h}) \\
^{77}\text{As} &\rightarrow {}^{77}\text{Se (Double donor)} \qquad (4.8)
\end{aligned}
$$

After the radioactivity produced has decayed to acceptable levels (∼6 months after the neutron exposure), the wafers are cut into $\sim 3 \times 3 \times 1$ mm^3 chips [74] to make individual thermistors.

At low temperatures, conduction in the thermistors is dominated by phonon-assisted tunneling (or "hopping"). This is a process in which electrons can tunnel through potential barriers between impurity sites after absorbing or emitting a phonon; refer to Figure 4.2. When there is a sufficient number of high energy phonons available, electrons prefer to hop to the nearest unoccupied impurity site. In CUORE, the temperature is so low that there are very few high energy phonons present. In this case, electrons can travel long distances if a site farther away has an energy that matches an already available phonon. This process is known as variable range hopping (VRH). In the VRH regime, the resistance of an NTD thermistor at temperature T is given by

$$R = R_0 e^{(T_0/T)^\gamma}. \qquad (4.9)$$

Here, $\gamma = 1/2$ and $R_0 = \rho_0 l/A$, where l and A are the thermistor's length and cross-sectional area, respectively. The parameters ρ_0 and T_0 depend on the doping concentration in the thermistor and must be determined experimentally. Inserting typical values for CUORE thermistors ($R_0 = 1.15$ Ω, $T_0 = 3.35$ K, $T = 10$ mK) into Equation 4.9 gives $R \approx 100$ MΩ.

4.2.2 Bolometer operation

To convert temperature variations in the TeO_2 crystals into electrical signals, the thermistor biasing circuit shown in Figure 4.3 was used. Two load resistors with a total resistance R_L were placed in series with the thermistor (resistance R_{Th}). The resistance R_L was chosen to be much greater than R_{Th} so that an applied bias voltage V_{Bias} would produce an approximately constant current (I) in the thermistor:

$$I = \frac{V_{Bias}}{(R_L + R_{Th})} \approx \frac{V_{Bias}}{R_L}. \qquad (4.10)$$

In CUORE, R_L is typically tens of GΩ. The voltage over the thermistor is then

$$V_{Th} = I R_{Th} \approx \left(\frac{V_{Bias}}{R_L} \right) R_{Th}. \qquad (4.11)$$

Since R_{Th} is given by Equation 4.9, which is a function of temperature, V_{Th} is also a function of temperature.

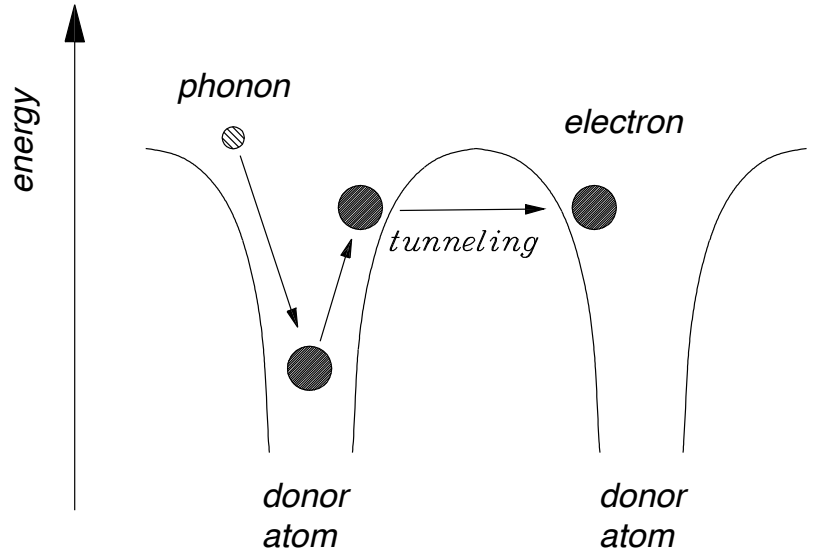

Figure 4.2: Illustration of phonon-assisted tunneling (or "hopping"). Electrons can tunnel through potential barriers between impurity sites after absorbing or emitting a phonon.

When a particle interacts in a TeO_2 crystal, V_{Th} generally changes by $\sim$0.3 mV per MeV of energy deposition. The voltage then returns to its base value (at $\sim$10 mK) with a decay time on the order of 1 second. Figure 4.4 shows a typical voltage pulse after it has been amplified and filtered.

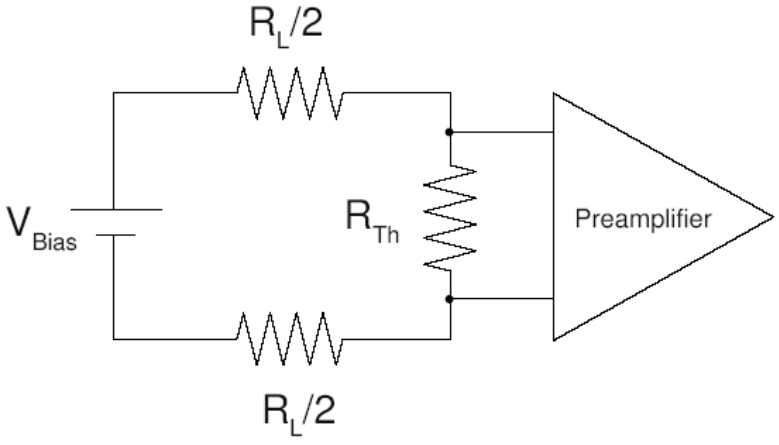

Figure 4.3: Circuit used to bias each CUORE thermistor. R_{Th} is the thermistor resistance, R_{L} is the total load resistance, and V_{Bias} is the bias voltage.

4.2.3 Cryostat and shields

During operation, the CUORE array will be mounted inside a He^3/He^4 dilution refrigerator cryostat [75] and cooled to $\sim$10 mK. Several layers of shielding will be placed

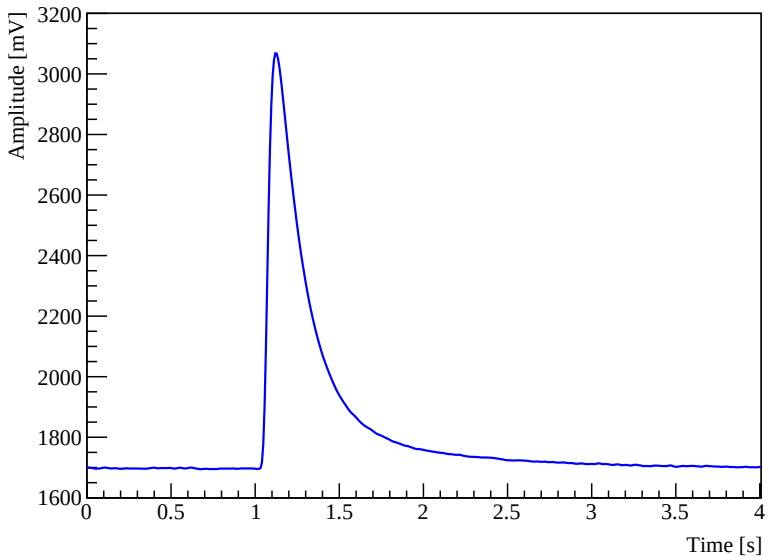

Figure 4.4: Typical voltage pulse from a particle interaction in a CUORE bolometer. The signal has been amplified and filtered.

inside and outside the cryostat to minimize the amount of background radiation reaching the detector. Figure 4.5 shows the shields inside the cryostat, which include:

- six nested copper vessels, each held at a different temperature (going from the outermost vessel inwards, the temperatures are 300 K, 40 K, 4 K, 600 mK, 50 mK, and 10 mK) - also known as the thermal shields;
- a 30 cm thick lead shield (24 cm of modern lead plus 6 cm of ancient Roman lead) located above the detector;
- a 6 cm thick Roman lead shield, anchored to the 600 mK copper vessel.

The outside of the cryostat will be surrounded by a ∼25 cm lead shield to absorb environmental gammas and a borated PET shield (18 cm thick polyethylene outer layer, 2 cm thick H_3BO_3 inner layer) to thermalize and absorb environmental neutrons.

4.3 Background sources in CUORE

In $0\nu\beta\beta$ decay experiments, one of the greatest challenges is minimizing radioactive background sources that can obscure the $0\nu\beta\beta$ decay signal. As can been seen from Equation 3.9, the half-life sensitivity of a $0\nu\beta\beta$ experiment can be substantially limited by this background. CUORE aims to have a background rate of 0.01 counts/(keV·kg·y) in the region surrounding the $0\nu\beta\beta$ decay peak at 2528 keV. This so called "$0\nu\beta\beta$ decay region" has been chosen to be 2497 - 2558 keV for CUORE background studies. This section discusses the various background sources in CUORE.

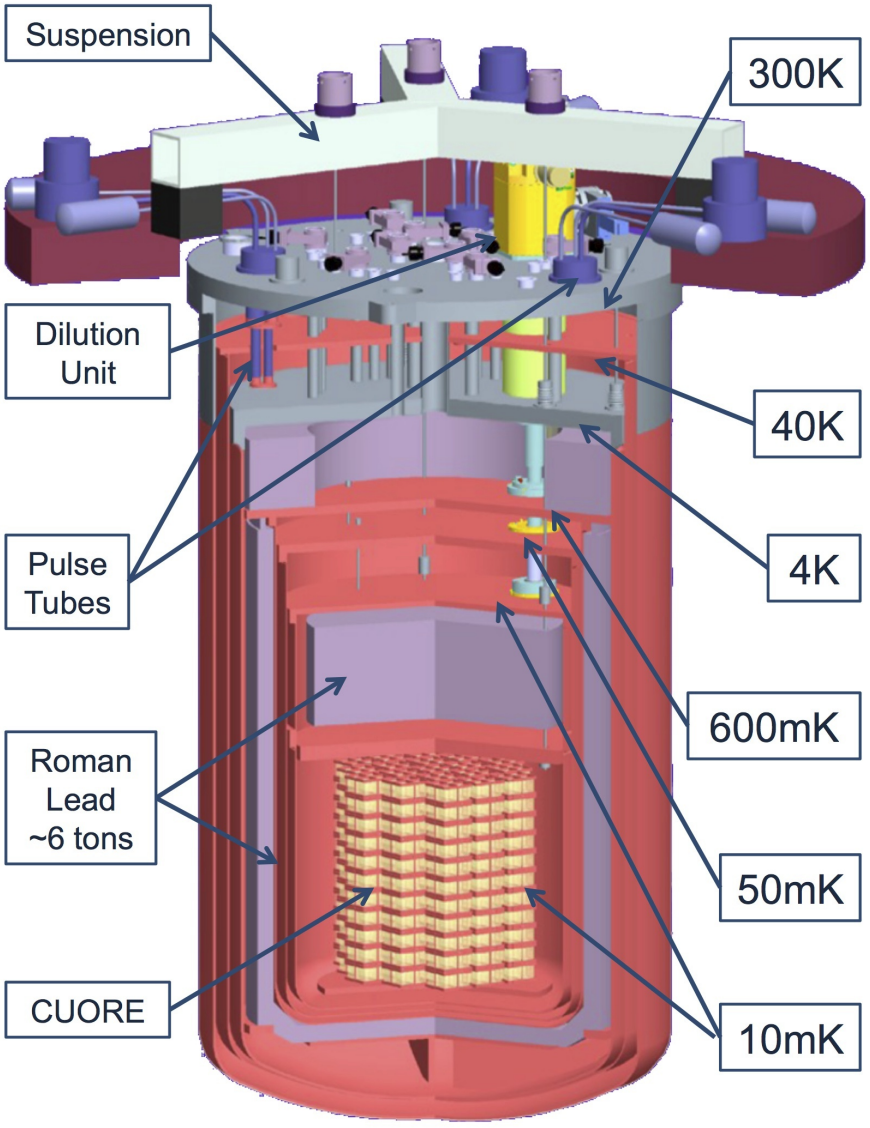

Figure 4.5: Schematic of the cryostat used to cool down the CUORE detector. The detector is located in the center and surrounded by several layers of shielding (e.g., lead shields and several thermal shields, which are labeled by their temperature).

4.3.1 Cosmic ray muons

The Gran Sasso National Laboratory where the CUORE detector is housed is located underground beneath the Gran Sasso mountain range, which provides an overburden of ∼3650 meters water equivalent. After passing through this thickness of rock, the flux of cosmic ray muons produced in the Earth's atmosphere is reduced by approximately six orders of magnitude. The average muon energy underground is 270 GeV [76] and the total flux is $(2.58 \pm 0.3) \times 10^{-8}$ cm^{-2}s^{-1} [77]. Direct muon interactions in the CUORE detector are not generally problematic because the energy deposition in a crystal would be a few tens of MeV, well above the 2528-keV Q-value. Additionally, a single muon will usually interact with several crystals at the same time. This kind of event can be easily distinguished from a $0\nu\beta\beta$ decay event, which deposits energy only in a single crystal. Muons are an issue because their interactions with the detector setup can produce gammas and neutrons with energies that are problematic for CUORE. The use of high density, high A materials (e.g., lead shields) exacerbates the situation because the neutron yield is proportional to $A^{0.8}$ [78]

4.3.2 Environmental neutrons

At LNGS, the neutron flux below ∼10 MeV is primarily due to spontaneous fission (mainly by ^{238}U) and (α,n) reactions with light nuclei in the rock. The alphas come from uranium, thorium, and their decay products, which are naturally present in the rock. Neutrons from ∼10 MeV to around a few GeV are produced by cosmic ray muon interactions with nuclei in the rock. The neutron flux below 10 MeV is $\sim 4 \times 10^{-6}$ cm^{-2}s^{-1}. The flux above 10 MeV has been determined to be three orders of magnitude lower [6].

4.3.3 Environmental gamma activity

At LNGS, the gamma-ray spectrum below 3 MeV is mainly due to natural radioactivity in the rock. In this region, only the 2615-keV gamma ray from ^{208}Tl (^{232}Th decay chain) is of concern; it is the only naturally occuring gamma ray with an energy higher than 2528 keV that is emitted with a substantial branching ratio. These gammas can deposit energy in the $0\nu\beta\beta$ decay region via multiple-Compton scatteirng. Above 3 MeV, the gammas come primarily from neutron and muon interactions with the rock. The flux below 3 MeV is ∼0.73 cm^{-2}s^{-1}. The flux above 3 MeV is estimated to be 10^5 times smaller than the flux of 2615 MeV gamma rays from ^{208}Tl [6].

4.3.4 Radioactivity in detector materials

^{238}U and ^{232}Th contaminations: All detector materials used in CUORE were checked for their radiopurity. Most of the detector components contained small amounts of ^{238}U and ^{232}Th. The contamination levels were measured using various techniques including bolometric measurements for the TeO_2 crystals and gold wires; gamma counting with a high-purity germanium detector for the lead, copper, and steel parts of the detector; and neutron activation analysis for the PTFE supports and Cu-PEN cables. A comprehensive list of the detector components examined and the measurement techniques used is given in Ref. [8]. Of main concern are ^{232}Th contaminations in the cryostat or its shields because 2615-keV gammas from the daughter isotope ^{208}Tl can contribute counts to the $0\nu\beta\beta$

decay region by multiple-Compton scattering. ^{238}U and ^{232}Th surface contaminations on the TeO_2 crystals and copper frames have also been shown to be a problem. Alphas from these isotopes and their daughters are all emitted with an energy $E_\alpha > 2528$ keV, and they each have the potential to deposit energy anywhere between 0 keV and E_α. Energy deposition in the $0\nu\beta\beta$ decay region can then occur in the following ways:

(1) the alpha is produced in the copper and loses some energy before entering a crystal;
(2) the alpha is produced in a crystal and escapes the array before depositing all of its energy;
(3) the alpha is produced in one crystal and loses some energy before entering a second crystal.

Case (3) is not problematic because it is a multi-crystal event and therefore distinguishable from a (single-crystal) $0\nu\beta\beta$ decay event. Cases (1) and (2) can only be dealt with by using effective cleaning methods for the surfaces of the copper and TeO_2 crystals. Another possibility is to cover the copper surface with an extra layer of material to absorb the alphas before they reach the crystals.

Cosmogenic activation: Primary cosmic rays (87% protons, 12% alphas, ∼1% heavier nuclei) entering the Earth's atmosphere produce cascades of secondary cosmic rays by interacting with nuclei in the air [79]. Particles in these cascades include protons and neutrons; alphas; pions, which decay to muons and gammas; and electrons and positrons, which can come from gamma pair-production or muon decay. At sea-level, the relative intensity of charged pions:protons:electrons:neutrons:muons is approximately 1:13:340:480:1420 [9]. Cosmogenic activation is the process in which interactions with these particles produce isotopes in materials. This process occurs while detector components are sitting on the surface of the earth. In CUORE, once all materials are moved underground, activation is negligible. Cosmogenic activation is an issue primarily for the TeO_2 crystals and the copper frames. While these components are above ground at sea-level, activation is due mainly to interactions with cosmic ray hadrons, which as shown earlier are dominated by *neutrons*. Production of ^{60}Co has been observed in the copper frames. This isotope has a half-life of 5.27 y and a beta-decay Q-value of 2.8 MeV. It has the potential to contribute events in the $0\nu\beta\beta$ decay region if its two main gamma rays (1.17MeV and 1.33 MeV) deposit most or all of their energy in one crystal. The contamination level of ^{60}Co in copper was determined to be < 50 μBq/kg.

For the TeO_2 crystals, cosmogenic activation occurred during their shipment by boat from the production site in Shanghai, China to LNGS. Any long-lived radioisotopes produced with decay Q-values greater than 2528 keV have the potential to contribute background to the $0\nu\beta\beta$ region. These radioisotopes are a source of irreducible background, and therefore a good estimate of their contribution to the $0\nu\beta\beta$ decay region is essential. CUORE currently does not have a good estimate, however, because of the lack of experimental cross sections for neutron interactions with TeO_2. Some data exist for neutron interactions with individual tellurium isotopes, but the neutron energies only go up to approximately 20 MeV [10]. From 800 MeV to tens of GeV, measured proton-activation data exist for natural tellurium [11]. This information can be used for neutron studies because at such high energies above the Coulomb barrier, activation cross sections for neutrons and protons are approximately the same. Additional cross-section measure-

ments are therefore needed to cover the intermediate region between 20 MeV and 800 MeV. This thesis discusses a cross-section measurement performed at the Los Alamos Neutron Science Center in which a TeO_2 powder target was irradiated with a spectrum of neutrons similar in shape to the cosmic ray neutron spectrum at sea-level. Activated radioisotopes that can deposit energy in the $0\nu\beta\beta$ decay region were identified and their cross sections were used to estimate the background rate in the $0\nu\beta\beta$ region.

4.4 Experimental sensitivity to neutrinoless double-beta decay

Equation 3.9 can be used to get the half-life sensitivity of CUORE. If we assume

- $\delta E = \Delta E = 5$ keV in Equation 3.7,
- the efficiency for detecting $0\nu\beta\beta$ decay is $\epsilon = 0.874$ [4],
- the background rate is $b = 0.01$ counts/(keV·kg·y),
- and the counting time is $t = 5$ years,

CUORE will have a sensitivity of $T_{1/2}^{0\nu\beta\beta} \geq 1.6 \times 10^{26}$ y.

Chapter 5

Cross-section measurement for neutron activation of TeO_2

To estimate the background in CUORE from cosmogenic neutron activation of the TeO_2 crystals, the following must be determined:

(1) what radioisotopes are activated in TeO_2 by sea-level cosmic-ray neutrons and which of those are problematic for CUORE, i.e., will contribute background in the $0\nu\beta\beta$ decay region while CUORE is counting;
(3) the production rate of problematic radioisotopes while the TeO_2 crystals are above ground at sea-level.

Chapter 6 will discuss how to estimate the background due to cosmogenic activation using radioisotope-production cross sections that have been measured at the Los Alamos Neutron Science Center (LANSCE) Weapons Neutron Research (WNR) facility. The cross-section measurement will be discussed in this chapter.

5.1 Independent and cumulative cross sections

For simplicity, consider a case where a thin target comprised only of a stable isotope A is exposed to a constant monoenergetic neutron flux, ϕ, which is in units of neutrons/(cm^2·s). Suppose that during the exposure, isotope B is both directly and indirectly produced from interactions with A nuclei. Here, direct production of B refers to the creation of B from the reaction A(n,X)B, where A is the target nucleus and X represents all possible combinations of light and heavy outgoing particles emitted along with B. The neutron, n, is what is known as a primary particle; X and B are secondary particles. Indirect production of B refers to the creation of B through the interaction or decay of a secondary particle.

For common irradiation times, the number of interactions in a target is usually much smaller than the number of target nuclei at the beginning of the irradiation, N. This means that N can be assumed to be constant during the irradiation. The rate $R_{ind}(t)$ for directly producing B at time t during the irradiation can then be expressed as

$$R_{ind}(t) \simeq N\sigma_{ind}\phi, \tag{5.1}$$

where σ_{ind} (with units of cm^2) is referred to as the *independent* cross section for producing B. The rate R_{cum} for both directly and indirectly producing B during the irradiation can be expressed as

$$R_{cum}(t) = \sum_i R_i(t), \tag{5.2}$$

where each $R_i(t)$ is the rate for producing B via a particular process. The summation is taken over all possible processes. One situation commonly encountered in neutron irradiation experiments is where all indirect production of B comes only from the decay of one or more secondary particles that were created by neutron interactions with A. If these decays occur on a time scale much shorter than t_{irrad}, Equation 5.2 can be written as

$$R_{cum}(t) \simeq N\sigma_{cum}\phi. \tag{5.3}$$

The parameter σ_{cum} is the *cumulative* cross section (in units of cm^2) for producing B. It depends on the independent cross section for producing B, the independent cross sections for producing the parent isotopes [80] of B, and the branching ratios of the parent isotopes for decaying to B.

Suppose the thin target is made of a chemical element that consists of isotopes A_i, each with a natural abundance a_i. The production rates for a particular isotope of interest, say B, would still be obtained using Equations 5.1 and 5.3. However now,

$$N = \sum_i N_i, \tag{5.4}$$

where N_i is the number of A_i nuclei in the target and the summation is taken over all isotopes. Additionally, the cross sections σ_{ind} and σ_{cum} would be expressed as

$$\sigma_{ind} = \sum_i a_i\sigma_{ind,i} \tag{5.5}$$

and

$$\sigma_{cum} = \sum_i a_i\sigma_{cum,i}, \tag{5.6}$$

where $\sigma_{ind,i}$ and $\sigma_{cum,i}$ are the independent and cumulative cross sections for producing B from A_i, and the summations are taken over all isotopes. In this chapter, *all* isotope-production cross sections discussed are either independent or cumulative. For a few of the isotopes, indirect production is due to the decay of secondary particles with half-lives $t_{1/2,i}$ on the order of or larger than t_{irrad}, but smaller than the half-life of B. In this case, the approximation in Equation 5.3 is not valid. A cumulative cross section can be obtained, however, because following the end of irradiation, the activity of B at a time $t >> t_{1/2,i}$ can be expressed in terms of σ_{cum}.

5.2 Radioisotope production at sea-level

For a $5 \times 5 \times 5$ cm^3 TeO_2 crystal exposed to cosmic-ray neutrons at sea-level, the production rate, R_{CR}, of a particular isotope in the crystal can be derived by first obtaining the production rate in a differential volume element dV (Figure 5.1):

$$\mathrm{d}R_{CR} = \left(\frac{N}{L}\mathrm{d}z\right)\int_{E_{min}}^{E_{max}} \sigma(E)\varphi_{CR}(E)T(E,z)\mathrm{d}E. \tag{5.7}$$

The parameter N is the number of target nuclei in the crystal. If the isotope is produced by neutron interactions with tellurium, N is the number of tellurium nuclei in the crystal. Likewise, if the isotope is produced by neutron interactions with oxygen, N is the number of oxygen nuclei in the crystal. L is the the total thickness of the crystal traversed by the neutrons, $\sigma(E)$ is the cross section for producing the isotope when neutrons of energy E interact with the target nuclei, $\varphi_{CR}(E)$ is the differential sea-level cosmic-ray neutron flux in units of neutrons/(cm^2·s·MeV), $T(E,z)$ is the fraction of incoming neutrons that are transmitted through a crystal thickness of z, and E_{min} and E_{max} are respectively the lowest and highest neutron energies the crystal is exposed to. Integrating over the entire

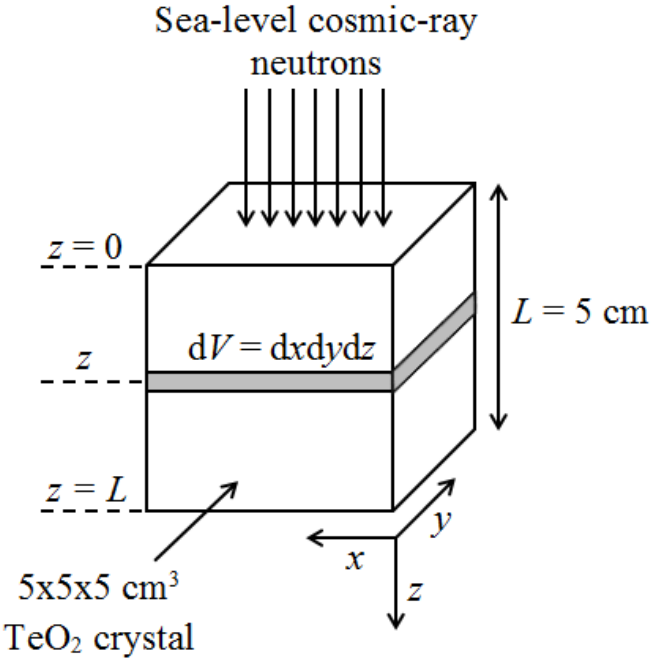

Figure 5.1: Schematic of a $5 \times 5 \times 5$ cm^3 TeO_2 crystal exposed to cosmic-ray neutrons at sea-level.

thickness of the crystal then gives

$$\begin{aligned} R_{CR} &= \int_0^L \left(\frac{N}{L}\mathrm{d}z\right)\int_{E_{min}}^{E_{max}} \sigma(E)\varphi_{CR}(E)T(E,z)\mathrm{d}E \\ &= N\int_{E_{min}}^{E_{max}} \sigma(E)\varphi_{CR}(E)\frac{\int_0^L T(E,z)\mathrm{d}z}{L}\mathrm{d}E. \end{aligned} \tag{5.8}$$

If we define

$$\bar{T}(E) \equiv \frac{\int_0^L T(E,z)\mathrm{d}z}{L}, \tag{5.9}$$

Equation 5.8 becomes

$$\begin{aligned} R_{CR} &= N\int_{E_{min}}^{E_{max}} \sigma(E)\varphi_{CR}(E)\bar{T}(E)\mathrm{d}E \\ &= N\int_{E_{min}}^{E_{max}} \sigma(E)\varphi_{CR}(E)\bar{T}(E)\mathrm{d}E\frac{\int_{E_{min}}^{E_{max}}\sigma(E)\varphi_{CR}(E)\mathrm{d}E}{\int_{E_{min}}^{E_{max}}\sigma(E)\varphi_{CR}(E)\mathrm{d}E}. \end{aligned} \tag{5.10}$$

If we define

$$\bar{T} \equiv \frac{\int_{E_{min}}^{E_{max}}\sigma(E)\varphi_{CR}(E)\bar{T}(E)\mathrm{d}E}{\int_{E_{min}}^{E_{max}}\sigma(E)\varphi_{CR}(E)\mathrm{d}E}, \tag{5.11}$$

Equation 5.10 becomes

$$\begin{aligned} R_{CR} &= N\bar{T}\int_{E_{min}}^{E_{max}} \sigma(E)\varphi_{CR}(E)\mathrm{d}E \\ &= N\bar{T}\int_{E_{min}}^{E_{max}} \sigma(E)\varphi_{CR}(E)\mathrm{d}E\frac{\int_{E_{min}}^{E_{max}}\varphi_{CR}(E)\mathrm{d}E}{\int_{E_{min}}^{E_{max}}\varphi_{CR}(E)\mathrm{d}E}. \end{aligned} \tag{5.12}$$

Finally, if we define

$$\bar{\sigma}_{CR} \equiv \frac{\int_{E_{min}}^{E_{max}}\sigma(E)\varphi_{CR}(E)\mathrm{d}E}{\int_{E_{min}}^{E_{max}}\varphi_{CR}(E)\mathrm{d}E}, \tag{5.13}$$

then Equation 5.12 becomes

$$R_{CR} = N\bar{\sigma}_{CR}\bar{T}\int_{E_{min}}^{E_{max}}\varphi_{CR}(E)\mathrm{d}E. \tag{5.14}$$

N can be calculated since the density of the CUORE crystals is known. The differential cosmic-ray neutron flux, $\varphi_{CR}(E)$, is also known, having been experimentally measured multiple times [81]. $\bar{T}$ is a difficult term to obtain because it depends on the shape of the isotope-production cross section, which is not well-known at neutron energies below 800 MeV for most isotopes activated in TeO_2. For the cosmogenic-activation background estimate discussed in Chapter 6, $\bar{T}$ is set equal to 1 (i.e., no neutron attenuation through the CUORE crystals) for simplicity. The term $\bar{\sigma}_{CR}$ is the so-called "flux-averaged cross section." For each isotope, $\bar{\sigma}_{CR}$ has been estimated by setting it equal to the flux-averaged cross section obtained from a neutron activation experiment performed at the LANSCE WNR facility at the end of February 2012. During this experiment, a sample of TeO_2 powder was irradiated for $\sim$43 h from February 25 until February 27 with the high intensity 4FP30R neutron beam, which has an energy spectrum closely resembling that of cosmic-ray neutrons at sea-level. Details of the experiment and the cross-section analysis are discussed below.

5.3 Neutron irradiation at LANSCE

5.3.1 Irradiation target

The target sample irradiated at the LANSCE WNR facility is illustrated in Figure 5.2. It consisted of 272 g of natural TeO_2 powder held within a cylindrical plastic container wrapped on all sides with a single layer of cadmium foil. The cadmium was used to (1) monitor neutrons via the reactions Cd(n,X)^{105}Ag and Cd(n,X)^{110m}Ag and (2) to remove thermal neutrons [79, 82] with energies ranging from ∼0.01 eV up to ∼0.3 eV. Circular aluminum and gold foils were also placed on either side of the target to monitor neutrons via the reactions ^{27}Al(n,X)^{22}Na and ^{197}Au(n,γ)^{198}Au. Table 5.1 contains details of each target component.

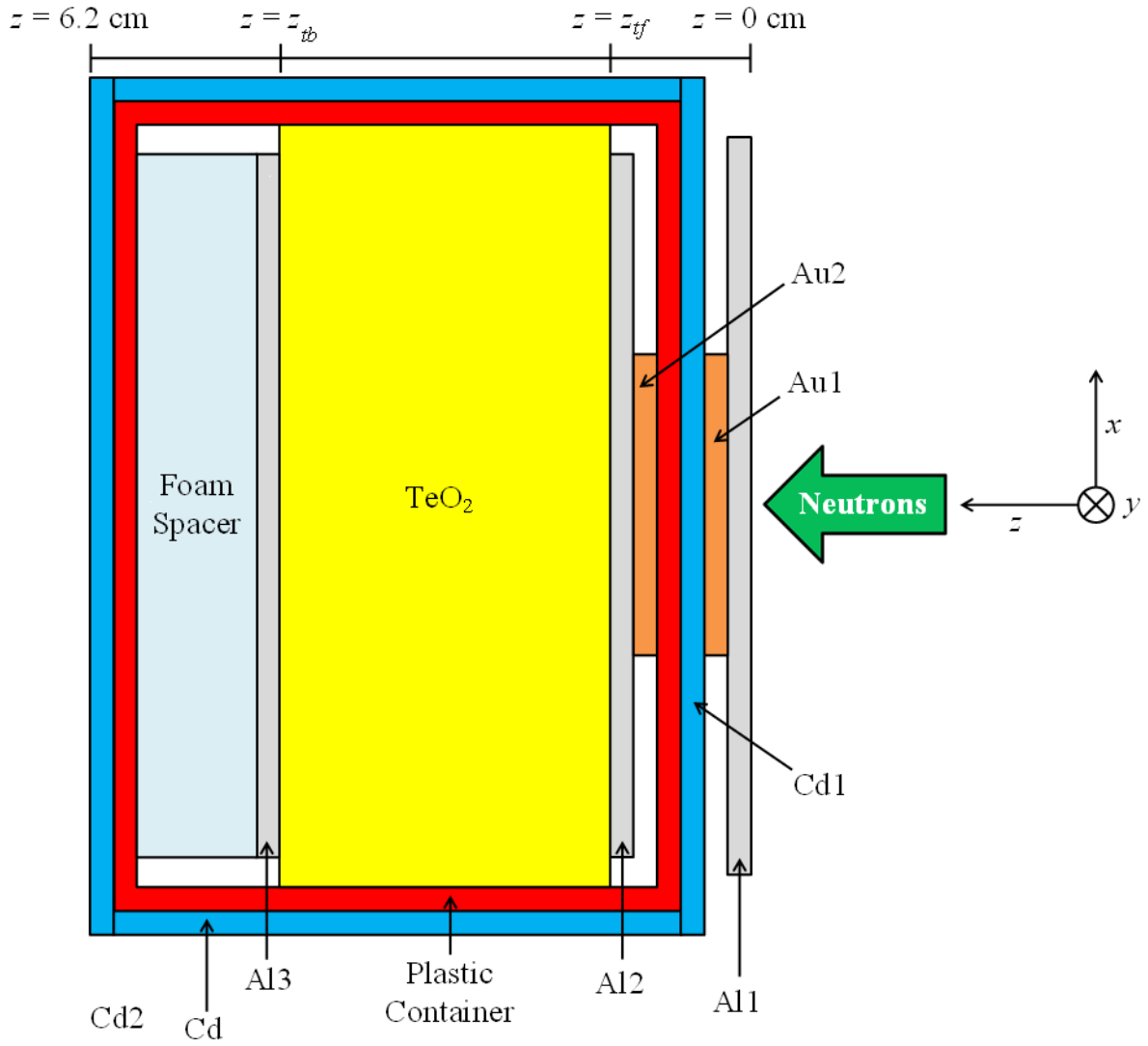

Figure 5.2: Schematic of the target irradiated at LANSCE. The entire target is 6.2 cm long in the z direction. Each target component is a cylinder with its axis along the z-axis. Details on each component are given in Table 5.1.

Table 5.1: Description of the target components illustrated in Figure 5.2. The parameters w, d, and m are respectively the thickness, diameter, and mass of the component.

Component	Material	Purpose	w (cm)	d (cm)	m (g)
TeO_2	TeO_2 powder	Target	2.79	6.43	271.56
Al1	Al	Monitor foil	0.0813	6.22	6.68
Al2	Al	Monitor foil	0.0813	5.93	6.06
Al3	Al	Monitor foil	0.0813	5.93	6.06
Au1	Au	Monitor foil	0.00515	2.54	0.504
Au2	Au	Monitor foil	0.00512	2.54	0.500
Cd1	Cd	Monitor foil Thermal neutron absorber	0.05	6.7	16.3
Cd2	Cd	Monitor foil Thermal neutron absorber	0.05	7.3	19.9
Cd	Cd	Thermal neutron absorber	0.05	—	—
Plastic Container	Polystyrene	Hold target components	0.2	—	—

5.3.2 Neutron beam

At the WNR facility, neutrons with energies up to ∼800 MeV are produced via spallation reactions by bombarding an unmoderated tungsten cylinder (Target 4 in Figure 5.3) with an 800 MeV pulsed proton beam from the LANSCE linear accelerator. The time structure of the proton beam during the TeO_2 cross-section measurement is shown in Figure 5.4. The proton beam entering Target 4 consisted of 625-μs-long proton macropulses occuring at a rate of 40 Hz, and each macropulse contained proton micropulses spaced 1.8 μs apart. There are $\sim 7 \times 10^8$ protons per micropulse, which results in a beam current of ∼1.5 μA during the measurement.

Several neutron beams are available at the WNR facility for neutron-irradiation experiments, and the flight path of each, labeled in Figure 5.3, goes off at a different angle relative to the proton-beam direction. The flight path used in the TeO_2 cross-section measurement was 4FP30R (henceforth referred to as 30R), which points 30° to the right of the proton-beam direction. The reasons for chosing 30R are two-fold: (1) its neutron-energy spectrum is very similar to that of cosmic-ray neutrons at sea-level and (2) its neutron flux is $\sim 3 \times 10^8$ times higher than the cosmic-ray neutron flux at sea-level, allowing the TeO_2 powder to see ∼1.5 million years' worth of sea-level neutrons in less than two days. For comparison, the 30R neutron spectrum and the measured sea-level cosmic-ray neutron spectrum [81] (multiplied by a factor 3×10^8) are shown in Figure 5.5. The 30R and sea-level cosmic-ray neutron fluxes are each tabulated in Appendix A as a function of energy.

During the cross-section measurement, the neutron spectrum along the 30R flight path was acquired using time-of-flight (ToF) techniques and a ^{238}U fission ionization chamber [83] located 25.4 cm upstream of the TeO_2 target. The ToF, described in Figure 5.6, is the time it takes for a neutron to travel a distance L from the tungsten target to the fission

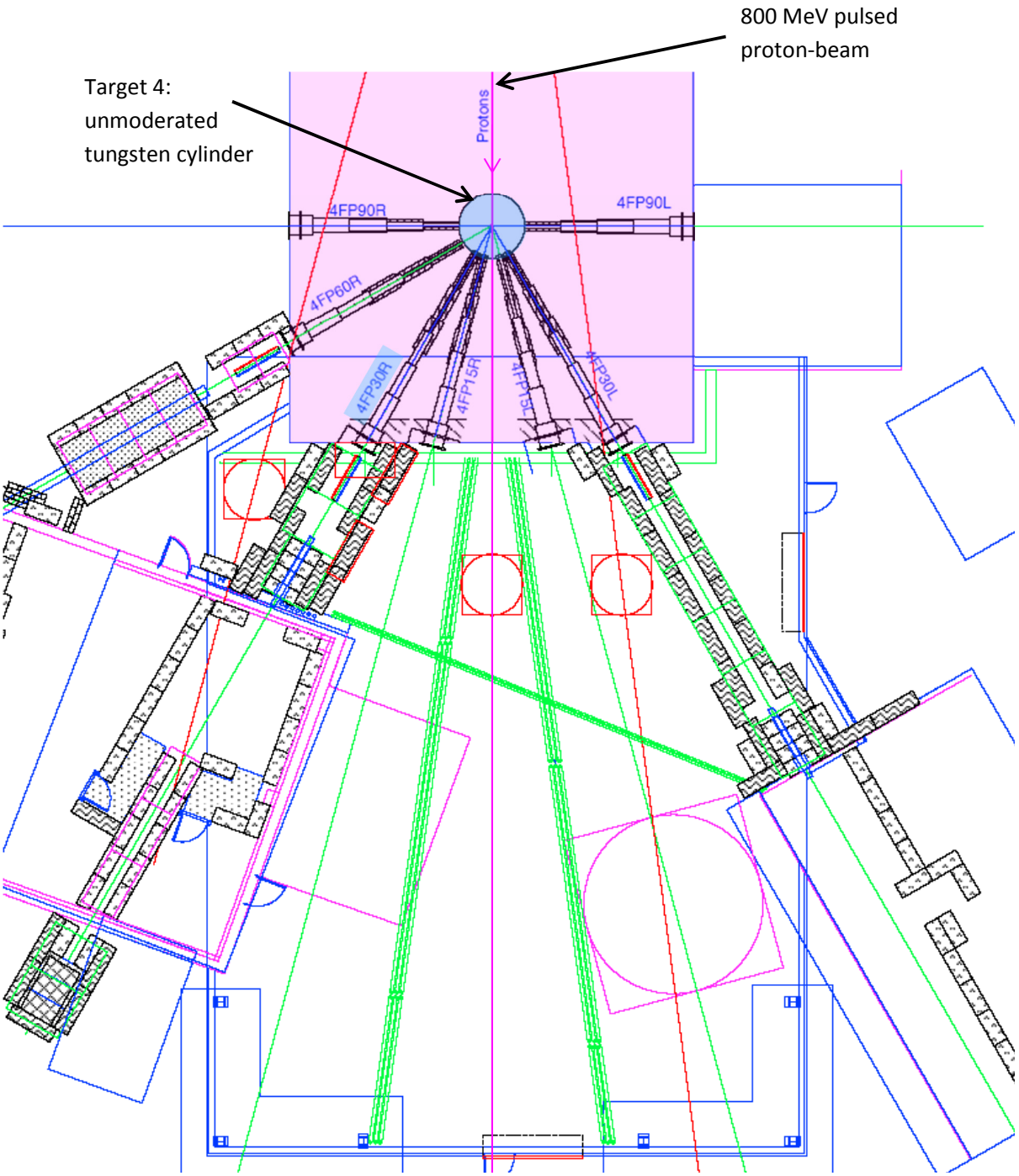

Figure 5.3: Neutrons with energies up to 800 MeV are produced at the LANSCE WNR facility by bombarding Target 4, an unmoderated tungsten cylinder, with an 800 MeV pulsed proton beam. The different neutron flight paths available at the WNR facility are labeled. Highlighted in blue is the flight path 30° to the right of the proton beam direction. This was used to irradiate the TeO_2 powder.

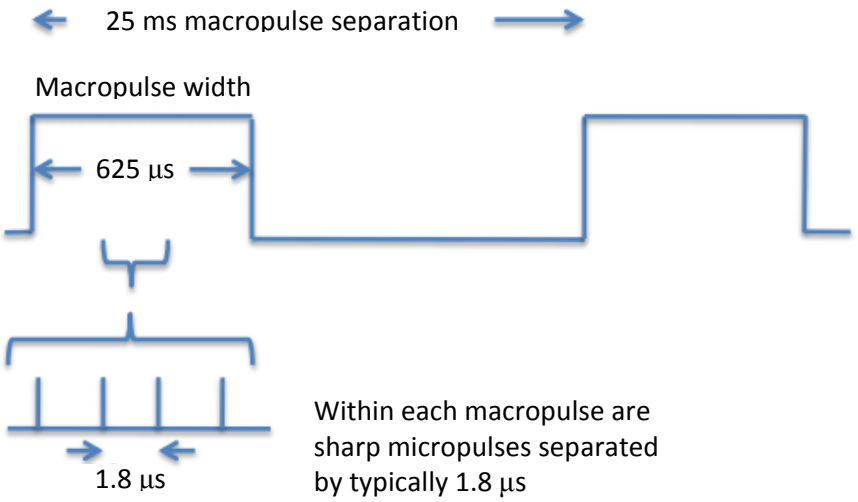

Figure 5.4: The time structure of the pulsed proton beam during the TeO_2 cross-section measurement. The beam consisted of 625-μs-long proton macropulses, each containing proton micropulses spaced 1.8 μs apart. The macropulses occurred at a rate of 40 Hz, which corresponds to a macropulse spacing of 25 ms.

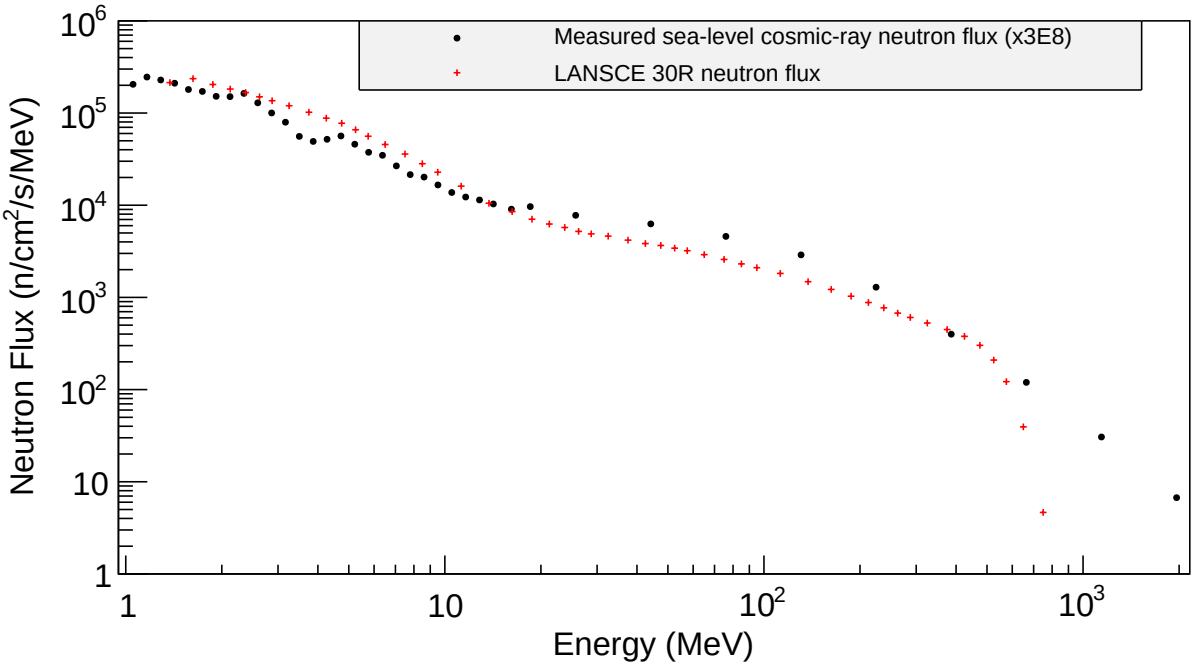

Figure 5.5: LANSCE 30R neutron flux (red crosses) compared with measured sea-level cosmic-ray neutron flux [81] (black dots), which has been multiplied by 3×10^8.

ionization chamber; L is equal to 13.885 m for the 30R flight path. When measuring the ToF, the neutron departure time from the tungsten is taken to be the proton-micropulse arrival time at the tungsten. To get the neutron spectrum, the WNR facility records the neutron fluence at the fission ionization chamber as a function of energy. Assuming non-relativistic kinematics, the neutron energy, E_n, can be calculated by inserting the ToF into the following equation:

$$E_n = \frac{1}{2} m_n \left(\frac{L}{\text{ToF}} \right)^2, \tag{5.15}$$

where m_n is the mass of a neutron. Then, for an energy bin with a central energy E_n and a width ΔE_n, the neutron fluence in the bin, $\Phi(E_n)\Delta E_n$, can be obtained from the number of fission pulses, $N_f(E_n)\Delta E_n$, produced in the fission ionization chamber:

$$\Phi(E_n)\Delta E_n = \frac{N_f(E_n)\Delta E_n}{\sigma_f \times \rho_f \times \epsilon_{\text{det}}}, \tag{5.16}$$

where σ_f is the ^{238}U fission cross section for a neutron with energy E_n, ρ_f is the areal density of ^{238}U nuclei in the ionization chamber, and ϵ_{det} is the efficiency of the ionization chamber for detecting events. The neutron-energy spectrum is recorded only for $E_n \geq$ 1.25 MeV because the ^{238}U fission cross section is very small below this threshold.

Once the neutron-energy spectrum is known, the total neutron flux, ϕ, impinging on the TeO_2 target can also be obtained in units of neutrons/(cm^2·s):

$$\phi = \frac{\Phi}{\pi \left(D/2\right)^2 \left(L_t/L\right)^2 \Delta t}, \tag{5.17}$$

where Φ is the total neutron fluence at the ionization chamber during an irradiation time Δt, D is the diameter of the neutron beam at the ionization chamber and is equivalent to the beam-collimation width, and L_t is the distance between the tungsten and the TeO_2 target. The total neutron flux is one of the parameters needed to obtain radioisotope-production cross sections for the TeO_2 powder.

The uncertainty in ϕ can be calculated from the uncertainties in the parameters from Equations 5.16 and 5.17. The ^{238}U-fission cross section has been experimentally measured for neutron energies from ∼1 eV to 380 MeV [84–86]. At LANSCE, measured cross sections are used to obtain the neutron flux. Above 200 MeV, the cross section is set equal its value at 200 MeV [87]. To be conservative, the uncertainty in σ_f is taken to be 5% at energies below 200 MeV and 50% at energies above 200 MeV. During the neutron irradiation, the statistical uncertainty in $N_f(E_n)\Delta E_n$ for each energy bin ranged from approximately 0.2 to 3%. The uncertainty in ϵ_{det} is estimated to be less than 2% [83]. Finally, the uncertainties in ρ_f, D, L_t, L, and Δt are all negligible compared with the other uncertainties discussed above and can be ignored. The uncertainty in the total neutron flux, $\Delta\phi$, can then be estimated using the following expressions:

$$\Delta[\Phi(E_n)\Delta E_n] = \Phi(E_n)\Delta E_n \sqrt{\left(\frac{\Delta[N_f(E_n)\Delta E_n]}{N_f(E_n)\Delta E_n} \right)^2 + \left(\frac{\Delta\sigma_f}{\sigma_f} \right)^2 + \left(\frac{\Delta\epsilon_{det}}{\epsilon_{det}} \right)^2}, \tag{5.18}$$

$$\Delta\Phi = \sum_n \Delta[\Phi(E_n)\Delta E_n], \tag{5.19}$$

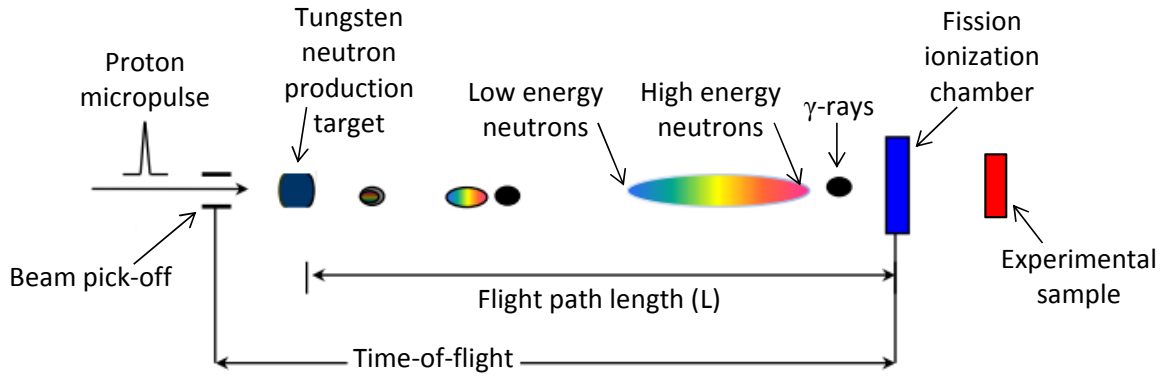

Figure 5.6: Neutron time-of-flight (ToF) at the WNR facility. A proton micropulse hits the tungsten neutron-production target. Neutrons, charged particles, and gamma-rays are produced. The charged particles are removed from the beam by magnets, and the remaining neutrons and gamma-rays travel a distance L to a fission ionization chamber located upstream of the experiment. The total traveling time of a neutron from the tungsten target to the ionization chamber is called the ToF. In a ToF measurement, the departure time of the neutron from the tungsten target is taken to be the arrival time of the proton micropulse at the tungsten target.

and

$$\Delta\phi = \phi\frac{\Delta\Phi}{\Phi}, \tag{5.20}$$

The parameters $\Delta[\Phi(E_n)\Delta E_n]$, $\Delta[N_f(E_n)\Delta E_n]$, $\Delta\sigma_f$, $\Delta\epsilon_{det}$, and $\Delta\Phi$ are the uncertainties of $\Phi(E_n)\Delta E_n$, $N_f(E_n)\Delta E_n$, σ_f, ϵ_{det}, and Φ, respectively. For the neutron irradiation at LANSCE, the uncertainty in the total neutron flux for $E_n \geq 1.25$ MeV is estimated to be $\sim$10%.

Parameters of the TeO_2 irradiation are given in Table 5.2. Since the ^{238}U fission ionization chamber tracks only neutrons with $E_n \geq 1.25$ MeV, Φ and ϕ in the table include only neutrons with $E_n \geq 1.25$ MeV.

5.4 Cross-section analysis

5.4.1 Gamma-counting and radioisotope identification

Approximately one week after the neutron irradiation, the TeO_2 target was dismantled, and each component was analyzed using gamma-ray spectroscopy [88] at the Lawrence Berkeley National Laboratory (LBNL) Low Background Facility (LBF) [89]. In gamma-ray spectroscopy, gamma rays emitted from a radioactive source are measured with a gamma detector such as HPGe. A spectrum is produced by collecting a histogram of the energy deposited in the detector by the gamma rays. Gammas that Compton scatter [88] in the detector and escape before depositing their full energy form a continuum in the gamma spectrum. Gammas depositing their full energy, E_γ, in the detector form peaks on top of the Compton continuum; each peak is centered at E_γ and spread by the resolution of the detector. Since gamma rays are characteristic of the decaying isotopes

Table 5.2: Parameters of TeO_2 irradiation.

Parameter	Value
Irradiation time (Δt)	154487 s
Distance between tungsten and ^{238}U fission ionization chamber (L)	13.885 m
Distance between tungsten and TeO_2 target (L_t)	14.139 m
Beam-collimation width	8.26 cm (3.25 in)
Beam diameter at ^{238}U fission ionization chamber (D)	8.26 cm
Beam diameter at TeO_2 target ($D\frac{L_t}{L}$)	8.41 cm
Total neutron fluence at ^{238}U fission ionization chamber for $E_n \geq 1.25$ MeV (Φ)	1.21×10^{13} neutrons
Neutron flux at TeO_2 target for $E_n \geq 1.25$ MeV (ϕ)	$(1.41 \pm 0.14) \times 10^6$ neutrons/(cm^2·s)

they come from, gamma-peak energies can be used to identify what radioisotopes are present in the measured source.

To identify the radioisotopes produced by neutron activation, each TeO_2 target component was gamma counted at the LBF. The TeO_2 powder, cadmium foils, and aluminum foils were measured using an upright, 115%, n-type HPGe detector [88]. The gold foils were measured with a horizontal, 80%, p-type HPGe detector [88]. The gold foils were each counted 12 cm away from the front of the detector. Their configuration is shown in Figure 5.7a. The cadmium and aluminum monitor foils were all counted in the configuration illustrated in Figure 5.7b, with the foil laid flat and centered on top of the detector. Prior to counting, the TeO_2 powder was mixed thoroughly and placed in a Marinelli beaker positioned over the top of the detector. A plastic insert was glued to the outer part of the inside of the beaker to decrease the thickness and increase the height of the powder in the beaker. This setup, illustrated in Figure 5.7c, was chosen because it increases the probability, or efficiency, for measuring gamma rays by minimizing the self-attenuation of gamma rays through the powder and by maximizing the solid angle of the detector seen by the powder. The TeO_2 was counted in this configuration periodically for six months to enable the observation of long-lived activation products after the short-lived ones decayed away. Figures 5.8a and 5.8b show gamma spectra for the TeO_2 powder collected one week and four months after the irradiation, respectively. The numerous peaks in the top spectrum come from the decays of neutron activated isotopes with half-lives as short as 1.39 d (^{131m}Te). In the bottom spectrum, fewer lines are present because the short-lived activation products have decayed away, leaving only products with half-lives greater than ∼12 d.

To determine the energies of the gamma rays emitted from the TeO_2 powder, each peak in the gamma spectra was fit with either a Gaussian or a Gaussian-like function summed with a quadratic function representing the Compton continuum. The peak-fitting was performed with the software RadWare [90]. Figure 5.9 shows an example of a peak fit with RadWare. Two parameters of interest given by the fit are the energy at the centroid of the peak (labeled "energy" in the figure) and the net number of counts in the peak (labeled "area"); the net counts is the total counts in the peak minus the continuous background. The peak energies from the fits were used to identify the radioisotopes

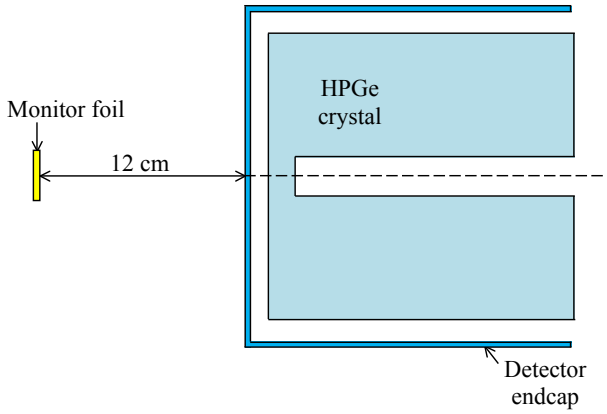

(a) Setup used to count each gold foil.

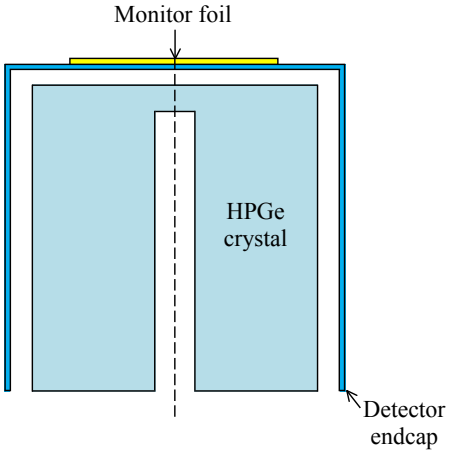

(b) Setup used to count each cadmium and aluminum foil.

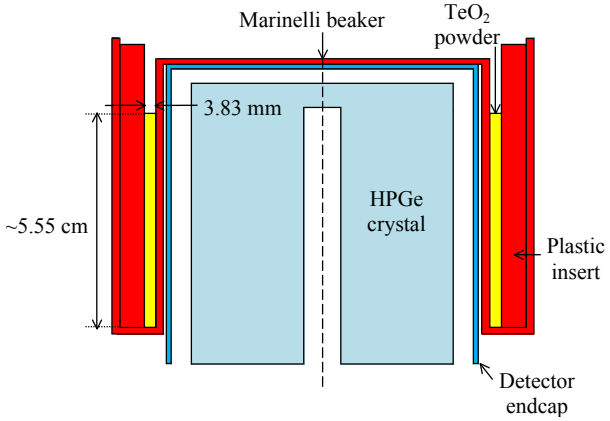

(c) Setup used to count TeO_2 powder.

Figure 5.7: Cross-sectional views of setups used to count monitor foils and TeO_2 powder. Everything is a cylinder with the axis along the long-dashed line.

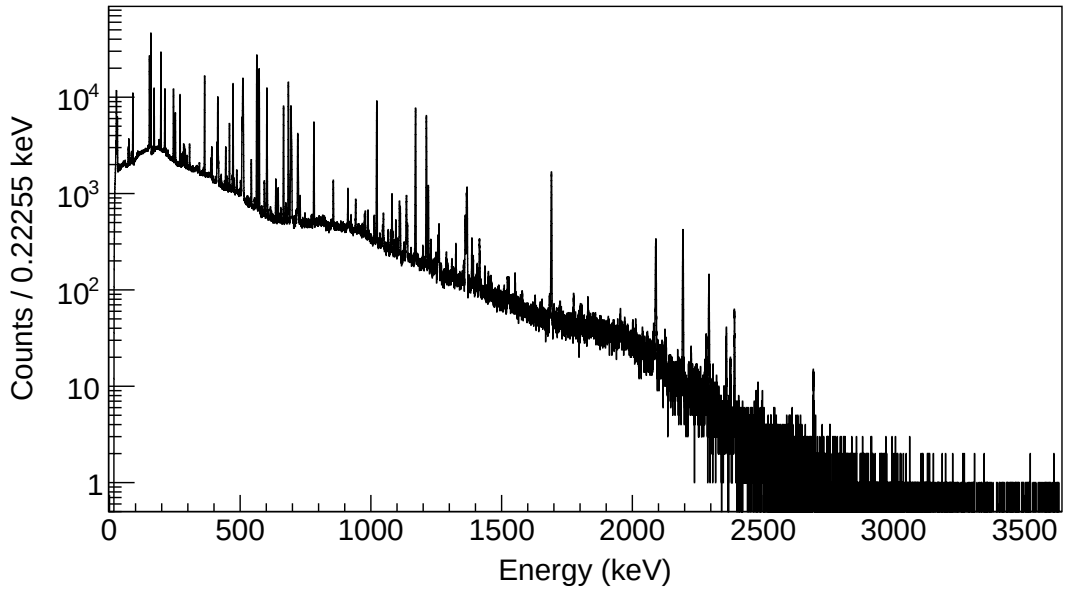

(a) 1-hour long spectrum collected one week after neutron irradiation.

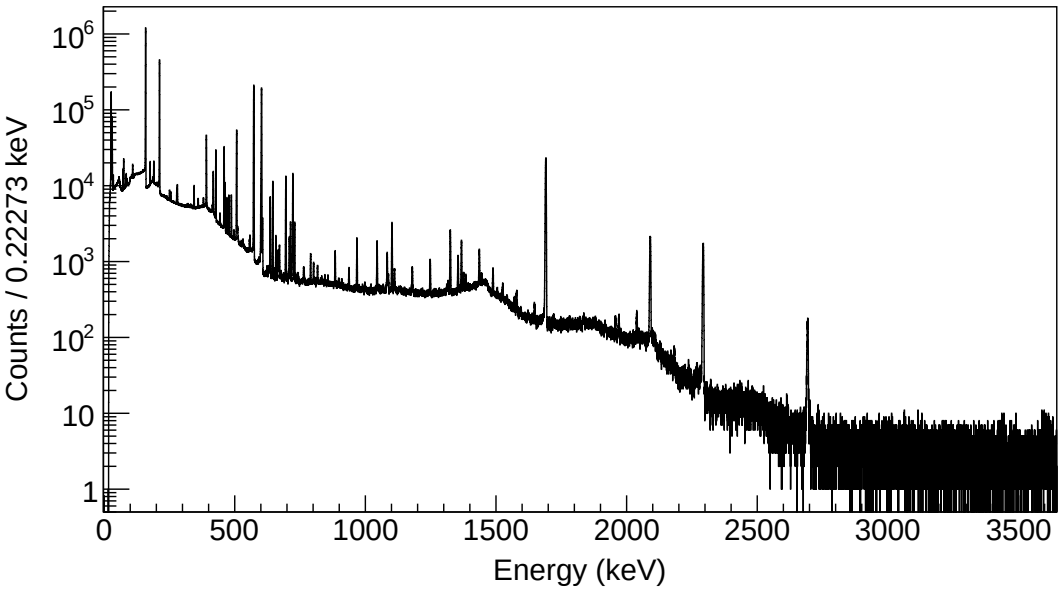

(b) 3-day long spectrum collected four months after neutron irradiation.

Figure 5.8: Gamma spectra collected for the TeO_2 powder.

present in the TeO_2 powder. Some gamma peaks could come from the decay of more than one isotope. In each of these cases, the count rate in the peak was plotted as a function of time. The count-rate curve was then fit with various functions describing the exponential decay of one or more isotopes. Isotopes contributing to the peak were deduced after finding the best fit.

A list of all radioisotopes observed in the TeO_2 powder is provided in column one of Table 5.3. For certain isotopes, production could occur in several different ways during the irradiation. ^{127m}Te, for example, could be directly produced from the reactions ^{126}Te(n,γ), ^{128}Te(n,2n), and ^{130}Te(n,4n). It could also be indirectly produced from the decay of ^{127}Sb, another isotope activated in the TeO_2 powder. Another example is ^{124}Sb, which could be produced during the irradiation in the following ways: (1) by neutron reactions such as ^{124}Te(n,p), ^{125}Te(n,d), and ^{126}Te(n,nd), or (2) from the isomeric transitions of the short-lived isotopes ^{124m1}Sb (93 s half-life) and ^{124m2}Sb (20.2 m half-life), which could both be created by neutron reactions such as those listed in (1). In Table 5.3, column two, Te(n,X) or O(n,X) are used to indicate that the isotope's presence in the TeO_2 is due to more than one type of reaction with tellurium or oxygen during the irradiation. The isotope ^{131m}Te is an exception in that it could only be produced via ^{130}Te(n,γ); this specific reaction is therefore reported in the table. Another exception is ^{126}I. Its presence in the TeO_2 powder was due to proton interactions with tellurium, i.e., Te(p,X). The protons were generated during the irradiation by neutron interactions with both tellurium and oxygen.

Since gamma counting started one week after the neutron irradiation ended, only neutron activated isotopes with half-lives (column four of Table 5.3) greater than $\sim$1 d could be observed. Those with shorter half-lives decayed away before counting began. Therefore, any isotope observed during the gamma measurement with a half-life less than $\sim$1 d has to be the decay daughter of another longer-lived isotope. Examples of these would be ^{127}Te and ^{129}Te, which were present during counting due to the decay of ^{127m}Te and ^{129m}Te, respectively.

In Table 5.3, isotopes in bold font all have Q-values (column three) greater than 2528 keV, which means they can contribute events to the $0\nu\beta\beta$ decay region. Looking at the half-lives, however, one can see that most of these isotopes have short half-lives and will not be present once CUORE begins counting. Assuming the TeO_2 crystals will have been underground for an average of $\sim$4 y before counting begins, only ^{110m}Ag has the potential to be an important source of background in CUORE.

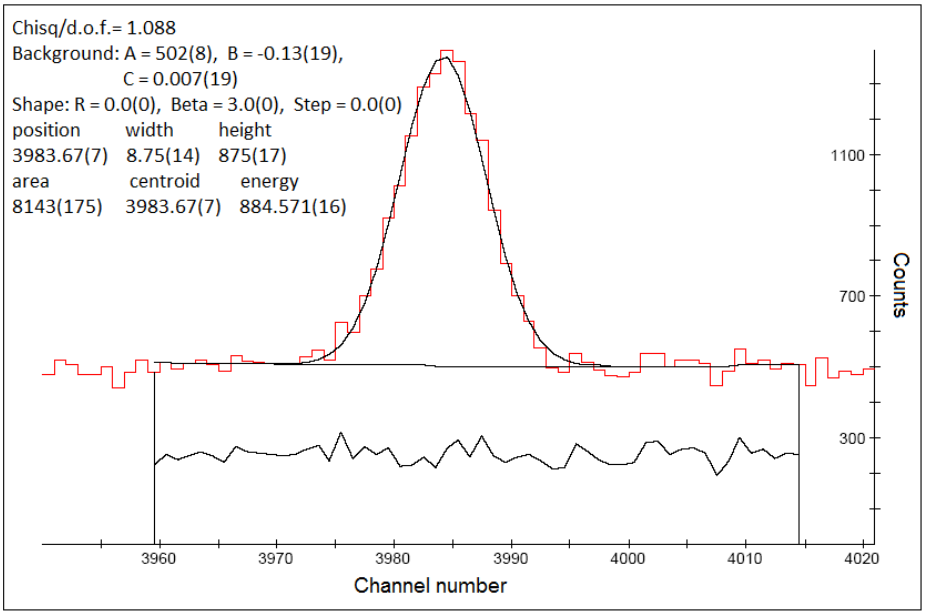

Figure 5.9: Example of a peak from a TeO_2 powder gamma spectrum being fit with RadWare. The spectrum is plotted with channel number along the x-axis and counts along the y-axis. The peak has been fit with a Gaussian summed with a quadratic representing the Compton continuum. The fit results provide the energy at the centroid of the peak (i.e., 884.571 keV) and the net number of counts in the peak (i.e., 8143 counts). The residual (i.e., data minus fit) in counts/channel is shown halfway between the spectrum and the x-axis.

Table 5.3: Radioisotopes observed in the TeO_2 powder. Reasons for each isotope's presence in the powder are given in column two. Decay Q-values for isotopes that can contribute to the $0\nu\beta\beta$ decay region are given in column three. The "ϵ" and "β^-" in parentheses stand for electron capture and beta-minus decay, respectively. Half-lives of all observed isotopes are listed in column four. The minimum threshold energy, E_{th}, for isotope production and the flux-averaged cross section, $\bar{\sigma}_{30R}$, are given in columns five and six for each isotope that has a half-life greater than ~1 day. For ^{120m}Sb, a lower limit on the cross section is given because GEANT4 is not able to properly simulate the decay of ^{120m}Sb. The lower limit was obtained by assuming no true coincidence summing occurs for the gamma ray of interest; in reality, this is not true. Superscripts i and c indicate whether the cross section is independent or cumulative, respectively. No cross sections were obtained for isotopes that were produced solely by indirect methods. Cross-sections are also not given for ^{121}Te and ^{131m}Te because the contribution of low energy ($\lesssim$0.1 MeV) neutrons to the production rates was too high. Finally, a cross section could not be obtained for ^{119}Sb because the strongest gamma line at 24 keV overlapped with x-rays emitted by other activated isotopes in the powder.

Isotope	Presence in TeO_2 due to:	Decay Q-value (MeV)	Half-life	E_{th} (MeV)	$\bar{\sigma}_{30R}$ (mb)
^{126}I	Te(p,X)		12.93 d		

Continued on next page

Table 5.3 – continued from previous page

Isotope	Presence in TeO_2 due to:	Q-value (MeV)	Half-life	E_{th} (MeV)	$\bar{\sigma}_{30R}$ (mb)
^{131}I	Te(n,X)		8.0252 d		
^{118}Te	Te(n,X)		6.00 d	18.0	5.7 ± 1.2^{i}
^{119m}Te	**Te(n,X)**	**2.554 (ϵ)**	**4.7 d**	**10.6**	**6.1 ± 0.8^{i}**
^{121}Te	Te(n,X)		19.17 d	0.0	—
^{121m}Te	Te(n,X)		164.2 d	0.0	16 ± 2^{i}
^{123m}Te	Te(n,X)		119.2 d	0.0	37 ± 5^{i}
^{125m}Te	Te(n,X)		57.4 d	0.0	84 ± 10^{i}
^{127}Te	Te(n,X)		9.35 h		
^{127m}Te	Te(n,X)		106.1 d	0.0	47 ± 10^{i}
^{129}Te	Te(n,X)		69.6 m		
^{129m}Te	Te(n,X)		33.6 d	0.0	53 ± 17^{c}
^{131}Te	Te(n,X)		25 m		
^{131m}Te	^{130}Te(n,γ)		33.25 h	0.0	—
^{131m}Xe	Te(n,X)		11.84 d		
^{118}Sb	**Te(n,X)**	**3.657 (ϵ)**	**3.6 m**		
^{119}Sb	Te(n,X)		38.19 h	5.0	—
^{120m}Sb	**Te(n,X)**	**2.681 + E_{ex} (ϵ)**	**5.76 d**	**> 0.2**	**$> 4.0 \pm 0.5^{i}$**
^{122}Sb	Te(n,X)		2.7238 d	1.2	14 ± 2^{c}
^{124}Sb	**Te(n,X)**	**2.904 (β^-)**	**60.2 d**	**2.1**	**15 ± 2^{c}**
^{125}Sb	Te(n,X)		2.75856 y	0.0	18 ± 2^{c}
^{126}Sb	**Te(n,X)**	**3.673 (β^-)**	**12.35 d**	**2.9**	**6.2 ± 0.8^{c}**
^{127}Sb	Te(n,X)		3.85 d	7.4	13 ± 2^{c}
^{113}Sn	Te(n,X)		115.09 d	27.9	2.5 ± 0.3^{c}
^{117m}Sn	Te(n,X)		14 d	0.0	4.2 ± 0.6^{i}
^{111}In	Te(n,X)		2.8047 d	34.8	2.1 ± 0.2^{c}
^{114m}In	Te(n,X)		49.51 d	10.4	1.8 ± 0.2^{i}
^{105}Ag	Te(n,X)		41.29 d	77.7	0.54 ± 0.06^{c}
^{106m}Ag	**Te(n,X)**	**3.055 (ϵ)**	**8.28 d**	**58.4**	**0.40 ± 0.08^{i}**
^{110}Ag	**Te(n,X)**	**2.893 (β^-)**	**24.56 s**		
^{110m}Ag	**Te(n,X)**	**3.010 (β^-)**	**249.83 d**	**13.9**	**0.26 ± 0.03^{i}**
^{111}Ag	Te(n,X)		7.45 d	11.2	0.42 ± 0.09^{c}
^{101m}Rh	Te(n,X)		4.34 d	80.0	0.29 ± 0.04^{c}
^{7}Be	O(n,X)		53.24 d	35.5	1.3 ± 0.1^{i}

5.4.2 Flux-averaged cross sections

Following the gamma counting and radioisotope identification, flux-averaged cross sections were obtained for all radioisotopes that have half-lives greater than ∼1 day. Of main interest was the cross section for ^{110m}Ag. In this analysis, the flux-averaged cross section, $\bar{\sigma}_{30R}$, for an isotope is defined as

$$\bar{\sigma}_{30R} \equiv \frac{\int_{E_{min}}^{E_{max}} \sigma(E)\varphi_{30R}(E)\mathrm{d}E}{\int_{E_{min}}^{E_{max}} \varphi_{30R}(E)\mathrm{d}E} = \frac{R_{30R}/(N\bar{T})}{\int_{E_{min}}^{E_{max}} \varphi_{30R}(E)\mathrm{d}E}. \tag{5.21}$$

The parameter $\sigma(E)$ is the cross section for producing the isotope when neutrons of energy E interact with target nuclei in the TeO_2 powder; it is identical to the $\sigma(E)$ that was introduced in Equation 5.7. The parameter $\varphi_{30R}(E)$ is the 30R differential neutron flux hitting the front of the target in units of neutrons/(cm^2·s·MeV), and E_{min} and E_{max} are respectively the lowest and highest neutron energies the TeO_2 powder was exposed to. On the right-hand side of the equation, R_{30R} is the isotope-production rate, which can be obtained using the gamma spectra collected for the TeO_2 powder; $\bar{T}$, like in Section 5.2, represents the average neutron transmission in the powder and will be explained later in this section; and N is the number of target nuclei in the powder. For the production of ^{7}Be during irradiation (refer to Table 5.3), N is the number of oxygen nuclei in the powder because ^{7}Be should be produced almost entirely by neutron interactions with oxygen. For all other radioisotopes activated in the powder, N is the number of tellurium nuclei.

For the 30R neutron beam, the lowest neutron energy is 0 MeV and the highest neutron energy is 800 MeV. However, a complication arises if E_{min} is 0 MeV: Equation 5.21 cannot be evaluated since the neutron flux during the experiment was not recorded for neutron energies less than 1.25 MeV. Appendix B discusses how the total flux below 1.25 MeV can be estimated using the two gold foils in the TeO_2 target. However, because the uncertainty in the flux was too large, the flux was not used in the cross-section analysis. Furthermore, it is not useful to evaluate a cross section that includes interactions with this flux because low-energy neutrons ($\lesssim$0.1 MeV) are primarily created by higher energy neutrons slowing down after interacting with nuclei in nearby materials. In other words, the flux at low energies is significantly affected by the surrounding environment. Fortunately, for most radioisotopes produced in the TeO_2 powder, $\sigma(E < 1.25\text{ MeV})$ is either equal to zero or negligible, which means we can write

$$\int_0^{800} \sigma(E)\varphi_{30R}(E)\mathrm{d}E \approx \int_{1.25}^{800} \sigma(E)\varphi_{30R}(E)\mathrm{d}E \tag{5.22}$$

Now, setting $E_{min} = 1.25$ MeV and $E_{max} = 800$ MeV, Equation 5.21 becomes

$$\bar{\sigma}_{30R} \equiv \frac{\int_{1.25}^{800} \sigma(E)\varphi_{30R}(E)\mathrm{d}E}{\int_{1.25}^{800} \varphi_{30R}(E)\mathrm{d}E} = \frac{R_{30R}/(N\bar{T})}{\int_{1.25}^{800} \varphi_{30R}(E)\mathrm{d}E}. \tag{5.23}$$

For almost every radioisotope with a half-life greater than ∼1 day, the cross section given by Equation 5.23 was determined. There are a few exceptions. First, no cross sections were obtained for isotopes that were produced solely by indirect methods. Cross sections were also not obtained for ^{121}Te and ^{131m}Te because the contribution of low energy neutrons to their production was uncertain. This will be discussed in more detail later. Finally, no cross section could be determined for ^{119}Sb because the strongest gamma line at 24 keV overlapped with x-rays emitted by other activated isotopes in the powder.

To know whether $\sigma(E < 1.25\text{ MeV})$ is small enough to be ignored, one must first look at the minimum kinetic energy, or threshold energy [80, 91], a neutron must have in order for isotope production to occur; if E is below the threshold energy, $\sigma(E)$ equals zero because the reaction cannot take place. During the irradiation, there were several different ways an isotope could be produced. ^{123m}Te, for example, could have been created by the reactions ^{122}Te(n,γ), ^{123}Te(n,n'), ^{124}Te(n,2n), ^{125}Te(n,3n), ^{126}Te(n,4n), ^{128}Te(n,6n), and ^{130}Te(n,8n). For each isotope, the web-based program Qtool [92] was used to identify possible modes of production. Threshold energies were calculated for each mode, and the lowest value obtained, i.e., minimum threshold energy, is listed in column five of

Table 5.3. For several isotopes, the minimum threshold energy is above 1.25 MeV, which means that $\sigma(E < 1.25 \text{ MeV})$ is equal to zero. There are eleven isotopes with thresholds less than 1.25 MeV, and for nine of these, one can show that $\sigma(E < 1.25 \text{ MeV})$ is very small. The metastable tellurium isotope ^{121m}Te, for example, has a threshold energy of 0 MeV. It is in an $\frac{11}{2}^-$ angular momentum state and is produced by neutron interactions with stable tellurium nuclei that are in either a 0^+ state (for ^{120}Te, ^{122}Te, ^{124}Te, ^{126}Te, ^{128}Te, and ^{130}Te) or a $\frac{1}{2}^+$ state (for ^{123}Te and ^{125}Te). For neutrons with $E < 1.25$ MeV, s-wave and p-wave neutron capture by ^{120}Te will dominate the production of ^{121m}Te. Directly producing a ^{121}Te nucleus in an $\frac{11}{2}^-$ state is impossible with an s-wave or p-wave capture reaction. This can be understood by looking at the total angular momentum, I', available to the system:

$$I' = I + s + l. \tag{5.24}$$

The parameter I is the angular momentum quantum number of the ^{120}Te nucleus and is equal to 0; s is the spin of the incoming neutron, which is $\frac{1}{2}$; and l is the orbital angular momentum quantum number of the neutron. For an s-wave reaction, $l = 0$, which, using angular momentum summing rules [93], gives $I' = \frac{1}{2}$. For a p-wave reaction, $l = 1$, which gives $I' = \frac{1}{2}, \frac{3}{2}$. None of these reactions provides enough angular momentum to create a nucleus in an $\frac{11}{2}^-$ state.

It is possible to produce ^{121m}Te indirectly from an s-wave or p-wave capture by first creating a ^{121}Te nucleus in an excited state. Using the following definition for parity [80]:

$$\pi' = \pi(-1)^l, \tag{5.25}$$

where π' is the parity of the entire system, π is the parity of the ^{120}Te nucleus, and l is the orbital angular momentum of the neutron, one determines that the excited ^{121}Te nucleus would have to be in a $\frac{1}{2}^+$, $\frac{1}{2}^-$, or $\frac{3}{2}^-$ state. The nucleus could then incrementally shift to states of higher and higher angular momentum through primarily M1, E1, and E2 gamma transitions [80]. However, transitioning to an $\frac{11}{2}^-$ state in this manner should have a very low probability. Thus, $\sigma(E < 1.25 \text{ MeV})$ should be small for ^{121m}Te. Analogous arguments can be made for ^{123m}Te, ^{125m}Te, ^{127m}Te, ^{129m}Te, ^{120m}Sb, ^{125}Sb, and ^{117m}Sn. For ^{122}Sb, its threshold energy, 1.2 MeV, is so close to 1.25 MeV that we can assume $\sigma(E < 1.25 \text{ MeV}) = 0$.

The final two radioisotopes to examine are ^{121}Te and ^{131m}Te. ^{121}Te is in a low angular momentum state, $\frac{1}{2}^+$, which makes it easy to produce through an s-wave or p-wave neutron capture by ^{120}Te. Since the flux below 1.25 MeV was not measured, the contribution of neutron capture to the entire flux-averaged cross section is uncertain. Therefore, no cross section was obtained for this isotope. ^{131m}Te is only produced by the reaction ^{130}Te(n,γ). Since neutrons with $E < 1.25$ MeV could participate significantly in these reactions, no cross section was obtained for ^{131m}Te either.

In the simplest case, where the radioisotope was not being fed by any other radioisotope *during or after* the irradiation, the flux-averaged cross section can be obtained by expressing the isotope-production rate, R_{30R}, in two different ways and then setting the two expressions equal to one another. The first expression can be acquired using equations analogous to Equations 5.7–5.14. We start with

$$\begin{aligned} R_{30R} &= \int_{z_{tf}}^{z_{tb}} \left(\frac{N}{z_{tb} - z_{tf}} \mathrm{d}z \right) \int_{1.25}^{800} \sigma(E) \varphi_{30R}(E) T(E, z) \mathrm{d}E \\ &= N \int_{1.25}^{800} \sigma(E) \varphi_{30R}(E) \frac{\int_{z_{tf}}^{z_{tb}} T(E, z) \mathrm{d}z}{z_{tb} - z_{tf}} \mathrm{d}E. \end{aligned} \tag{5.26}$$

The integration limits z_{tf} and z_{tb} in Equation 5.26 are described in Figure 5.2. During irradiation, neutrons from the 30R beam travel in the positive z-direction, which is indicated in the figure. The neutrons first impact the target stack at $z = 0$. After passing through various target components, they enter and leave the TeO_2 powder at $z = z_{tf}$ and $z = z_{tb}$, respectively. The parameter $T(E, z)$ is the fraction of incoming neutrons with energy E that survive after traveling a distance z through the target stack. Next, if we define

$$\bar{T}(E) \equiv \frac{\int_{z_{tf}}^{z_{tb}} T(E, z) \mathrm{d}z}{z_{tb} - z_{tf}}, \tag{5.27}$$

Equation 5.26 becomes

$$\begin{aligned} R_{30R} &= N \int_{1.25}^{800} \sigma(E) \varphi_{30R}(E) \bar{T}(E) \mathrm{d}E \\ &= N \int_{1.25}^{800} \sigma(E) \varphi_{30R}(E) \bar{T}(E) \mathrm{d}E \frac{\int_{1.25}^{800} \sigma(E) \varphi_{30R}(E) \mathrm{d}E}{\int_{1.25}^{800} \sigma(E) \varphi_{30R}(E) \mathrm{d}E}. \end{aligned} \tag{5.28}$$

If we define

$$\bar{T} \equiv \frac{\int_{1.25}^{800} \sigma(E) \varphi_{30R}(E) \bar{T}(E) \mathrm{d}E}{\int_{1.25}^{800} \sigma(E) \varphi_{30R}(E) \mathrm{d}E}, \tag{5.29}$$

Equation 5.28 becomes

$$\begin{aligned} R_{30R} &= N\bar{T} \int_{1.25}^{800} \sigma(E) \varphi_{30R}(E) \mathrm{d}E \\ &= N\bar{T} \int_{1.25}^{800} \sigma(E) \varphi_{30R}(E) \mathrm{d}E \frac{\int_{1.25}^{800} \varphi_{30R}(E) \mathrm{d}E}{\int_{1.25}^{800} \varphi_{30R}(E) \mathrm{d}E} \\ &= N\bar{T} \bar{\sigma}_{30R} \int_{1.25}^{800} \varphi_{30R}(E) \mathrm{d}E. \end{aligned} \tag{5.30}$$

The second expression for R_{30R} uses data from the gamma spectra collected for the TeO_2 powder. We start with the radioisotope's activity, A_0, at the end of irradiation:

$$A_0 = R_{30R}[1 - \exp(-\lambda t_{irrad})], \tag{5.31}$$

where λ is the decay constant of the isotope and t_{irrad} is the neutron irradiation time. The number of decays, N_d, that occur during gamma-counting can be expressed as

$$N_d = \frac{A_0}{\lambda}[\exp(-\lambda t_s) - \exp(-\lambda t_e)], \tag{5.32}$$

where t_s and t_e are respectively the start time and end time of gamma-counting relative to the end of irradiation. If the isotope emits a gamma of energy E_γ during decay, the net number of counts, C_γ, in the spectrum peak at E_γ can be written as

$$C_\gamma = N_d B_\gamma \epsilon_\gamma, \tag{5.33}$$

where B_γ is the isotope's branching ratio [88] (as a fraction of 100%) for emitting a gamma with energy E_γ and ϵ_γ is the photopeak efficiency [88] at energy E_γ. The photopeak efficiency will be discussed in detail in Section 5.4.4. Using Equations 5.31–5.33, the production rate can be expressed as

$$R_{30R} = \frac{\lambda C_\gamma}{B_\gamma \epsilon_\gamma [\exp(-\lambda t_s) - \exp(-\lambda t_e)][1 - \exp(-\lambda t_{irrad})]} \tag{5.34}$$

Setting Equation 5.30 equal to Equation 5.34 gives

$$N\bar{T}\bar{\sigma}_{30R} \int_{1.25}^{800} \varphi_{30R}(E)\mathrm{d}E = \frac{\lambda C_\gamma}{B_\gamma \epsilon_\gamma [\exp(-\lambda t_s) - \exp(-\lambda t_e)][1 - \exp(-\lambda t_{irrad})]}, \tag{5.35}$$

which allows the flux-averaged cross section to be written as

$$\bar{\sigma}_{30R} = \frac{\lambda C_\gamma}{N\bar{T}[\int_{1.25}^{800} \varphi_{30R}(E)\mathrm{d}E] B_\gamma \epsilon_\gamma [\exp(-\lambda t_s) - \exp(-\lambda t_e)][1 - \exp(-\lambda t_{irrad})]}. \tag{5.36}$$

For most radioisotopes produced in the TeO_2 powder, Equation 5.36 can be used to obtain $\bar{\sigma}_{30R}$. However, there exist several cases where more complicated growth and decay equations [80] must be used.

In the cross-section equations used in this analysis, all parameters except for $\bar{T}$ and ϵ_γ are known. The photopeak efficiency, ϵ_γ, is the parameter more challenging to obtain. As shown in Equation 5.33, ϵ_γ is the net number of counts detected in the peak at E_γ divided by the number of gammas with energy E_γ emitted by the source. Photopeak efficiencies can often be determined experimentally; however, for many of the isotopes being analyzed, this is difficult to do because the isotopes have complicated decay schemes that result in substantial *true coincidence gamma summing* [88, 94], a process that will be discussed in Section 5.4.4. Therefore, GEANT4 [95, 96] has been used to simulate the TeO_2 powder counting-setup and to obtain photopeak efficiencies that take into account the complex summing that can occur. The next two sections discuss how $\bar{T}$ was determined from aluminum and cadmium monitor foil data and how ϵ_γ was obtained from measurements and GEANT4 simulations.

5.4.3 Attenuation of neutron beam during irradiation

During the neutron irradiation, aluminum and cadmium monitor foils were located in front of and behind the TeO_2 powder. These foils were gamma counted following the irradiation, and the spectra for foils Al1, Al3, Cd1, and Cd2 (located as shown in

Figure 5.2) were used to analyze the neutron transmission through the powder. Three of the activation reactions observed in the foils, along with their minimum threshold energies, are listed in Table 5.4. For each activation product, the production rates in the front foils (Al1, Cd1) and back foils (Al3, Cd2) can be given by Equations 5.37 and 5.38, respectively:

$$R_f = N_f \int_0^{800} \sigma(E)\varphi_{30R}(E)\mathrm{d}E = N_f \int_{1.25}^{800} \sigma(E)\varphi_{30R}(E)\mathrm{d}E \tag{5.37}$$

$$R_b = N_b \int_0^{800} \sigma(E)\varphi_{30R}(E)T_b(E)\mathrm{d}E = N_b \int_{1.25}^{800} \sigma(E)\varphi_{30R}(E)T_b(E)\mathrm{d}E. \tag{5.38}$$

Here, $R_{f(b)}$ is the production rate in the front (back) foil. $N_{f(b)}$ is the number of target nuclei in the front (back) foil; for the cadmium foils, the target nucleus is any cadmium nucleus, and for the aluminum foils, the target nucleus is ^{27}Al. $T_b(E)$ is the fraction of incoming neutrons with energy E that reach the back foil. The integral limits on right-hand side of each equation can be used because the minimum threshold energies for the activation products in Table 5.4 are all greater than 1.25 MeV. Finally, since neutron attenuation for $E > 1.25$ MeV was small through each target component upstream of the TeO_2 powder (Figure 5.10), Equation 5.37 assumes that 100% of neutrons reach Al1 and Cd1.

For each activation product, Equation 5.34 can be used to get R_f and R_b. Then, after taking the ratio R_b/R_f, an average value, $\bar{T}_b$, can be obtained for T_b:

$$\begin{aligned} \bar{T}_b &\equiv \frac{\int_{1.25}^{800} \sigma(E)\varphi_{30R}(E)T_b(E)\mathrm{d}E}{\int_{1.25}^{800} \sigma(E)\varphi_{30R}(E)\mathrm{d}E} \\ &= \left(\frac{C_{\gamma,b}}{C_{\gamma,f}}\right)\left(\frac{N_f}{N_b}\right)\left[\frac{\exp(-\lambda t_{s,f}) - \exp(-\lambda t_{e,f})}{\exp(-\lambda t_{s,b}) - \exp(-\lambda t_{e,b})}\right]\left(\frac{\epsilon_{\gamma,f}}{\epsilon_{\gamma,b}}\right), \end{aligned} \tag{5.39}$$

where parameters with subscripts f and b correspond to the front and back foils, respectively. All of the foils were counted in the same configuration (Figure 5.7b), and since for both cadmium and aluminum, the front and back foils are very similar in diameter and thickness, the following approximation was made: $\epsilon_{\gamma,f} = \epsilon_{\gamma,b}$. The values of $\bar{T}_b$ obtained by analyzing each activation product are given in Table 5.4. The uncertainty quoted for $\bar{T}_b$ was calculated by adding the uncertainties in $C_{\gamma,f}$, $C_{\gamma,b}$, N_f, and N_b in quadrature [97]. Uncertainties in the other parameters in Equation 5.39 were small enough to be ignored.

The data in Table 5.4 have been used to calculate $\bar{T}$. Recall the definition of $\bar{T}(E)$ given by Equation 5.27:

$$\bar{T}(E) \equiv \frac{\int_{z_{tf}}^{z_{tb}} T(E,z)\mathrm{d}z}{z_{tb} - z_{tf}}.$$

$\bar{T}(E)$ is the average fraction of neutrons with energy E that make it to any region of the TeO_2 powder. Since neutron attenuation through all monitor foils and the plastic container was small for $E > 1.25$ MeV, the following approximation can be made:

Table 5.4: Neutron transmission results. Reactions used to determine the transmission through the TeO_2 powder are listed in column one. The minimum threshold energy for each reaction is given in column two, and the value of $\bar{T}_b$ obtained from each reaction is given in column three.

Reaction	Minimum Threshold Energy (MeV)	$\bar{T}_b$
^{27}Al(n,X)^{22}Na	23.4	0.98 ± 0.03
Cd(n,X)^{105}Ag	5.2	0.84 ± 0.01
Cd(n,X)^{110m}Ag	2.2	0.86 ± 0.01

$$T(E > 1.25 \text{ MeV}, z = z_{tf}) = 1. \tag{5.40}$$

$\bar{T}(E)$ can then be estimated to be

$$\bar{T}(E) \simeq \frac{1 + T_b(E)}{2}. \tag{5.41}$$

Plugging Equation 5.41 into Equation 5.29 gives

$$\begin{aligned} \bar{T} &\simeq \frac{\int_{1.25}^{800} \sigma(E)\varphi_{30R}(E)\frac{1+T_b(E)}{2}\mathrm{d}E}{\int_{1.25}^{800} \sigma(E)\varphi_{30R}(E)\mathrm{d}E} \\ &= \frac{1+\bar{T}_b}{2}. \end{aligned} \tag{5.42}$$

Looking at Equations 5.29 and 5.39, one can see that $\bar{T}$ and $\bar{T}_b$ are isotope dependent; their values are decided by the shape of $\sigma(E)\varphi_{30R}(E)$. To simplify this issue, we first examine the value of $\bar{T}_b$ obtained using the reaction ^{27}Al(n,X)^{22}Na. The result $\bar{T}_b = 0.98 \pm 0.03$ is statistically consistent with 1. Since the minimum threshold energy for the reaction is 23.4 MeV, one can conclude that ∼100% of neutrons with $E > 23.4$ MeV are fully transmitted through the TeO_2 powder, while losing no energy. Thus for activation products in the powder that have threshold energies greater than 23.4 MeV, $\bar{T}_b$ has been set equal to 1. For activation products with threshold energies less than 23.4 MeV, $\bar{T}_b$ has been set equal to 0.90 ± 0.10. This range was chosen because it includes the three $\bar{T}_b$ values in Table 5.4, while also taking into account their uncertainties. This range was also made a little wider than the $\bar{T}_b$ values suggest for the sake of being conservative. The value of $\bar{T}$ is then calculated using the approximation:

$$\bar{T} = \frac{1 + (0.90 \pm 0.10)}{2} = 0.95 \pm 0.05 \tag{5.43}$$

5.4.4 Photopeak efficiency

For a gamma source being measured by a gamma detector, the photopeak efficiency, ϵ_γ, for a gamma ray with energy E_γ can be expressed as

$$\epsilon_\gamma = \frac{\text{Net counts detected in peak at } E_\gamma}{\text{Number of gammas with energy } E_\gamma \text{ emitted by source}}. \tag{5.44}$$

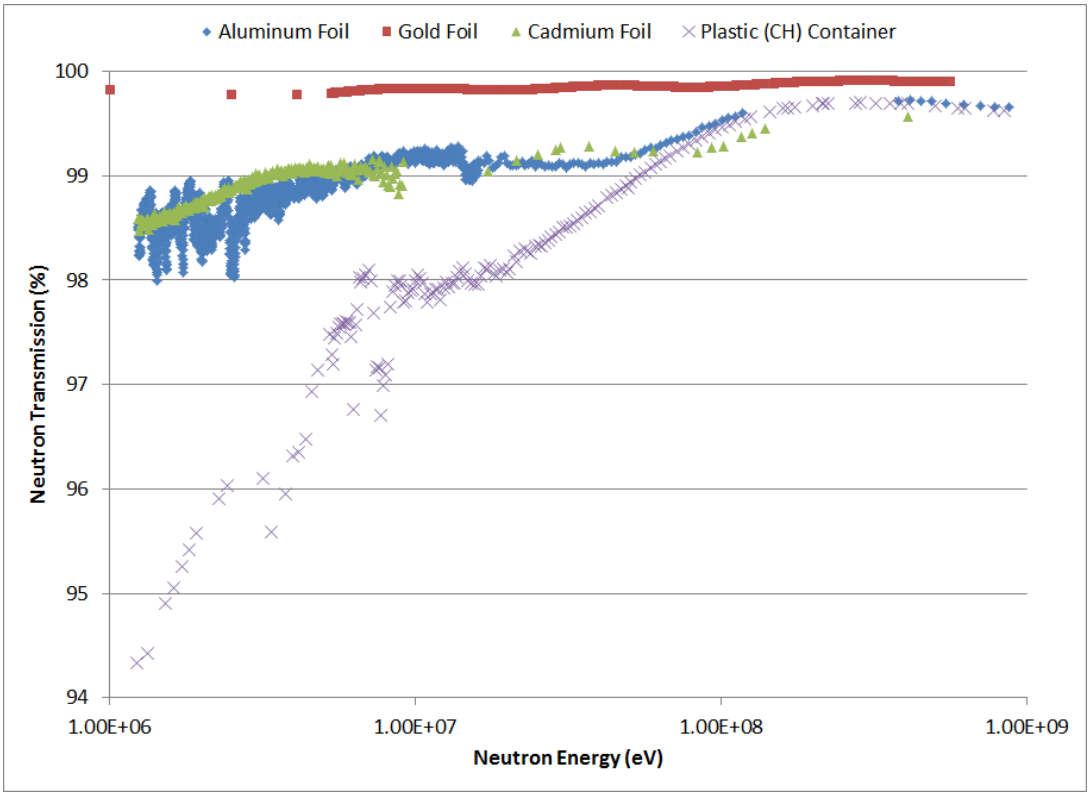

Figure 5.10: Neutron transmission through the plastic container as well as through each aluminum, gold, and cadmium foil in the TeO_2 target; uncertainties are on the order of the size of the data points. The neutron transmission (in %) through each component was estimated to be $\exp(-\Sigma_{tot}\Delta z) \times (100\%)$, where Δz is the thickness of the component in the direction of the neutron beam and Σ_{tot} is the total neutron-interaction cross section for the component material. For the plastic container, Σ_{tot} of the compound CH was used. All cross sections were obtained from measured data [10]. Linear interpolation was performed to get cross sections at energies where measurements were not available. This estimate underpredicts the neutron transmission because it assumes every neutron interaction removes the neutron from the beam. This is not the case for high energy neutrons, which mostly maintain their initial direction after an interaction.

In the case of the irradiated TeO_2 powder, many of the gammas used to obtain flux-averaged cross sections were either rarely or never emitted *in coincidence* (i.e., simultaneously) with another gamma. For these gammas, the photopeak efficiencies can be obtained experimentally using the so-called natural source calibration method from Ref. [98]. In this method, one first creates a source of known activity that ideally reproduces the physical properties (e.g., geometry and density) of the sample. The source should then be counted in the same configuration and with the same detector used to count the sample.

To obtain ϵ_γ for the TeO_2 powder, an extended source (named ES1) was created that consisted of a powder mixture inside a Marinelli beaker; refer to Figure 5.11c and Table 5.5. The Marinelli beaker was identical to the one used to hold the TeO_2 powder. The physical properties of ES1 did not exactly reproduce those of the TeO_2 powder. The height of the powder in ES1 was ~5.75 cm, whereas the height of the TeO_2 powder was ~5.55 cm (Figure 5.7c). The densities were also different. ES1 had a density of ~1.3 g/cm^3, while the TeO_2 powder had a density of ~3.9 g/cm^3. Other measurements

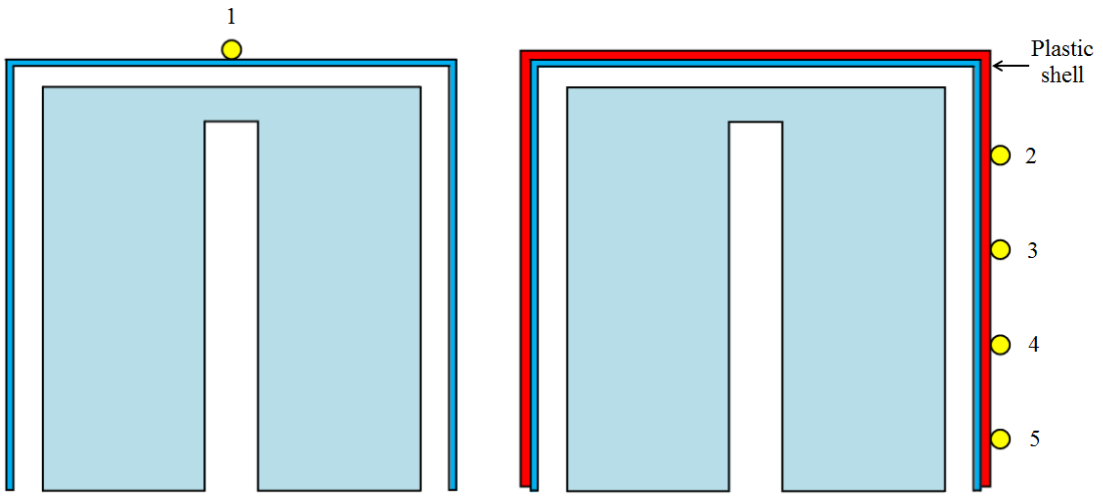

(a) Locations of point sources: (1) center of detector face, (2) 1.9 cm below detector face, (3) 3.9 cm below detector face, (4) 5.9 cm below detector face, (5) 7.9 cm below detector face.

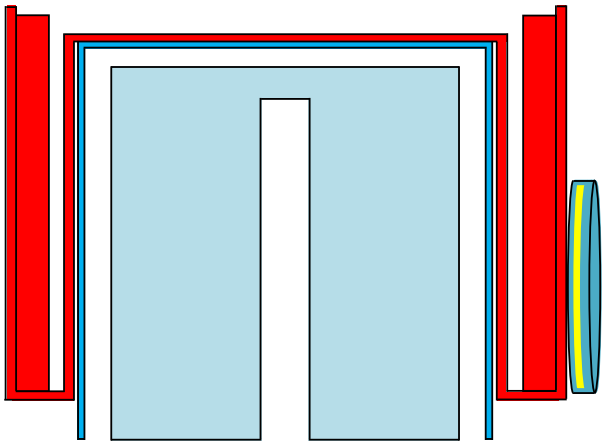

(b) Configuration of uranium-ore source measurement.

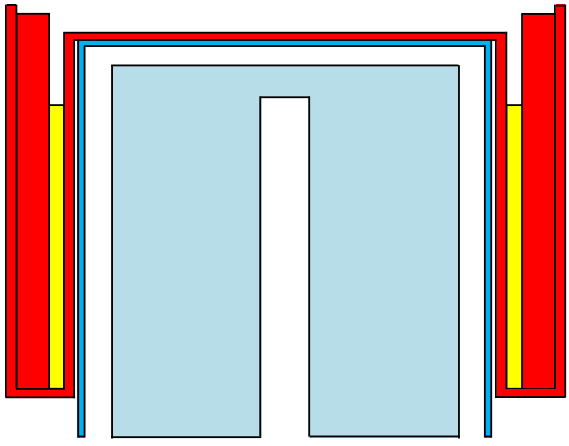

(c) Configuration of extended source measurements.

Figure 5.11: Gamma-source measurements. All sources are in yellow.

Table 5.5: Description of gamma sources used to benchmark GEANT4.

Source	Composition	Dimensions
Co-57	Co-57	Point source
Mn-54	Mn-54	Point source
Uranium ore	Natural uranium (0.1176 g)	Diameter = 4.76 cm
	mixed with epoxy	Thickness = 3.175 mm
ES1	La_2O_3 powder (89 g),	Inner radius = 5.06 cm
	Lu_2O_3 powder (2 g),	Outer radius = 5.443 cm
	KCl powder (4 g)	Average height = 5.75 cm
ES2	(Unirradiated) TeO_2 powder (228 g),	Inner radius = 5.06 cm
	La_2O_3 powder (23 g),	Outer radius = 5.443 cm
	Lu_2O_3 powder (6 g),	Average height = 6.5 cm
	K_2SO_4 powder (14 g)	

Table 5.6: Gamma lines for which photopeak efficiencies were obtained. Listed are the source of the gamma, the specific isotope that emits the gamma, the energy of the gamma, and the branching ratio of the gamma.

Source	Isotope	Gamma Energy (keV) [99]	Branching Ratio (%) [99]
^{57}Co	^{57}Co	122.06	85.60 ± 0.17
^{57}Co	^{57}Co	136.47	10.68 ± 0.08
^{54}Mn	^{54}Mn	834.85	99.9760 ± 0.0010
Uranium ore	^{235}U	185.72	57.2 ± 0.8
Uranium ore	^{210}Pb	46.54	4.25 ± 0.04
Uranium ore	^{226}Ra	186.21	3.64 ± 0.04
Uranium ore	^{214}Pb	242.00	7.251 ± 0.016
Uranium ore	^{214}Pb	295.22	18.42 ± 0.04
Uranium ore	^{214}Bi	1764.49	15.30 ± 0.03
Uranium ore	^{214}Bi	2204.06	4.924 ± 0.018
ES1, ES2	^{176}Lu	201.83	78.0 ± 2.5
ES1, ES2	^{176}Lu	306.78	93.6 ± 1.7
ES1, ES2	^{138}La	788.74	34.4 ± 0.5
ES1, ES2	^{138}La	1435.80	65.6 ± 0.5
ES1, ES2	^{40}K	1460.82	10.66 ± 0.18
ES1, ES2	^{223}Ra	269.46	13.9 ± 0.3
ES1, ES2	^{219}Rn	271.23	10.8 ± 0.6
ES1, ES2	^{211}Pb	832.01	3.52 ± 0.06
ES1, ES2	^{211}Bi	351.07	13.02 ± 0.12

discussed later in this section show that these differences do not substantially affect the photopeak efficiencies. ES1 was comprised of 89 g of La_2O_3 powder, 2 g of Lu_2O_3 powder, and 4 g of KCl powder that were mixed together thoroughly before being placed in the beaker. La_2O_3, Lu_2O_3, and KCl respectively contain the long-lived radioisotopes ^{138}La, ^{176}Lu, and ^{40}K, whose major gamma lines are listed in Table 5.6 along with their branching ratios. The activity A of each radioisotope was obtained using

$$A = \lambda \frac{M}{W} N_A \eta a, \tag{5.45}$$

where λ is the decay constant of the radioisotope, M is the mass of the powder containing the radioisotope, W is the molar mass of the powder compound, N_A is the Avogadro constant, η is the stoichiometric coefficient of the element (La, Lu, or K), and a is the natural abundance of the radioisotope in the element. ES1 was counted in the same configuration and with the same detector used to count the TeO_2 powder. A gamma spectrum was collected for approximately 1 day, which was long enough to detect more than 10,000 net counts in each peak from ^{138}La, ^{176}Lu, and ^{40}K; this ensured a statistical uncertainty of less than 1% in the net counts. The 789-keV and 1461-keV peaks from ^{138}La and ^{40}K were used to obtain photopeak efficiencies. The 789-keV gamma was chosen because it is not emitted in coincidence with any other gammas. The 1461-keV gamma was chosen because from the point of view of the detector, it is emitted alone; the x-rays it is in coincidence with have energies $\leq$ 3 keV and will be absorbed in other materials before reaching the detector. The 1436-keV line was not used because when ^{138}La decays by electron capture, the gamma is emitted in coincidence with x-rays 32 - 37 keV and lower. The 202-keV and 307-keV gammas from ^{176}Lu were also not used because they are emitted in coincidence with each other and with an 88-keV gamma (14.5% branching ratio). The 202-keV, 307-keV, and 88-keV gammas all have the probability to internally convert [80] as well, resulting in the production of x-rays 55 - 65 keV and below. The 202-keV and 307-keV gammas can therefore also be in coincidence with these x-rays. Since ES1 was counted very close to the detector, true coincidence summing, which will be discussed shortly, caused the efficiencies at 1436 keV, 202 keV and 307 keV to be lower than they would be if the gammas were emitted one at a time. The efficiencies at 789 keV and 1461 keV were obtained using

$$\epsilon_\gamma = \frac{C_\gamma}{A B_\gamma t}, \tag{5.46}$$

where C_γ is the net counts in the gamma peak, B_γ is the branching ratio of the gamma divided by 100%, and t is the total live time of the measurement.

Due to a small ^{227}Ac contamination in the La_2O_3, ES1 also contained ^{227}Ac and its daughter isotopes. A few of these isotopes emit gammas that are either rarely or never in coincidence with other gammas or x-rays. The gammas for which photopeak efficiencies were obtained are listed in Table 5.6; these are 269 keV (^{223}Ra), 271 keV (^{219}Rn), 351 keV (^{211}Bi), and 832 keV (^{211}Pb). These gammas had strong peaks in the spectrum; each peak had more than 10,000 net counts. For these gammas, efficiencies could not be as easily obtained because the activity of ^{227}Ac in ES1 was not readily known. The activity was determined in the following way. First, because the La_2O_3 powder was made more than six months prior to measuring the extended sources, ^{227}Ac was assumed to be in secular equilibrium with its daughters. The reasoning behind this assumption can be understood

by looking at the decay chain of ^{227}Ac (Figure 5.12). All isotopes will be in secular equilibrium when ^{227}Th reaches secular equilibrium with ^{227}Ac. Six months, or ten ^{227}Th half-lives, is enough time for this to happen. Secular equilibrium means that the ^{227}Ac daughters listed in Table 5.6 all have the same activity. This activity was determined by first obtaining the photopeak efficiency for one of the daughter gammas: 832 keV. This gamma has no coincidence summing. Therefore its efficiency could be determined by interpolating between the efficiencies at 789 keV and 1461 keV. The interpolation was performed after fitting the following curve to the efficiencies at 789 keV and 1461 keV:

$$\epsilon_\gamma = \exp\left[a + b\ln(E_\gamma)\right], \tag{5.47}$$

where the parameters a and b are fitting constants. Equation 5.47 is commonly used to describe the photopeak efficiency as a function of gamma energy [94]. Other functions could have been used as well; however, fitting with Equation 5.47 provided a satisfactory estimate of the photopeak efficiency at 832 keV. The curve fit was performed by implementing the least squares method [97, 100] in ROOT [101], a C++-based data-analysis software program. The results are shown in Figure 5.13a. ROOT also outputs the error matrix for a and b:

$$\Sigma = \begin{bmatrix} \sigma_a^2 & \sigma_{ab} \\ \sigma_{ba} & \sigma_b^2 \end{bmatrix}, \tag{5.48}$$

where σ_a is the uncertainty in a, σ_b is the uncertainty in b, and σ_{ab} (equivalent to σ_{ba}) is the covariance [97, 100] of a and b. For the 832-keV gamma the photopeak efficiency was obtained by plugging a and b from the fit into Equation 5.47 and setting $E_\gamma = 832$. The uncertainty in the efficiency, σ_γ, can be determined using

$$\sigma_\gamma = \sqrt{\left(\frac{\partial\epsilon_\gamma}{\partial a}\right)^2\sigma_a^2 + \left(\frac{\partial\epsilon_\gamma}{\partial b}\right)^2\sigma_b^2 + 2\left(\frac{\partial\epsilon_\gamma}{\partial a}\right)\left(\frac{\partial\epsilon_\gamma}{\partial b}\right)\sigma_{ab}}. \tag{5.49}$$

The resulting photopeak efficiency for the 832-keV gamma was 0.057 ± 0.001. Plugging this value into Equation 5.46 gives an ^{227}Ac activity of $A = 156 \pm 4$ Bq. Then, plugging the latter activity into Equation 5.46 gives the photopeak efficiencies for the other three ^{227}Ac daughter gammas in Table 5.6.

The ES1 photopeak efficiencies from 269 keV to 1461 keV are plotted in Figure 5.14 and have been fit with Equation 5.47. For the TeO_2 powder, photopeak efficiencies for gammas between 269 keV and 1461 keV can be obtained by plugging the gamma energy into Equation 5.47, with a and b equal to the values from the fit.

A second extended source (named ES2) was made to examine the effects of density and geometry (i.e., powder height) on the photopeak efficiencies. It was comprised primarily of (unirradiated) TeO_2 powder, but also contained small amounts of La_2O_3, Lu_2O_3, and K_2SO_4 powders; refer to Table 5.5. The powders were mixed thoroughly before being placed in a Marinelli beaker identical to the one used to hold the irradiated TeO_2 powder. The density of ES2 was $\sim$3.3 g/cm^3, close to that of the TeO_2 powder; however the height, 6.5 cm, was almost 1 cm higher than that of the TeO_2 powder. ES2 was gamma counted in the same configuration and with the same detector used to count the TeO_2 powder. The photopeak efficiencies at 789 keV and 1461 keV were obtained in the same way they were for ES1. The 202-keV, 307-keV, and 1436-keV lines were once again not used because of true coincident summing effects. Since the same La_2O_3 powder used in ES1

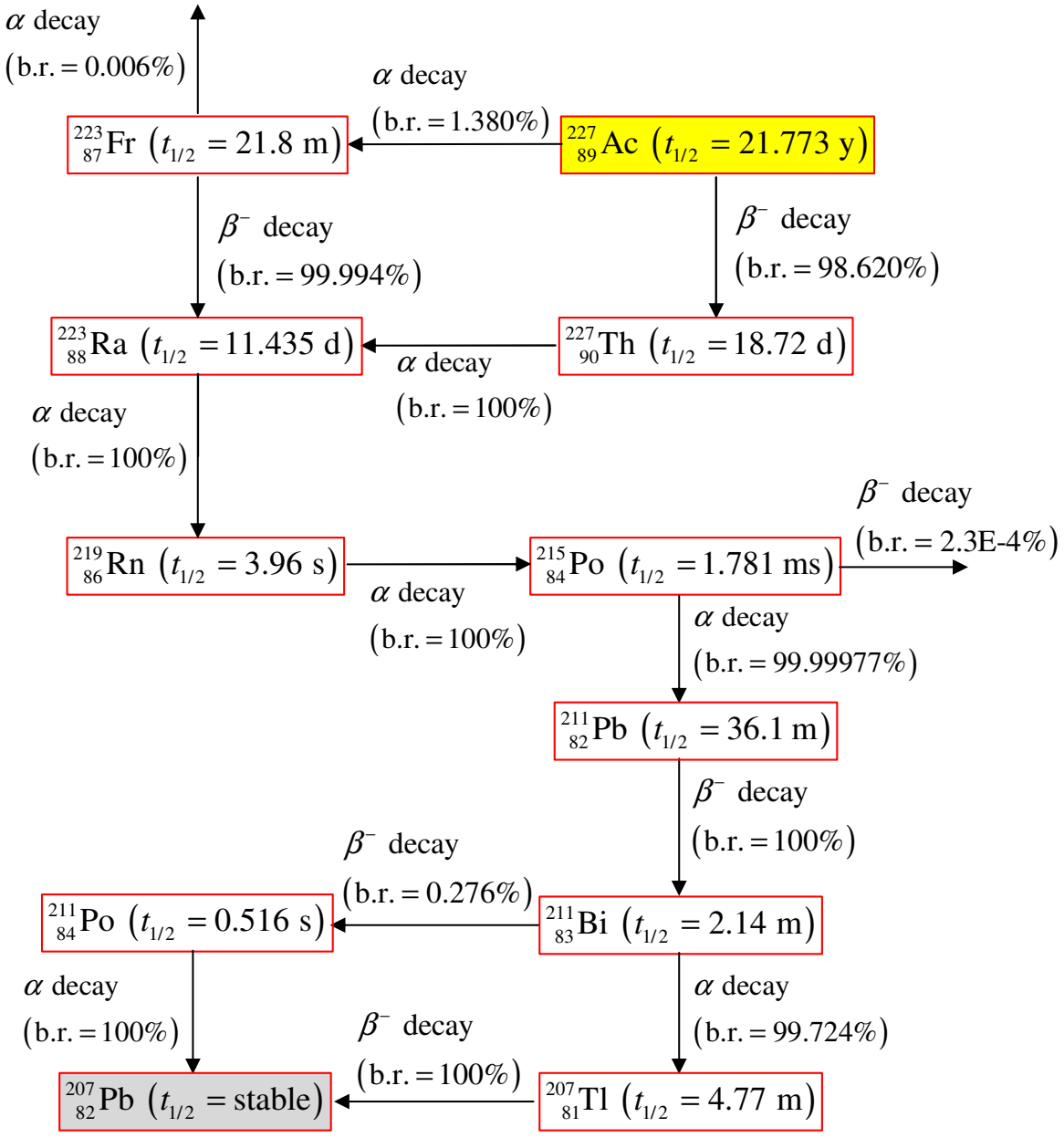

Figure 5.12: Decay chain of ^{227}Ac. For each isotope, the half-life ($t_{1/2}$) and the different modes of decay are given. The branching ratio (b.r.) for each mode is also provided.

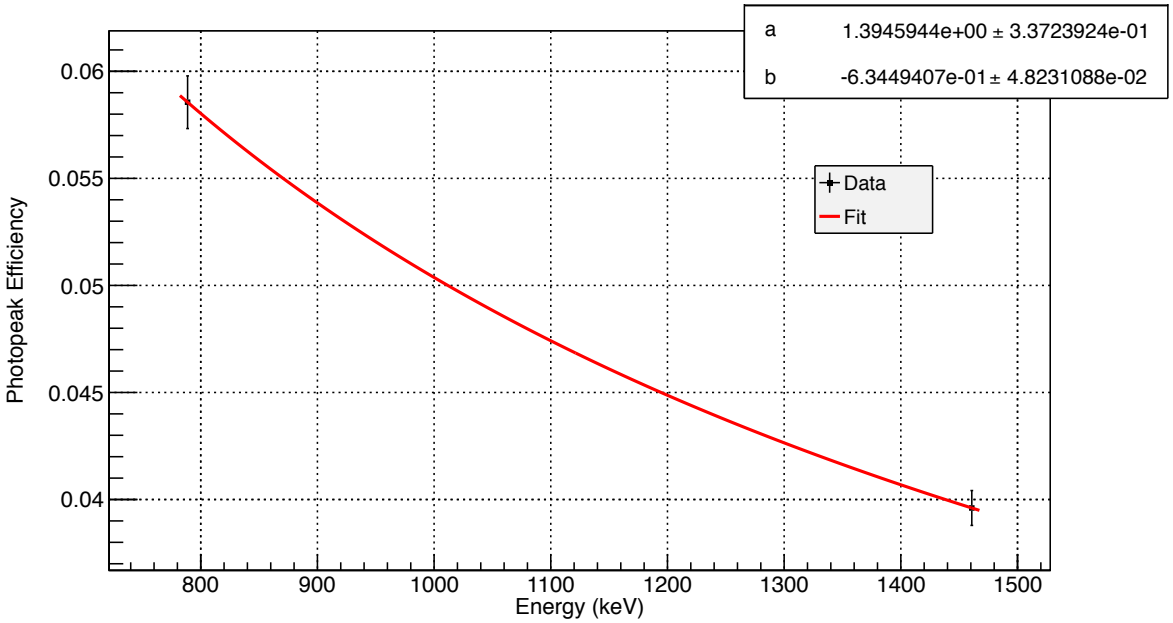

(a) ES1.

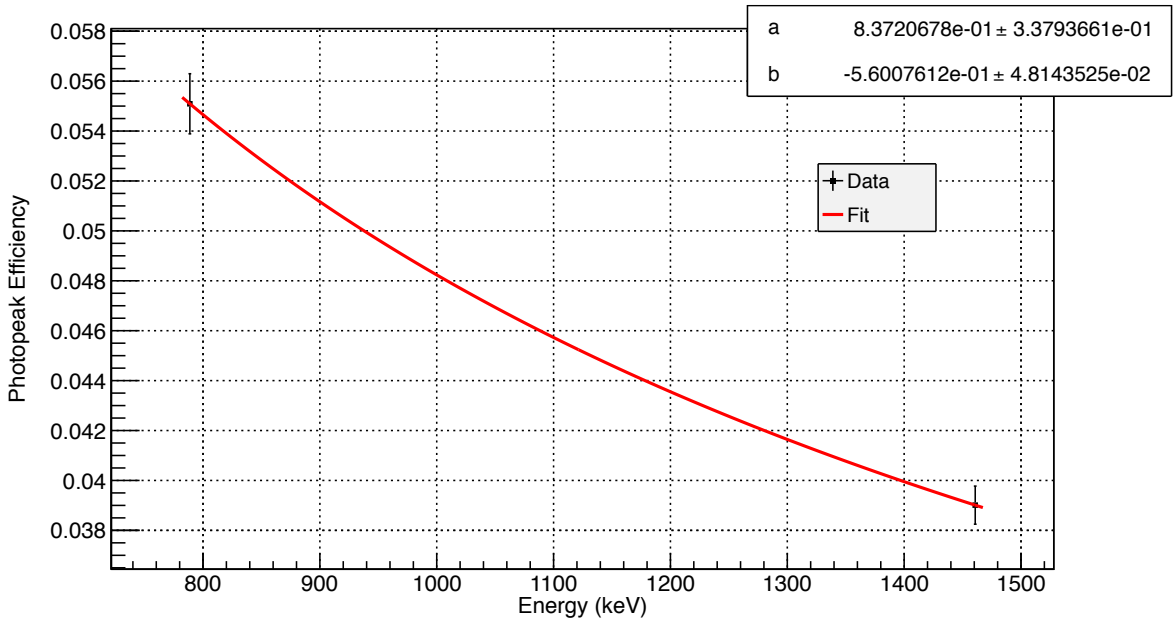

(b) ES2.

Figure 5.13: Curve-fit results for the extended sources ES1 and ES2. Equation 5.47 has been fit to the photopeak efficiencies at 788.74 keV and 1460.82 keV.

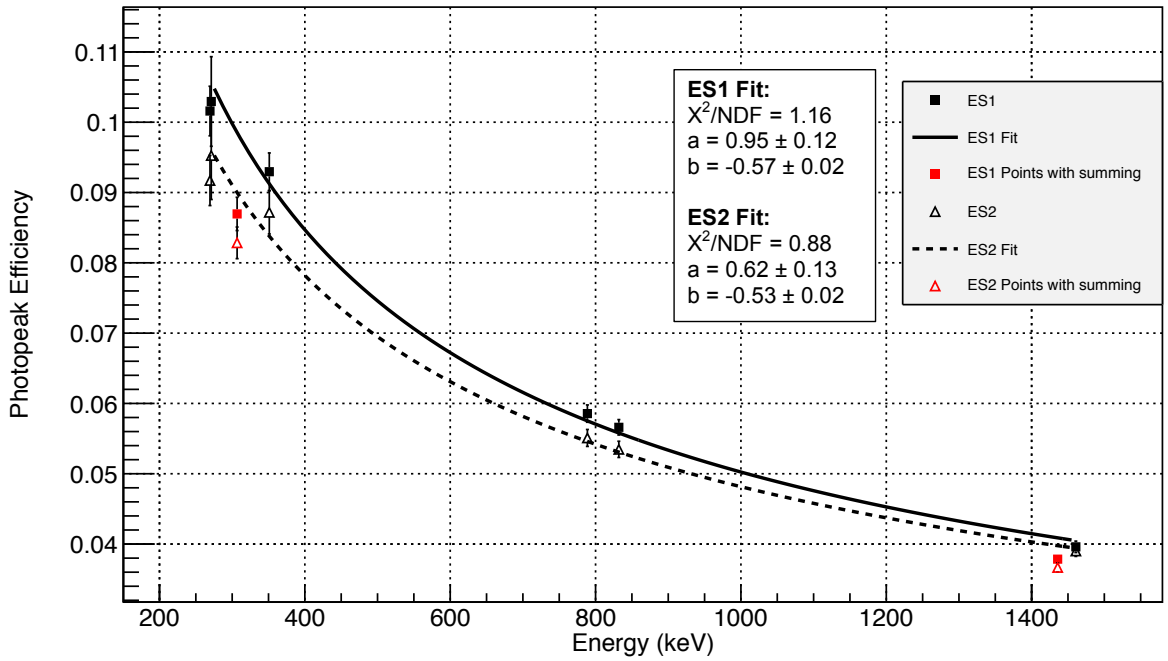

Figure 5.14: The measured photopeak efficiencies obtained for ES1 (black squares) and ES2 (black triangles) are plotted and fit with Equation 5.47. The solid black line and dotted black line are the results of the fit for ES1 and ES2, respectively. The values obtained for the fitting constants a and b are also provided. The red squares and triangles are the photopeak efficiencies obtained for gamma rays (307 keV and 1436 keV) that were affected by true coincidence summing.

was also used in ES2, ^{227}Ac and its daughter isotopes were also present. The photopeak efficiencies for the 269-keV, 271-keV, 351-keV, and 832-keV gammas were obtained using the method described for ES1. The efficiencies for ES2 are plotted in Figure 5.14 and fit with Equation 5.47. From the figure, one can see that the differences in powder height and density do not substantially change the photopeak efficiencies, leading to the conclusion that either curve can be used to obtain reasonable efficiencies for the TeO_2 powder, although the results for ES2 should be a better match. The figure does show evidence of gamma self-attenuation, which refers to the attenuation of source gammas by the source material itself. Since ES2 has a larger density than ES1, self-attenuation in ES2 should be more severe than in ES1, resulting in lower photopeak efficiencies for ES2. This is clearly seen in the figure. Additionally, low energy gammas are self-attenuated more than high energy gammas. Therefore, one expects to see larger differences between the ES1 and ES2 photopeak efficiencies at low energies and smaller differences at high energies. This effect is also seen in the figure.

Unfortunately, the photopeak efficiency curves for ES1 and ES2 are not sufficient for the cross-section analysis discussed in this chapter. The gamma energies used to obtain the cross sections go down to 105 keV, which is not in the energy range covered by ES1 and ES2. Furthermore, several of the gammas are emitted in coincidence with other gammas, which will result in efficiencies that are either higher or lower than those predicted by the ES1 and ES2 curves. The efficiencies are affected in this way because of true coincidence summing.

What is true coincidence summing? When a nucleus decays and generates multiple

gammas, the typical emission time of each gamma is much shorter than the resolving time of the detector (e.g., HPGe). Therefore, from the point of view of the detector, all the gammas are emitted at the same time. The photopeak efficiencies of the gammas are strongly dependent on the size of the source and the source-detector distance. For example, if we have a point source that is tens of centimeters away from the face of an HPGe detector, the solid angle subtended by the detector is small, which means the probability that more than one gamma will hit the detector simultaneously is small. The photopeak efficiency curve obtained at this distance will be similar to the ones shown in Figure 5.14: the efficiency will increase smoothly with decreasing energy, reach a maximum at some energy (not shown in Figure 5.14), and start decreasing smoothly with decreasing energy. This decrease in efficiency at lower energies is due to the gammas being absorbed in materials between the source and the active region of the detector crystal (e.g., detector endcap, crystal dead layer). As the source-detector distance decreases, the solid angle subtended by the detector increases, which in turn increases the probability that more than one gamma ray will hit the detector simultaneously. When two (or more) gammas hit the detector at the same time, each will deposit some or all of its energy in the detector. The total energy deposition, E_{tot}, will be

$$\begin{aligned} E_{tot} &= f_1 E_{\gamma 1} + f_2 E_{\gamma 2}, \\ 0 \leq f_1 \leq 1 &\text{ and } 0 \leq f_2 \leq 1, \end{aligned} \tag{5.50}$$

where $E_{\gamma 1}$ and $E_{\gamma 2}$ are the energies of the two gammas (γ_1 and γ_2, respectively) when they are emitted from the source. This summing of energies is known as *true coincidence gamma summing*.

To understand why coincidence summing will cause some gammas from the TeO_2 powder to have higher or lower efficiencies than those predicted by ES1 and ES2, consider the case where γ_1 deposits all of its energy in the detector (i.e., $f_1 = 1$) and γ_2 deposits some or all of its energy in the detector (i.e., $0 < f_2 \leq 1$). In this scenario, a count that would have gone to the $E_{\gamma 1}$ peak if there were no coincidence summing now goes to some other energy in the gamma spectrum. Thus, compared to the no-summing case, the number of counts in the $E_{\gamma 1}$ peak will be lower, resulting in a lower corresponding photopeak efficiency. This is known as *summing out*. There is also a phenomenon called *summing in* where the sum of two (or more) gammas is equivalent to the energy of another gamma, $E_{\gamma 3}$. In this case, there will be more counts in the peak at $E_{\gamma 3}$ than there would be if no coincidence summing occurred, and a higher photopeak efficiency at $E_{\gamma 3}$ results. For both ES1 and ES2, the 202-keV, 307-keV, and 1436-keV gammas all suffered from the effects of summing out. The measured photopeak efficiencies at 307 keV and 1436 keV are shown in red in Figure 5.14; they were obtained with Equation 5.46. As one can see, they are lower than the efficiencies predicted by ES1 and ES2.

Many of the radioisotopes observed in the irradiated TeO_2 powder have complicated decay schemes in which multiple gammas are emitted in coincidence during a decay; the decay scheme for ^{126}Sb is shown in Figure 5.15 as an example. The photopeak efficiencies for gammas from these radioisotopes will be affected by true coincidence summing. In principle, it is possible to determine these efficiencies using a combination of experimental measurements and mathematical calculations. Consider, for example, a simple case in which a point source with the decay scheme in Figure 5.16 is centered on the face of a gamma detector. The source emits three gamma rays, γ_1, γ_2, and γ_3, with energies

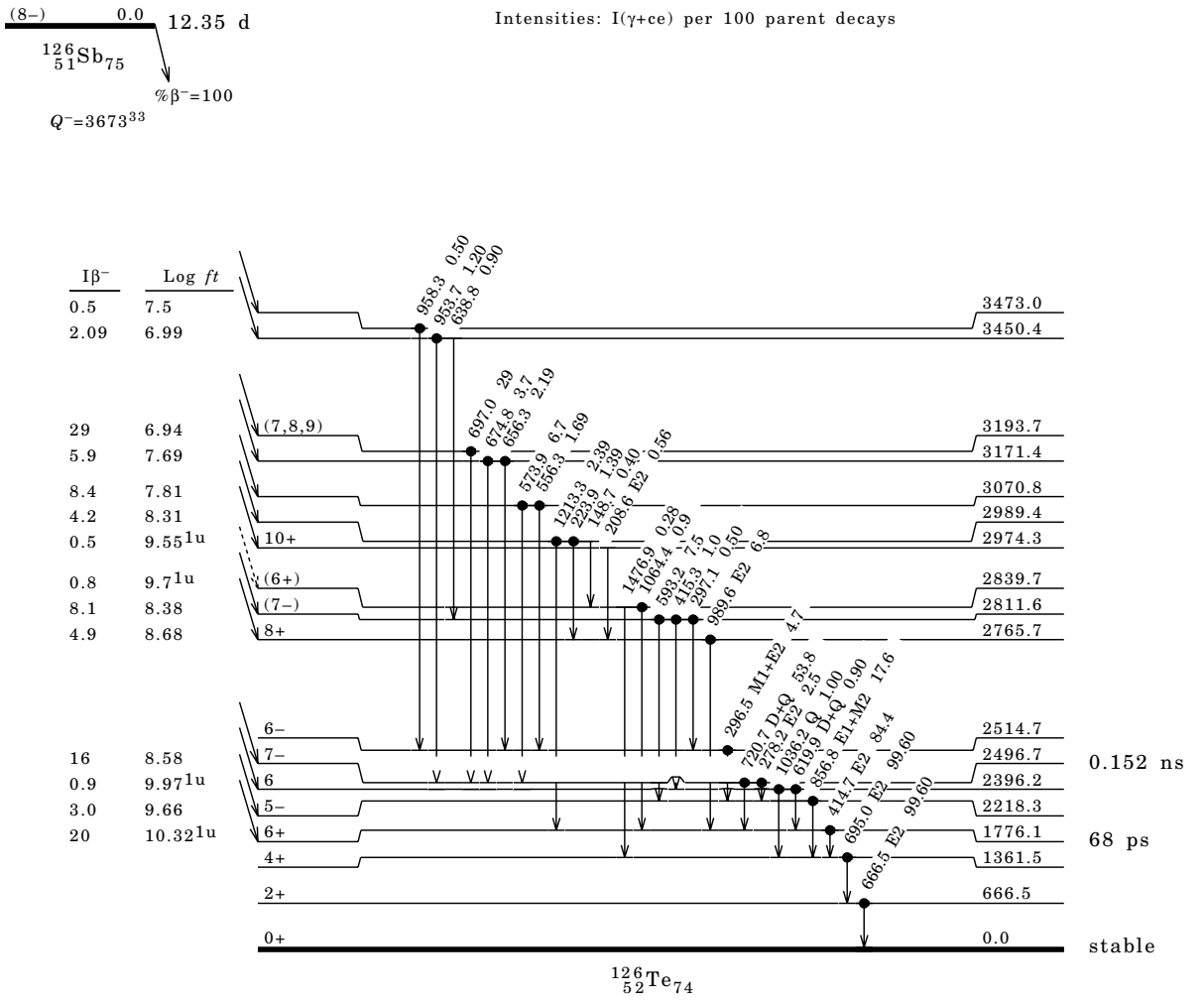

Figure 5.15: Decay scheme for ^{126}Sb. The figure was obtained from Ref. [102]. The 720.7-keV gamma ray was used to determine the cross section for ^{126}Sb. As can be seen, this gamma is emitted in coincidence with several other gammas.

$E_{\gamma 1}$, $E_{\gamma 2}$, and $E_{\gamma 3}$, respectively. B_1, B_2, and B_3 are the branching ratios of the gammas divided by 100%, and the internal conversion coefficient [80, 94] for each gamma is zero. Also assume that angular correlation [80] between γ_1 and γ_2 can be ignored. The photopeak efficiency for each gamma could be determined by first experimentally obtaining the photopeak efficiency curve for the no-summing case. This is done by identifying calibration point sources that emit gammas with no (or negligible) summing and measuring them at the center of the detector face. The gammas should ideally cover an energy range that includes $E_{\gamma 1}$, $E_{\gamma 2}$, and $E_{\gamma 3}$. The photopeak efficiencies without summing for γ_1, γ_2, and γ_3 (i.e., ϵ'_1, ϵ'_2, and ϵ'_3, respectively) can now be deduced by methods such as fitting the photopeak efficiency curve with a function or interpolating between points on the curve. The next step in the analysis is to get the *total* detection efficiencies of the three gammas for the no-summing case (i.e., ϵ'_{t1}, ϵ'_{t2}, and ϵ'_{t3}). The total efficiency is the probability that a gamma ray deposits *any* amount of energy in the detector. The total efficiencies without summing can be most easily obtained by measuring *monoenergetic* calibration point sources at the center of the detector face. Once again, the calibration

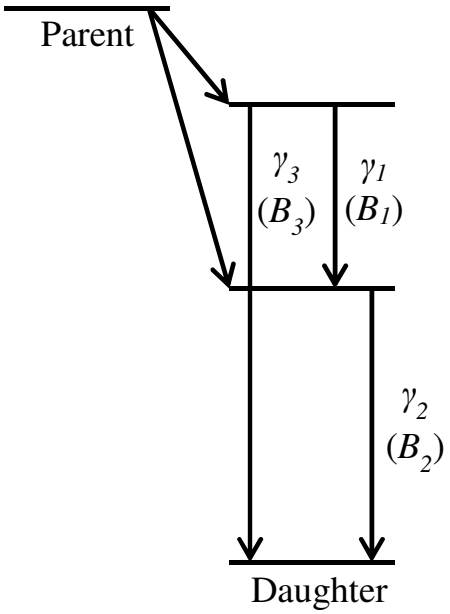

Figure 5.16: Example decay scheme used to discuss true coincidence summing. The parameters B_1, B_2, and B_3 are the branching ratios (divided by 100%) of γ_1, γ_2, and γ_3, respectively. The internal conversion coefficients [80, 94] for the three gammas are all zero. It is also assumed that angular correlation between γ_1 and γ_2 can be ignored.

sources should cover an energy range that includes $E_{\gamma 1}$, $E_{\gamma 2}$, and $E_{\gamma 3}$; and the parameters ϵ'_{t1}, ϵ'_{t2}, and ϵ'_{t3} can then be determined by fitting the total efficiency curve with a function or by interpolating between points on the curve. Taking A to be the decay rate of the source from Figure 5.16, the count rate, c_1, in the $E_{\gamma 1}$ peak would be

$$c_1 = AB_1\epsilon'_1 - AB_1\epsilon'_1\epsilon'_{t2}, \tag{5.51}$$

the count rate, c_2, in the $E_{\gamma 2}$ peak would be

$$c_2 = AB_2\epsilon'_2 - AB_1\epsilon'_{t1}\epsilon'_2, \tag{5.52}$$

and the count rate, c_3, in the $E_{\gamma 3}$ peak would be

$$c_3 = AB_3\epsilon'_3 + AB_1\epsilon'_1\epsilon'_2. \tag{5.53}$$

The photopeak efficiencies (with summing) for γ_1, γ_2, and γ_3 (i.e., ϵ_1, ϵ_2, and ϵ_3, respectively) can now be obtained:

$$\epsilon_1 = \frac{c_1}{AB_1} = \epsilon'_1(1 - \epsilon'_{t2}), \tag{5.54}$$

$$\epsilon_2 = \frac{c_2}{AB_2} = \epsilon'_2\left(1 - \frac{B_1}{B_2}\epsilon'_{t1}\right), \tag{5.55}$$

$$\epsilon_3 = \frac{c_3}{AB_3} = \epsilon'_3 + \frac{B_1}{B_3}\epsilon'_1\epsilon'_2. \tag{5.56}$$

For the irradiated TeO_2 powder, using the latter method for determining photopeak efficiencies is intractable. Many of the radioisotopes present in the powder have decay

schemes far more complex than Figure 5.16, making it very challenging to mathematically calculate photopeak efficiencies using equations akin to Equations 5.51–5.56. Furthermore, obtaining the no-summing photopeak and total efficiency curves needed for the mathematical calculations is also difficult. This is due to the challenge of creating suitable calibration sources, which (1) should each be able to reproduce the geometry and density of the TeO_2 powder during gamma counting and (2) should each be preferably monoenergetic to make obtaining the no-summing total efficiency curve easier. Requirement (1) is quite easy to achieve; however requirement (2) is problematic because there are not many radioisotopes that decay monoenergetically. Due to the myriad of complications, computer simulations were selected as the method for obtaining photopeak efficiencies for the TeO_2 powder. The GEANT4 (GEometry ANd Tracking 4) code [95, 96], version 4.9.4.p02, was chosen to run these simulations.

GEANT4 is a C++-based software package comprised of tools that can be used to accurately simulate the passage of particles through matter. Before running the code, the user must:

- construct the simulated system by defining the geometry and material of each object in the system (e.g., the detector, items surrounding the detector);
- indicate what physics processes (e.g., Compton scattering, photoelectric effect, ionization, bremsstrahlung) will be included in the simulation to describe how particles interact with materials;
- construct the radiation source by defining its geometry, its location, the particles it emits, etc.

Once the simulation is started, GEANT4 utilizes Monte Carlo methods [103] to track the source particles as they travel through the system. The user can ask GEANT4 to output information such as the energy deposition in specified parts of the system, track lengths of source particles, physics processes the source particles participate in, the secondary particles produced in each interaction, etc.

Photopeak efficiencies were determined by first constructing the gamma counting setup for the TeO_2 powder (Figure 5.7c) in GEANT4. The setup included four main components: the HPGe detector, the Marinelli beaker, the plastic insert, and the TeO_2 powder. A detailed schematic of the HPGe detector used in the gamma measurement was provided by the manufacturer, ORTEC, and is shown in Figure C.1 of Appendix C. It contains the dimensions and material of each component in the detector. All components below the HPGe crystal were excluded from the simulations. The top edge of the crystal was rounded (or bulletized) to improve charge collection. This detail was also excluded from the simulations; a sharp edge was used instead. A detailed schematic of the detector geometry used in GEANT4 is given in Figure 5.17. Each component was constructed in GEANT4 using the material listed in Figure C.1 or Table C.1. The physical dimensions used in the simulations will be discussed later in this section. The geometries and materials used to simulate the Marinelli beaker, the plastic insert, and the TeO_2 powder are illustrated in Figure 5.18. Overall, these three components have been constructed in GEANT4 using the nominal dimensions and materials given by the manufacturers. However, there are a few differences. In reality, the outer sides of the Marinelli beaker are not completely vertical, and during the gamma measurement, the Marinelli beaker had a lid; refer to Figure 5.19 for a photo of the type of Marinelli beaker used in the

gamma measurement. Also, the height of the TeO_2 powder during the measurement was not constant throughout the beaker; it varied between approximately 5.3 and 5.8 cm. The average height, 5.55 cm, was used in the simulations.

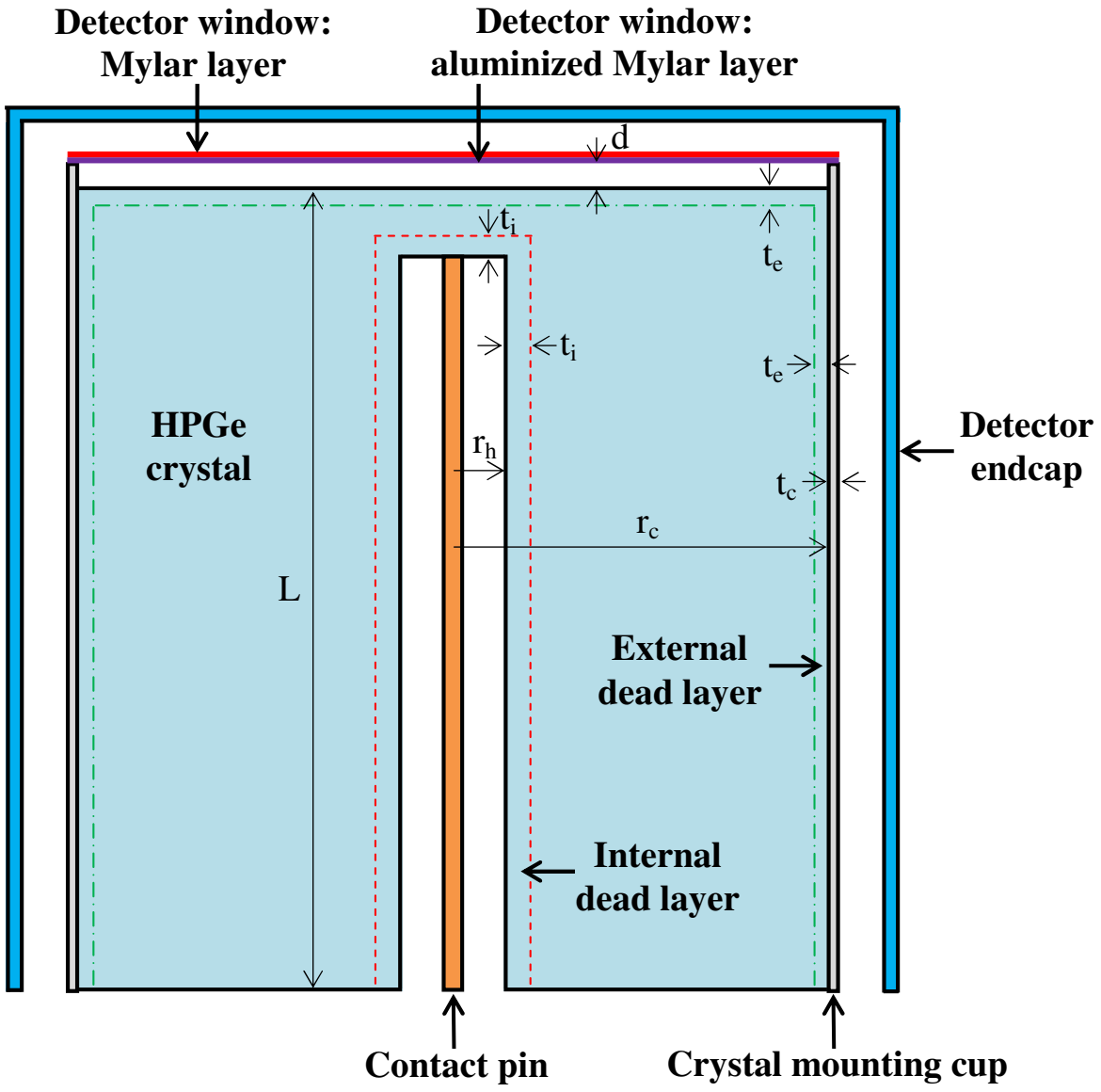

Figure 5.17: Schematic of the detector geometry used in the GEANT4 simulations. The material of each component can be found in Table C.1 or Figure C.1 of Appendix C.

A separate simulation was performed for each gamma ray of interest. As demonstrated earlier in this section, the efficiencies obtained from these simulations need to reflect the coincidence summing that occurs when the gamma is emitted from the *radioisotope of interest*. For each gamma, the decay scheme of the corresponding radioisotope was examined to determine whether or not true coincidence summing needed to be taken into account. For cases where the gamma is emitted with negligible or no coincidence summing, GEANT4 simulated monoenergetic gammas with energy E_γ. The gammas were generated one at a time; their positions were uniformly distributed throughout the volume of the TeO_2 powder and their directions were isotropic. GEANT4 tracked each

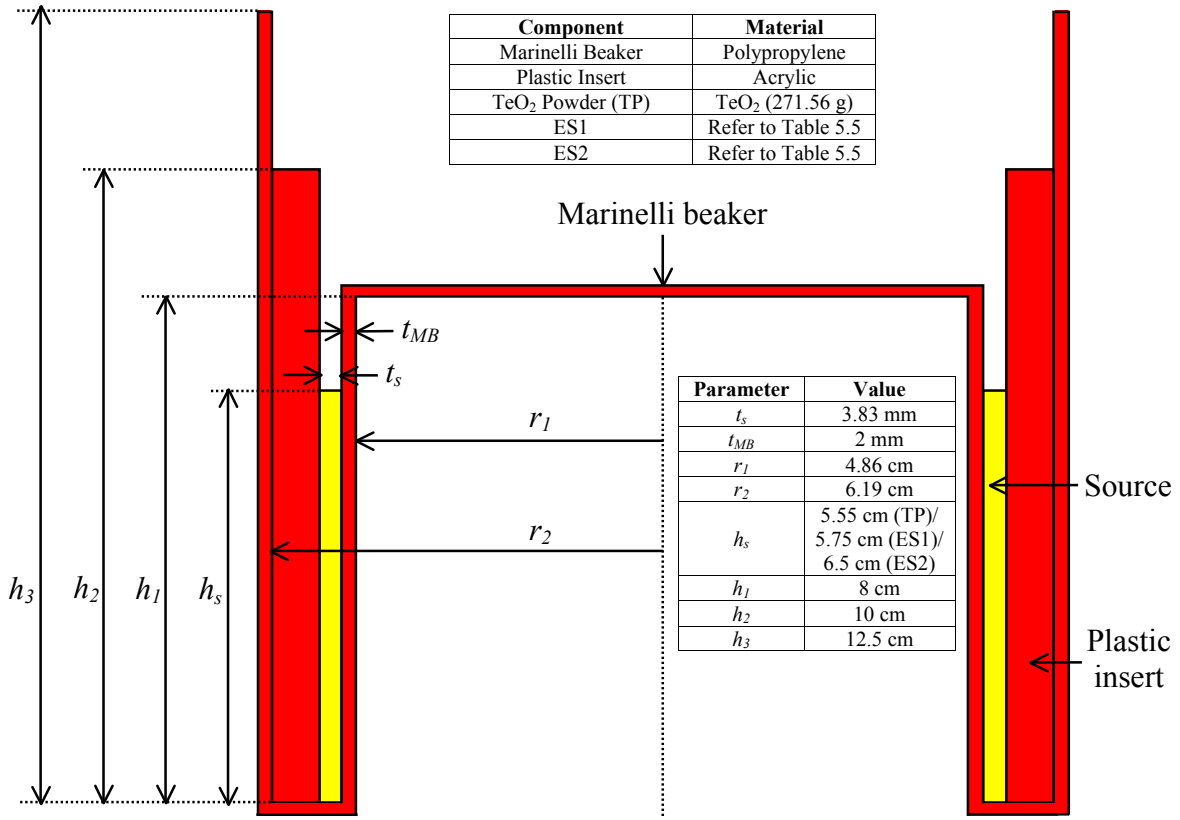

Figure 5.18: The geometries and materials used in GEANT4 to construct the Marinelli beaker, the plastic insert, the irradiated TeO_2 powder, and the two extended sources. The parameter h_s is the average height of the source in the beaker.

Figure 5.19: Photo of the type of Marinelli beaker used in the gamma measurements of the irradiated TeO_2 powder and the two extended sources. Photo was taken from Ref. [104].

gamma and determined the amount of energy deposited in the active region [88,94] of the detector. The active region is the part of the detector in which charge carriers [88,94] are produced and collected to form the detector signal. In an HPGe detector this would be the entire HPGe crystal, excluding the dead layer regions on the inner and outer surfaces of the crystal (Figure 5.17). During a simulation, a histogram of the energy deposited in the detector by each gamma was collected. For the no-summing case, the photopeak efficiency at E_γ was obtained using

$$\epsilon_\gamma = \frac{C_\gamma}{N_\gamma}, \tag{5.57}$$

where C_γ is the number of counts in the E_γ peak of the histogram and N_γ is the number of source gammas simulated. To ensure a statistical uncertainty of less than 1% for C_γ, N_γ was set to hundreds of thousands or millions, depending on the value of E_γ.

For cases where coincidence summing could not be ignored, the radioactive nucleus producing the gamma of interest was simulated in GEANT4, instead of just the gamma. GEANT4 generated a uniform distribution of the radioactive nucleus throughout the entire volume of the TeO_2 powder. The nuclei were simulated one at a time, with each nucleus created at a random position in the powder. When a nucleus decays in GEANT4, all the particles that would be produced in a real-life decay are produced and tracked in GEANT4. Gammas that are emitted in coincidence in the decay scheme are produced simultaneously in GEANT4, allowing for coincidence summing to be simulated. One issue to note is that all gammas are generated isotropically in GEANT4, which means that angular correlation [80] between gammas emitted in cascade is not taken into account. Fortunately, because the TeO_2 powder surrounds such a large region of the detector, the effects of angular correlation are largely averaged out. During a simulation, the total energy deposited in the detector's active region was recorded for each decay, and as in the no-summing case, a histogram of energy deposition was created. For each coincidence summing case, the photopeak efficiency at E_γ was obtained using Equation 5.57, where C_γ is still the number of counts in the E_γ peak of the histogram, but N_γ is now the number of gammas with energy E_γ produced by radioactive decay in GEANT4. To ensure a statistical uncertainty of less than 1% for C_γ, the number of radioactive nuclei generated in each simulation was set to hundreds of thousands to millions, depending on the branching ratio of the gamma of interest.

Before running the simulations for the TeO_2 powder, GEANT4 was benchmarked against experimental measurements of various gamma sources. These included ES1 and ES2, calibration point sources, and a uranium-ore source (described in Table 5.5). Each measurement was reproduced with GEANT4. Then, photopeak efficiencies were obtained from the simulations and compared with the measured values to determine the reliability of GEANT4's results. Gamma lines for which photopeak efficiencies were obtained are given in Table 5.6, along with their branching ratios.

The calibration point sources measured were ^{57}Co and ^{54}Mn. A calibration source is a source for which the activity A_0 on a particular reference date is known. ^{57}Co electron capture decays 100% of the time. 99.8% of the time, either a 122-keV or 136-keV gamma is emitted in coincidence with x-rays 6 - 7 keV and lower. The 122-keV gamma is also in coincidence with a 14-keV gamma. The x-rays and 14-keV gamma are too low in energy to reach the detector, so summing will not occur for the 122-keV and 136-keV gammas. ^{54}Mn also electron capture decays 100% of the time. Essentially 100% of the time it

emits an 835-keV gamma in coincidence with x-rays ∼5 keV and lower. These x-rays are too low in energy to reach the detector, so summing will also not occur for the 835-keV gamma. For the 122-keV, 136-keV, and 835-keV gammas, ϵ_γ can be determined using Equation 5.46, where $A = A_0 \exp(-\lambda t_s)$, λ is the decay constant of the calibration source isotope, and t_s is the start time of the measurement relative to the reference date.

In each ^{57}Co and ^{54}Mn measurement, the source was placed at a single location and counted until C_γ for the photopeak of interest had a statistical uncertainty of less than 1%. Each point source was measured at the five locations indicated in Figure 5.11a:

(1) at the center of the detector face;
(2) along the side of the detector, 1.9 cm below the detector face;
(3) along the side of the detector, 3.9 cm below the detector face;
(4) along the side of the detector, 5.9 cm below the detector face;
(5) along the side of the detector, 7.9 cm below the detector face.

For measurements along the side of the detector, the point source was taped to a 2 mm-thick, cylindrical plastic shell (colored red in Figure 5.11a) that was then placed over the HPGe detector. This set of measurements served as a good benchmark for how well simple sources could be simulated by GEANT4. Additionally, the measurements along the side of the detector also allowed for an evaluation of how much the heights of the TeO_2 powder, ES1, and ES2 affect the photopeak efficiencies. As mentioned previously, the height of the TeO_2 powder varied between approximately 5.3 cm and 5.8 cm. The heights of ES1 and ES2 had similar variations as well. The photopeak efficiencies along the side of the detector for the 122-keV, 136-keV, and 835-keV gammas are plotted in Figure 5.20. The plot indicates that the efficiencies will not be affected substantially by these variations. Thus, using the average heights (Figure 5.18) in the GEANT4 simulations is a reasonable choice.

For the uranium-ore source measurement, the source was taped to the side of an empty Marinelli beaker identical to the one used to count the TeO_2 powder. This source consisted of 0.1176 g of natural-uranium in secular equilibrium [80] with all of its daughter isotopes. The uranium was mixed with epoxy and spread evenly inside the bottom of a ∼1 mm-thick, cylindrical plastic box. Table 5.5 gives the dimensions of the *uranium-epoxy mixture*. Counting was performed with the bottom of the plastic box touching the beaker; refer to Figure 5.11b. The measurement was stopped when the net counts in each gamma peak of interest had a statistical uncertainty of ∼1% or less. The photopeak efficiencies were obtained using Equation 5.46. There was one exception, however. The 185.72-keV-gamma line from ^{235}U and the 186.21-keV-gamma line from ^{226}Ra could not be separated in the spectrum and appeared as a single peak. This peak was used to determine the photopeak efficiency at 186 keV, which can be expressed as

$$\epsilon_\gamma = \frac{C_\gamma}{(A_{235} B_{185.72} + A_{226} B_{186.21}) t}. \tag{5.58}$$

A_{235} and A_{226} are the activities of ^{235}U and ^{226}Ra in the uranium-ore source. $B_{185.72}$ and $B_{186.21}$ are the branching ratios (divided by 100%) of the 185.72-keV and 186.21-keV gammas.

Once all gamma-source measurements had been performed and photopeak efficiencies obtained, each measurement was reproduced in GEANT4. In these simulations, the HPGe

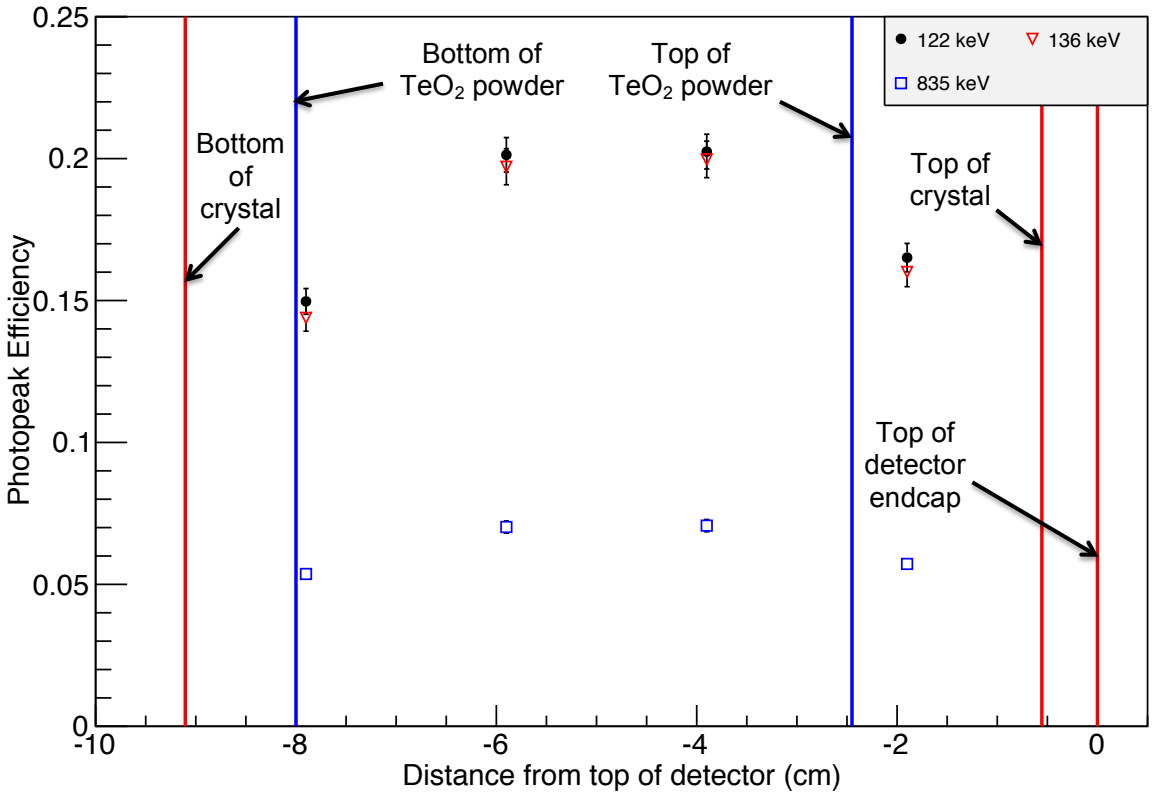

Figure 5.20: The photopeak efficiencies obtained from ^{57}Co and ^{54}Mn point source measurements along the side of the HPGe detector are shown. The vertical distance of the point source from the top of the detector during the measurement is plotted along the x-axis. The nominal locations of the top of the detector endcap, the top of the HPGe crystal, and the bottom of the HPGe crystal are indicated with solid red lines. The bottom and average location of the top of the TeO_2 powder are indicated with solid blue lines.

detector was constructed using the schematic in Figure 5.17. Each detector component was constructed in GEANT4 using the material and physical dimensions provided by the manufacturer, ORTEC (Figure C.1). For simulations of the ^{57}Co and ^{54}Mn measurements, a monoenergetic (122 keV, 136 keV, or 835 keV), isotropic gamma point-source was constructed in GEANT4 and placed at each of the five detector locations described in Figure 5.11a. For measurements along the side of the detector, the simulations also included the plastic shell the sources were taped to. During each simulation, a histogram of the energy deposited in the detector's active region was collected. The photopeak efficiency for each gamma was then obtained using Equation 5.57. Depending on the gamma energy, N_γ from Equation 5.57 was set to tens of thousands or millions to ensure a statistical uncertainty of less than 1% for C_γ. The same statistical uncertainty was achieved in simulations of all other gamma lines in Table 5.6. During each point source measurement, there was some uncertainty in the exact location of the source, on the order of a few millimeters. In addition, each source was not really geometrically a point; it was closer to a small disk with a diameter on the order of a millimeter. Figure 5.20, however, shows that these uncertainties have only a small effect on the photopeak efficiencies. It is reasonable to assume that this is also the case for the measurement at the center of

the detector face. Thus, these uncertainties were ignored when comparing the GEANT4 point source simulations with the point source measurements.

For the uranium-ore source, the plastic container and the uranium-epoxy layer were both constructed in GEANT4. In the simulation, the uranium-epoxy layer had the dimensions specified in Table 5.5. However, the material used was just natural uranium; the epoxy was not included. This simplification could be made because the epoxy was not dense enough to significantly attenuate source gammas during the measurement. Since all gammas of interest from this source had little or no summing, the photopeak efficiency of each gamma was determined by first simulating a uniform distribution of monoenergetic gammas throughout the entire volume of the uranium layer. The gammas were generated one at a time, with a random position in the uranium and an isotropic direction of motion. A histogram of energy deposition was collected during each simulation, and the photopeak efficiency was obtained using Equation 5.57.

ES1 and ES2 were constructed in GEANT4 using the materials and dimensions listed in Table 5.5. The Marinelli beaker and plastic insert from Figure 5.18 were also included in the simulations. Many of the gammas emitted by the extended sources had either no summing or negligible summing. For these cases, a uniform distribution of monoenergetic gammas were simulated throughout the volume of the powder region. Each gamma was produced individually with a random position in the powder and a random direction. For a few gammas (1436 keV, 202 keV, and 307 keV), summing could not be ignored. In each of these cases, a uniform distribution of radioactive nuclei (^{138}La for 1436 keV and ^{176}Lu for 202 keV and 307 keV) was generated throughout the entire volume of the powder region. The nuclei were created one at a time, each with a random position and random direction. During all simulations, a histogram of energy deposition was collected. Then, photopeak efficiencies were obtained with Equation 5.57. For gammas with no or ignorable summing, N_γ was the number of source gammas simulated. For gammas with summing, N_γ was the number of gammas of interest produced by radioactive decay in GEANT4. Benchmarking against the 1436-keV, 202-keV, and 307-keV lines allowed for an evaluation of GEANT4's ability to simulate true coincidence summing.

The photopeak efficiencies obtained from the GEANT4 simulations were compared with the measured values. The percent difference between the two, i.e.,

$$\Delta\epsilon_\gamma = \frac{\epsilon_{m\gamma} - \epsilon_{s\gamma}}{\epsilon_{s\gamma}} \times 100\% \tag{5.59}$$

is plotted in Figure 5.21 at the gamma energies of interest for each experimental measurement. Here, $\epsilon_{m\gamma}$ and $\epsilon_{s\gamma}$ are the measured and simulated efficiencies, respectively. From the plot, it is evident that the simulations overestimate the photopeak efficiencies of the detector. This kind of disagreement has been seen in other studies that also implemented Monte Carlo methods to model the gamma efficiencies of HPGe detectors (e.g., Refs. [105–107]). The discrepancies have been attributed to the physical characteristics of the detector being different from the manufacturer's specifications. For example, it is common for the physical length of the crystal to deviate from the nominal value by a few millimeters. Sometimes, the crystal axis may not be parallel to the housing axis, or the location of the crystal may have an uncertainty of a few millimeters. The dead layer resulting from a Li-diffused contact can also be on the order of a millimeter thicker than specifed. Such discrepancies are not unexpected, as the manufacturing process and optimization of HPGe detectors are inherently complex. These errors may seem insignificant,

but their effects are noticeable, particularly when the source is close to the detector and therefore sensitive to small changes in geometry.

In some experiments (e.g., Ref. [105]), better agreement between simulations and measurements were attained by x-raying the detector to determine the actual (versus nominal) values of the physical parameters. In the present case, x-raying the detector was not an option; therefore, adjustments were made to the detector geometry in GEANT4 until the simulations more closely matched the measurements. Figure 5.21 was used to determine how the geometry needed to be changed. First, it was evident that all values of $\Delta\epsilon_\gamma$ were negative, i.e., the measured efficiencies were smaller than the simulated efficiencies. This could have been due to a number of issues with the simulation, such as (1) the active region of the detector being too large, (2) the sources seeing too much of the active region, or (3) too many gammas from the sources reaching the detector. Item (1) could be addressed by increasing the crystal's dead layer thicknesses, or by decreasing the crystal's size in the simulation. For the HPGe detector used in the measurements, it makes sense to only change the inner dead layer thickness. The nominal value of the outer dead layer thickness is so small ($\sim$0.3 μm) that making any kind of realistic adjustment to it would have a negligible effect on the gamma efficiencies. Item (2) could be addressed by adjusting the crystal location. Finally, item (3) could be addressed by increasing the thicknesses of the attenuating materials between the sources and the detector's active region.

The four ^{57}Co measurements along the side of the detector are shown again in Figure 5.22. Here, $\Delta\epsilon_\gamma$ is on the x-axis and the vertical distance from the top of the detector endcap is on the y-axis. The distances corresponding to the ^{57}Co measurements are -1.9 cm, -3.9 cm, -5.9 cm, and -7.9 cm for point source positions (2), (3), (4), and (5) from Figure 5.11a. The nominal locations of the top of the detector endcap, the top of the HPGe crystal, and the bottom of the HPGe crystal are also indicated in Figure 5.22. From this plot, one can see that the measurement at position (2) is sensitive to the location of the top of the crystal, and the measurement at position (5) is sensitive to the location of the bottom of the crystal. All four measurements are also sensitive to the thicknesses of any attenuating materials between the sources and the active region. For each gamma energy, the effects of attenuation should be approximately independent of the location along the side of the detector. Finally, the measurements are not affected by the crystal's inner dead layer thickness because the ^{57}Co gammas are too low in energy to penetrate very far in the crystal. Combining these observations, one can conclude from Figure 5.22 that the top of the crystal is too close to the detector endcap and the bottom of the crystal needs to be higher up along the y-axis. Increasing the crystal-detector-window distance (Figure 5.17) and decreasing the length of the crystal should help resolve both of these issues. Figure 5.21 also shows evidence of a component between the sources and detector being too thin. This is most apparent from the uranium-ore data, where $\Delta\epsilon_\gamma$ is extremely negative at the lowest gamma energy, 46.5 keV, and less negative at higher gamma energies. Increasing the thickness of one or more components between the sources and detector will help fix this issue because low-energy gammas are more strongly attenuated than high-energy gammas.

Table 5.7 lists all the parameters that were changed. Column two gives the nominal values of the parameters provided by the manufacturer. Column three shows the final values obtained after adjusting the detector geometry and gaining satisfactory agreement between the simulations and measurements. Note that the thickness increase of the alu-

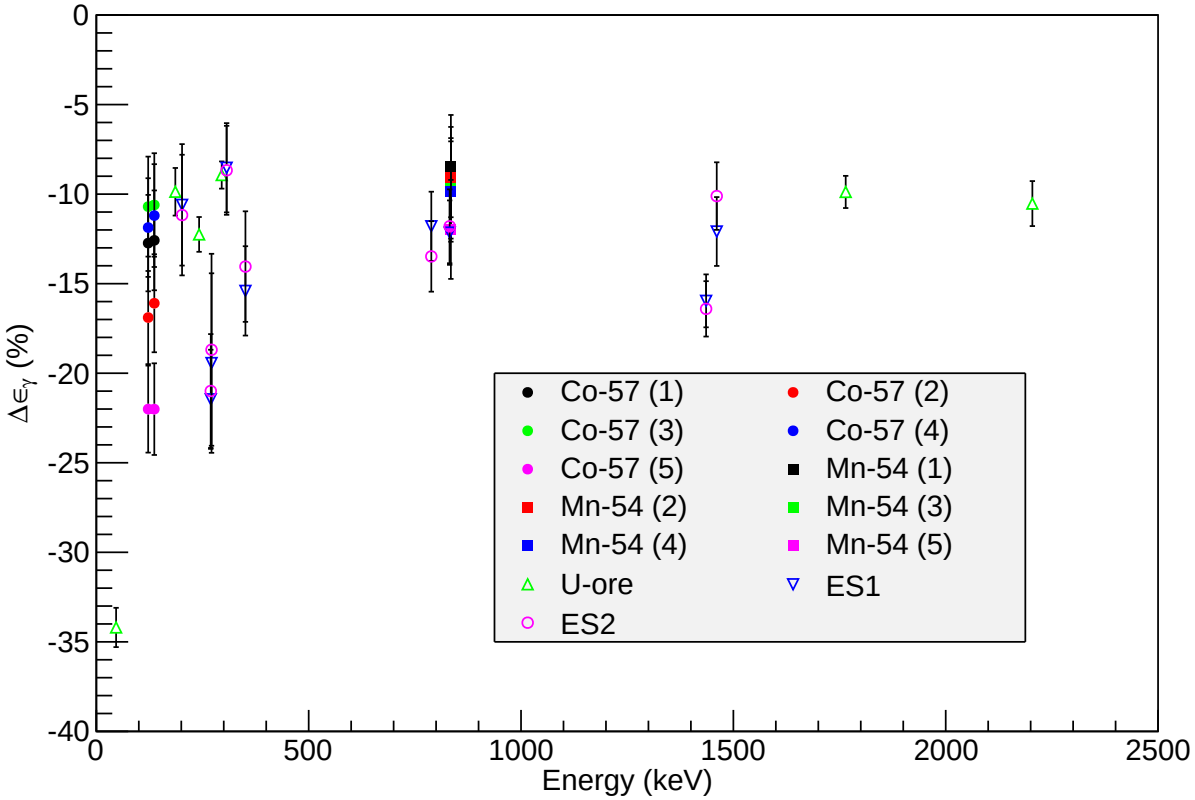

Figure 5.21: Photopeak efficiency results for GEANT4 simulations performed with the detector geometry given by the manufacturer. $\Delta\epsilon_\gamma$ is plotted versus gamma energy for each measurement described in Figure 5.11. The numbers in parentheses correspond to the point source positions in Figure 5.11a.

minum detector mounting cup may be unrealistically large. This increase was necessary to address the gamma attenuation issue just discussed. The only other parameter that could have been changed was the thickness of the detector endcap; however, this was not done because the thickness increase required would have been even more unrealistic. It is also possible that there is another attenuating material inside the detector that the manufacturer did not mention. Regardless, the 2.25 mm increase in the thickness of the mounting cup helps achieve good agreement between the simulations and measurements.

A plot of $\Delta\epsilon_\gamma$ versus gamma energy is provided in Figure 5.23 for simulations using the final set of detector parameters from Table 5.7. To estimate the uncertainty in the simulated photopeak efficiencies, the standard deviation [97], σ, was calculated for the points in the figure:

$$\sigma = \sqrt{\frac{1}{N-2}\sum_{i=1}^{N}(\Delta\epsilon_{\gamma i})^2}. \tag{5.60}$$

Here, $\Delta\epsilon_{\gamma i}$ is the value of $\Delta\epsilon_\gamma$ obtained for data point i, N is the total number of data points, and 0 is taken to be the true value [97] of each $\Delta\epsilon_{\gamma i}$. σ was determined to be 4.3%, which was then rounded up to 5%. The value 5% was taken to be the uncertainty in the simulated photopeak efficiencies, i.e., $\epsilon_{s\gamma} = \epsilon_{s\gamma} \pm \left(\frac{5}{100}\right)\epsilon_{s\gamma}$.

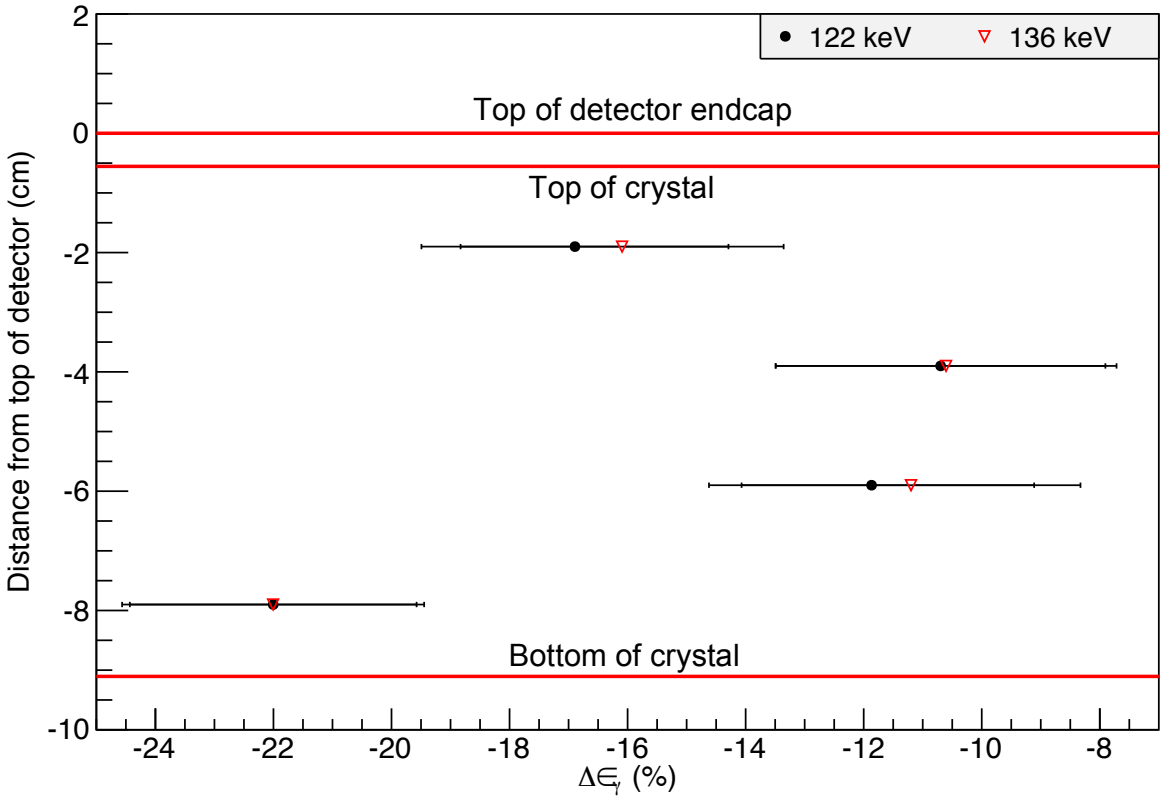

Figure 5.22: ^{57}Co data from Figure 5.21. The $\Delta\epsilon_\gamma$ values corresponding to positions (2), (3), (4), and (5) in Figure 5.11 are plotted along the x-axis. The vertical distance of each position from the top of the detector endcap is plotted along the y-axis. The numbers in parentheses indicate which position each pair of points corresponds to. The nominal locations of the top of the detector endcap, the top of the HPGe crystal, and the bottom of the HPGe crystal are indicated with solid red lines.

Table 5.7: Detector parameters adjusted in GEANT4 simulations. Parameters are labeled in Figure 5.17.

Parameter	Nominal Value from Manufacturer	Value Used in Final Detector Simulations
Crystal length (L)	85.5 mm	80.5 mm
Crystal-detector-window distance (d)	0 mm	2 mm
Al detector mounting cup thickness (t_c)	0.5 mm	2.75 mm
Internal dead layer thickness (t_i)	1 mm	2 mm

After benchmarking was complete, the irradiated TeO_2 powder simulations described earlier in this section were performed. These simulations used the final set of detector parameters from Table 5.7. The resulting photopeak efficiencies were inserted into Equation 5.36 (or the other cross-section equations used) to get the flux-averaged cross sections listed in Table 5.3. An uncertainty of 5% was also assumed for the photopeak efficiencies.

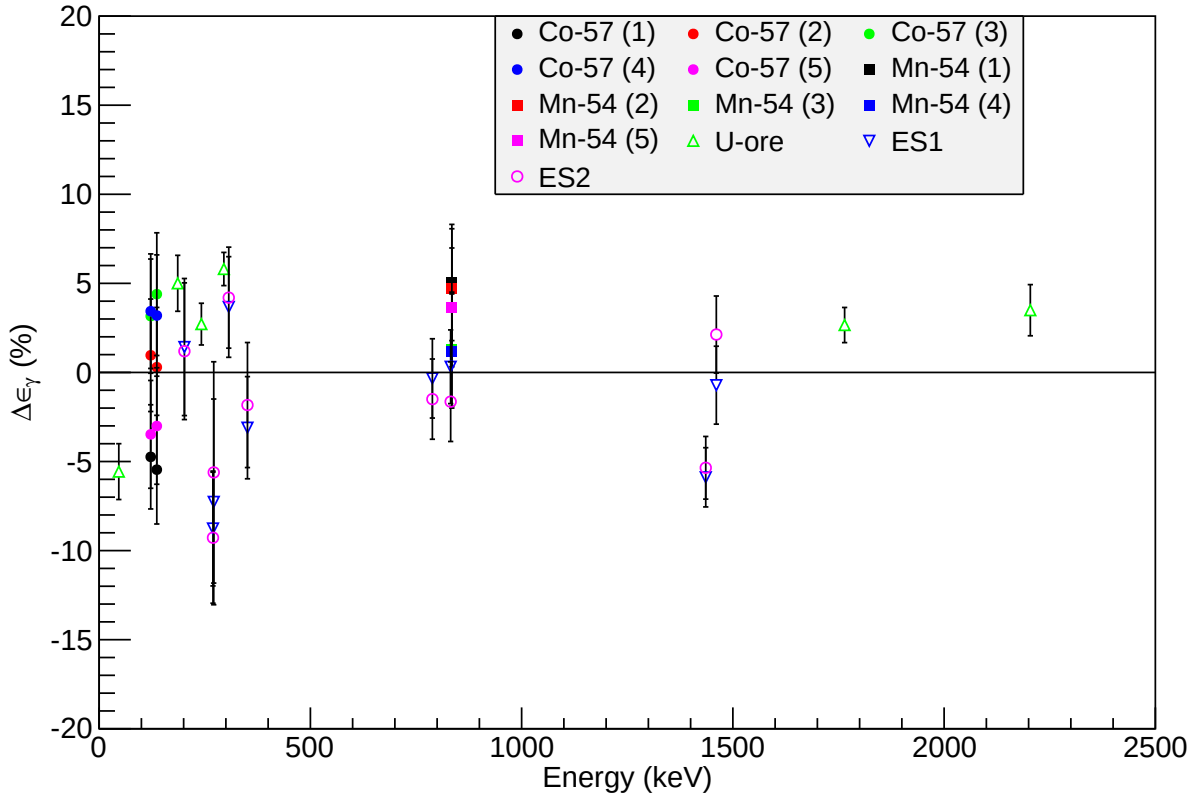

Figure 5.23: Photopeak efficiency results for GEANT4 simulations performed with the final set of detector parameters. $\Delta\epsilon_\gamma$ is plotted versus gamma energy for each measurement described in Figure 5.11. The numbers in parentheses correspond to the point source positions in Figure 5.11a.

Chapter 6

Estimation of the background in CUORE from cosmogenic activation of TeO_2

All CUORE crystals were manufactured at SICCAS (the Shanghai Institute of Ceramics, Chinese Academy of Sciences) in Shanghai, China, transported by cargo ship to Genova, Italy, then delivered by ground transportation to the Gran Sasso National Laboratory (LNGS), where they were stored underground. During their time above ground at sea-level, the crystals were exposed to cosmic-ray neutrons that induced the production of radioisotopes in the crystals. Analysis of the radioisotopes produced in the TeO_2 powder during the LANSCE experiment (Chapter 5) indicates that only ^{110m}Ag has the potential to be an important source of background in CUORE. Of main interest to CUORE are the contamination level (in Bq/kg) of ^{110m}Ag in each TeO_2 crystal and the resulting background rate (in counts/(keV·kg·y)) in the $0\nu\beta\beta$ decay region while CUORE is counting.

The contamination level of ^{110m}Ag in a single crystal is defined as

$$A'_{110m}(t) = \frac{R_{CR}\left[1 - \exp(-\lambda_{110m} t_{irrad})\right] \exp(-\lambda_{110m} t)}{m_{xtal}}, \tag{6.1}$$

where R_{CR} is the production rate of ^{110m}Ag while the crystal is at sea-level, λ_{110m} is the decay constant for ^{110m}Ag, t_{irrad} is the time the crystal spends at sea-level, t is the time the crystal spends underground, and m_{xtal} is the mass of the crystal (0.750 kg). The production rate of an isotope in a CUORE crystal at sea-level was discussed in Section 5.2. For ^{110m}Ag, R_{CR} is given by Equation 5.12:

$$R_{CR} = N\bar{T}\int_{E_{min}}^{E_{max}} \sigma(E)\varphi_{CR}(E)\mathrm{d}E,$$

where N is the number of tellurium nuclei in the crystal (2.83×10^{24} nuclei), $\sigma(E)$ is the cross section for producing ^{110m}Ag when sea-level cosmic-ray neutrons with energy E interact with tellurium, $\bar{T}$ is a parameter that describes the neutron transmission through the crystal, $\varphi_{CR}(E)$ is the differential cosmic-ray neutron flux at sea-level, and E_{min} and E_{max} are respectively the lowest and highest neutron energies the crystal is exposed to. As previously explained, $\bar{T}$ (Equation 5.11) is a difficult term to obtain because it depends on the shape of the isotope-production cross section, which is not well-known for a large

Table 6.1: Measured cross sections for the reactions Te(n,X)^{110m}Ag and Te(p,X)^{110m}Ag. The energy, E, of the incoming neutron or proton is given in column two. At 800 MeV, 1.4 GeV, and 23 GeV, the cross sections for Te(p,X)^{110m}Ag and Te(n,X)^{110m}Ag can be assumed equivalent. The flux-averaged cross section from Table 5.3 is reported for the neutron energy range 1.25 MeV - 800 MeV.

Measured Reaction	E	Cross-section (mb)
Te(n,X)^{110m}Ag	1.25 MeV - 800 MeV	0.26 ± 0.03
Te(p,X)^{110m}Ag	800 MeV	3.95 ± 0.40 [108]
Te(p,X)^{110m}Ag	1.4 GeV	1.9 ± 0.3 [11]
Te(p,X)^{110m}Ag	23 GeV	0.88 ± 0.59 [11]

range of energies below 800 MeV. For the background analysis discussed in this chapter, $\bar{T}$ is set equal to 1, which allows for an upper limit to be obtained for R_{CR}.

Cross sections for the reactions Te(p,X)^{110m}Ag have been measured at proton energies 800 MeV, 1.4 GeV, and 23 GeV [11, 108]. The values obtained are given in Table 6.1. At energies this high, the cross sections for Te(p,X)^{110m}Ag and Te(n,X)^{110m}Ag can be assumed equivalent. Using these cross sections, Equation 5.12 can now be approximated as

$$\begin{aligned} R_{CR} \simeq\ & N \int_{0\text{ MeV}}^{800\text{ MeV}} \sigma(E)\varphi_{CR}(E)\mathrm{d}E \\ & + N\sigma_{0.8} \int_{800\text{ MeV}}^{1.4\text{ GeV}} \varphi_{CR}(E)\mathrm{d}E \\ & + N\sigma_{1.4} \int_{1.4\text{ GeV}}^{23\text{ GeV}} \varphi_{CR}(E)\mathrm{d}E \\ & + N\sigma_{23} \int_{23\text{ GeV}}^{150\text{ GeV}} \varphi_{CR}(E)\mathrm{d}E. \end{aligned} \tag{6.2}$$

The parameters $\sigma_{0.8}$, $\sigma_{1.4}$, and σ_{23} are the Te(p,X)^{110m}Ag cross sections measured for 800 MeV, 1.4 GeV, and 23 GeV protons, respectively. The differential flux, $\varphi_{CR}(E)$, was taken from Ref. [81] and is discussed in detail in Section 6.1. Neutrons above 150 GeV were ignored in this analysis because their flux is negligible compared to the flux of neutrons below 150 GeV. Equation 6.2 also includes a few conservative assumptions. Between 1.4 and 150 GeV, $\sigma(E)$ should continuously decrease with increasing E. Therefore, $\sigma_{1.4}$ and σ_{23} are the highest cross sections in the energy ranges 1.4 - 23 GeV and 23 - 150 GeV, respectively, allowing for upper limits to be obtained for $N\int_{1.4\text{ GeV}}^{23\text{ GeV}} \sigma(E)\varphi_{CR}(E)\mathrm{d}E$ and $N\int_{23\text{ GeV}}^{150\text{ GeV}} \sigma(E)\varphi_{CR}(E)\mathrm{d}E$. From 800 MeV to 1.4 GeV, $\sigma(E)$ either continuously decreases, or first increases to a maximum and then decreases. If the former case is true, setting $\sigma(E)$ equal to $\sigma_{0.8}$ provides an upper limit on $N\int_{800\text{ MeV}}^{1.4\text{ GeV}} \sigma(E)\varphi_{CR}(E)\mathrm{d}E$. If the latter case is true, setting $\sigma(E)$ equal to $\sigma_{0.8}$ is still a good estimate because the difference between $\sigma_{0.8}$ and $\sigma_{1.4}$ is not very large.

Because the threshold energy for the reaction Te(n,X)^{110m}Ag is 13.9 MeV, the following is true:

$$N\int_{0\text{ MeV}}^{800\text{ MeV}}\sigma(E)\varphi_{CR}(E)\mathrm{d}E = N\int_{0\leq E_{lo}\leq 13.9\text{ MeV}}^{800\text{ MeV}}\sigma(E)\varphi_{CR}(E)\mathrm{d}E, \tag{6.3}$$

where E_{lo} is the lower limit of the integral on the right-hand side. If one defines

$$\bar{\sigma}_{CR}(E_{lo}) \equiv \frac{\int_{E_{lo}}^{800\text{ MeV}}\sigma(E)\varphi_{CR}(E)\mathrm{d}E}{\int_{E_{lo}}^{800\text{ MeV}}\varphi_{CR}(E)\mathrm{d}E}, \tag{6.4}$$

Equation 6.3 can be written as

$$N\int_{0\text{ MeV}}^{800\text{ MeV}}\sigma(E)\varphi_{CR}(E)\mathrm{d}E = N\bar{\sigma}_{CR}(E_{lo})\int_{0\leq E_{lo}\leq 13.9\text{ MeV}}^{800\text{ MeV}}\varphi_{CR}(E)\mathrm{d}E. \tag{6.5}$$

If E_{lo} is set equal to 1.25 MeV, then the parameter $\bar{\sigma}_{CR}(1.25\text{ MeV})$ can be approximated by setting it equal to $\bar{\sigma}_{30R}$, the flux-averaged cross section for $^{110\mathrm{m}}$Ag determined from the LANSCE experiment:

$$\bar{\sigma}_{CR}(1.25\text{ MeV}) \simeq \bar{\sigma}_{30R} \equiv \frac{\int_{1.25\text{ MeV}}^{800\text{ MeV}}\sigma(E)\varphi_{30R}(E)\mathrm{d}E}{\int_{1.25\text{ MeV}}^{800\text{ MeV}}\varphi_{30R}(E)\mathrm{d}E}. \tag{6.6}$$

Here, $\varphi_{30R}(E)$ is the LANSCE 30R differential neutron flux hitting the front of the irradiated target, and the value of $\bar{\sigma}_{30R}$ is given again in Table 6.1. Equation 6.6 is valid because the shape of the 30R neutron spectrum is very similar to that of the cosmic-ray neutron spectrum at sea-level, i.e., $\varphi_{30R}(E) \simeq k\varphi_{CR}(E)$, where k is a constant on the order of 10^8. Now, Equation 5.14 can be rewritten as

$$\begin{aligned} R_{CR} \;\simeq\; & N\bar{\sigma}_{30R}\int_{1.25\text{ MeV}}^{800\text{ MeV}}\varphi_{CR}(E)\mathrm{d}E \\ & + N\sigma_{0.8}\int_{800\text{ MeV}}^{1.4\text{ GeV}}\varphi_{CR}(E)\mathrm{d}E \\ & + N\sigma_{1.4}\int_{1.4\text{ GeV}}^{23\text{ GeV}}\varphi_{CR}(E)\mathrm{d}E \\ & + N\sigma_{23}\int_{23\text{ GeV}}^{150\text{ GeV}}\varphi_{CR}(E)\mathrm{d}E. \end{aligned} \tag{6.7}$$

The four integrated fluxes from Equation 6.7 were estimated using Ref. [81]; their values are given in Table 6.2. Details on how these values were obtained are provided in Section 6.1. Also given in Table 6.2 is the value of R_{CR} obtained after plugging in the integrated fluxes and cross sections; the individual contributions to R_{CR} from the four different energy ranges are shown as well. The uncertainties in the rates were obtained by propagating the errors from the cross sections and the integrated fluxes. From the table, one can see that the dominant contribution to $^{110\mathrm{m}}$Ag production is from neutrons in the 1.25 - 800 MeV region. Without the LANSCE cross-section measurement discussed in Chapter 5, a good estimate of R_{CR}, and therefore the contamination levels and background rates in the crystals, would be difficult to obtain.

To determine the contamination level of $^{110\mathrm{m}}$Ag in a CUORE crystal, the irradiation time, t_{irrad}, and the time the crystal spent underground, t, need to be known. Since

Table 6.2: Integrated neutron fluxes from Equation 6.7 are given. The values of E_{min} and E_{max} from the integral $\int_{E_{min}}^{E_{max}} \varphi_{CR}(E)\mathrm{d}E$ are provided in columns one and two, respectively. The production rate R_{CR}, obtained from Equation 6.7, is also shown, along with the individual contributions to R_{CR} from the four energy ranges listed below. The uncertainties in the rates were obtained by propagating the errors from the cross sections and integrated fluxes in Equation 6.7. The percentage of each contribution to R_{CR} is given in the last column.

E_{min}	E_{max}	Integrated Neutron Flux ($s^{-1}\cdot cm^2$)	Contribution to R_{CR} (s^{-1})	Contribution to R_{CR} (%)
1.25 MeV	800 MeV	$(3.7 \pm 1.3) \times 10^{-3}$	$(2.7 \pm 1.0) \times 10^{-6}$	78.78
800 MeV	1.4 GeV	$(5.3 \pm 1.9) \times 10^{-5}$	$(5.9 \pm 2.2) \times 10^{-7}$	17.12
1.4 GeV	23 GeV	$(2.6 \pm 1.0) \times 10^{-5}$	$(1.4 \pm 0.6) \times 10^{-7}$	4.09
23 GeV	150 GeV	$(1.6 \pm 0.6) \times 10^{-7}$	$(4.0 \pm 3.1) \times 10^{-10}$	0.01
		R_{CR} (s^{-1}):	$(3.5 \pm 1.3) \times 10^{-6}$	

for each crystal, the CUORE Collaboration keeps track of (1) the crystal birth date and (2) the date the crystal arrived at LNGS, the values of t_{irrad} and t can be determined. The crystal birth date is the date on which the crystal growth process was complete. The process starts with tellurium metal, which certainly contained all the cosmogenic radioisotopes from Table 5.3, excluding ^{7}Be. During growth, impurities are removed from the crystal [109]. These include any cosmogenically activated radioisotopes in the tellurium metal, except for metastable tellurium isotopes. Thus, considering that no $^{110\mathrm{m}}$Ag would be present in each crystal on its birth date, t_{irrad} is equal to the total time between (1) and (2) above. To determine the time each crystal spends underground, we consider that CUORE plans to start counting in early 2015. Assuming the start date is January 1, 2015, the time t_s each crystal has spent underground when CUORE begins counting can be obtained by subtracting (2) from January 1, 2015. Then assuming the counting end-date is five years later on January 1, 2020, the time t_e each crystal has spent underground when CUORE stops counting can be obtained by subtracting (2) from January 1, 2020. Now, using the value of R_{CR} obtained from Equation 6.7 and setting $t = t_{s(e)}$ in Equation 6.1, $A'_{110m}(t_{s(e)})$, the contamination level of $^{110\mathrm{m}}$Ag in each crystal at the start (end) of counting, can be obtained. The crystals were shipped in batches from Shanghai to LNGS. The arrival date and average irradiation time, $\bar{t}_{irrad}$, of each batch are given in Table 6.3. Average $^{110\mathrm{m}}$Ag contamination levels for each batch were obtained using

$$\bar{A}'_{110m}(t_{s(e)}) = \frac{\sum_{i=1}^{N} A'_{110m,i}(t_{s(e)})}{N}, \tag{6.8}$$

where $A'_{110m,i}(t_{s(e)})$ is the contamination level in the ith crystal of the batch at the start (end) of counting and N is the total number of crystals in the batch. $\bar{A}'_{110m}(t_s)$ and $\bar{A}'_{110m}(t_e)$ are also given in Table 6.3, along with the $^{110\mathrm{m}}$Ag contamination levels averaged

over *all* CUORE crystals. Finally, the table gives the number of crystals in each batch, as well as the total number shipped to LNGS. While a total of 1032 CUORE crystals were shipped, only 988 will be used in the experiment.

^{110m}Ag isomerically transitions to ^{110}Ag 1.33% of the time (Figure 6.1). Because the half-life of ^{110}Ag is 24.56 s, which is much shorter than that of ^{110m}Ag (250 d), the two isotopes will be in secular equilibrium within minutes of being stored underground. ^{110}Ag is of interest because it can also contribute background events to the $0\nu\beta\beta$ decay region via beta-minus decay, which has a Q-value of 2893 keV. The contamination level of ^{110}Ag in each crystal, $A'_{110}(t)$, can be obtained using

$$A'_{110}(t) = A'_{110m}(t)\left(\frac{B_{IT}}{100}\right), \tag{6.9}$$

where B_{IT} is the 1.33% branching ratio for isomerically transitioning from ^{110m}Ag to ^{110}Ag. The average ^{110}Ag contamination levels in each batch of crystals at the start ($\bar{A}'_{110}(t_s)$) and end ($\bar{A}'_{110}(t_e)$) of CUORE are listed in Table 6.4. The contamination levels averaged over *all* CUORE crystals are provided in the last row of the table.

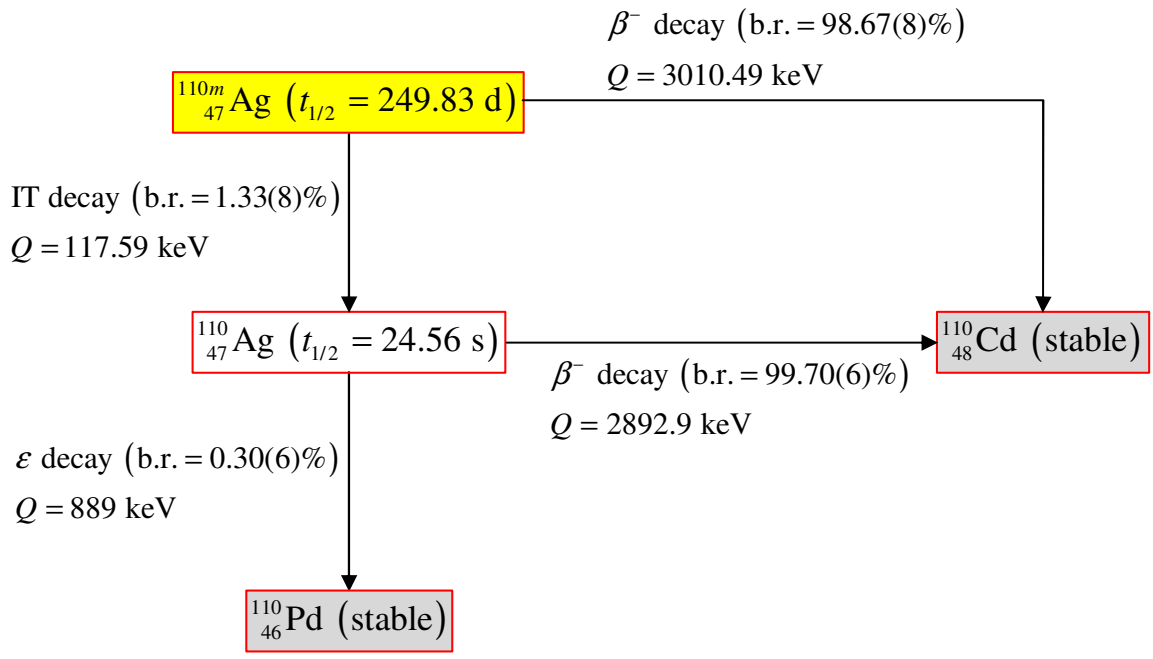

Figure 6.1: Decay chain of ^{110m}Ag. For each isotope, the half-life ($t_{1/2}$) and the different modes of decay are given. β^-, IT, and ε stand for beta-minus, isomeric transition, and electron capture, respectively. The branching ratio (b.r.) and Q-value (Q) for each mode are also provided. The number in parentheses at the end of each branching ratio is the uncertainty in the last digit.

The background rate $R'_{0\nu\beta\beta}(t)$ in the $0\nu\beta\beta$ decay region from ^{110m}Ag contamination in the CUORE crystals can now be obtained from $A'_{110m}(t)$ and $A'_{110}(t)$:

$$R'_{0\nu\beta\beta}(t) = \frac{\left[A'_{110m}(t)\epsilon^{0\nu\beta\beta}_{110m} + A'_{110}(t)\epsilon^{0\nu\beta\beta}_{110}\right]}{\Delta E_{0\nu\beta\beta}}, \tag{6.10}$$

where $R'_{0\nu\beta\beta}(t)$ is in units of counts/(keV·kg·y), $\epsilon^{0\nu\beta\beta}_{110m}$ is the probability that a ^{110m}Ag decay will result in a count in the $0\nu\beta\beta$ decay region, $\epsilon^{0\nu\beta\beta}_{110}$ is the probability that a ^{110}Ag decay will result in a count in the $0\nu\beta\beta$ decay region, and $\Delta E_{0\nu\beta\beta}$ is the width of the $0\nu\beta\beta$ decay region in units of keV. In CUORE, the $0\nu\beta\beta$ decay region ranges from 2497 keV to 2558 keV.

The parameters $\epsilon^{0\nu\beta\beta}_{110m}$ and $\epsilon^{0\nu\beta\beta}_{110}$ were obtained using GEANT4. Details and results of the GEANT4 simulations are discussed in Section 6.2. Values used to calculate the background rates in each crystal at the start and end of CUORE are $\epsilon^{0\nu\beta\beta}_{110m} = 0.0021 \pm 0.0002$ and $\epsilon^{0\nu\beta\beta}_{110} = 0.0039 \pm 0.0004$. Average background rates for each batch of crystals were determined using

$$\bar{R}'_{0\nu\beta\beta}(t_{s(e)}) = \frac{\sum_{i=1}^{N} R'_{0\nu\beta\beta,i}(t_{s(e)})}{N}, \tag{6.11}$$

where $R'_{0\nu\beta\beta,i}(t_s)$ is the background rate in the ith crystal of the batch at the start of CUORE and $R'_{0\nu\beta\beta,i}(t_e)$ is the background rate in the ith crystal of the batch at the end of CUORE. $R'_{0\nu\beta\beta}(t_s)$ and $R'_{0\nu\beta\beta}(t_e)$ are given in Table 6.5, along with the background rates averaged over *all* CUORE crystals. The rates averaged over all crystals are orders of magnitude lower than CUORE's goal background of 0.01 counts/(keV·kg·y), which means ^{110m}Ag (and ^{110}Ag) will not be an issue for CUORE.

For a more pessimistic estimate of the ^{110m}Ag background rate, one could assume that no ^{110m}Ag was removed from the TeO_2 crystals during crystal growth and that the activity of ^{110m}Ag in each crystal had reached secular equilibrium. The resulting background rates ($\sim 3 \times 10^{-4}$ counts/(keV·kg·y) and $\sim 2 \times 10^{-6}$ counts/(keV·kg·y) at the start and end of CUORE) are approximately four times higher than the rates given in the last row of Table 6.5, but they are still orders of magnitude lower than CUORE's goal background. In addition, the crystal growth process has been shown to remove impurities very effectively; the uranium and thorium content was decreased by three orders of magnitude [109]. Thus, the assumption that no ^{110m}Ag is removed is indeed quite pessimistic.

6.1 The cosmic-ray neutron flux at sea-level

Ref. [81] has shown that the cosmic-ray differential neutron flux at ground-level can be expressed as

$$\varphi_{CR}(E) = \varphi_0(E) \cdot F_{\text{alt}}(d) \cdot F_{\text{BSYD}}(R_c, d, I), \tag{6.12}$$

where $\varphi_0(E)$ is the differential cosmic-ray neutron flux at a reference location (chosen to be New York City at sea-level and mid-value solar modulation), d is the atmospheric depth in [g/cm^2], R_c is the vertical geomagnetic cut-off rigidity at the top of the atmosphere, I is a measure of the solar modulation, $F_{\text{alt}}(d)$ is a function that describes the dependence on altitude (i.e., atmospheric depth), and $F_{\text{BSYD}}(R_c, d, I)$ is a function that describes the dependence on geomagnetic location (and therefore on latitude and longitude), altitude, and solar modulation. Solar modulation refers to the affect the sun's 11-year solar activity cycle (Figure 6.2) has on the galactic (i.e., primary) cosmic-ray flux entering the Earth

Table 6.3: ^{110m}Ag contamination levels in CUORE crystals. The identification code and LNGS-arrival date of each batch of crystals are given in columns one and two. The number of crystals (N) is given in column three. The average irradiation time ($\bar{t}_{irrad}$) and average contamination levels at the start ($\bar{A}'_{110m}(t_s)$) and end ($\bar{A}'_{110m}(t_e)$) of CUORE are provided in the last three columns. The values of N, $\bar{t}_{irrad}$, $\bar{A}'_{110m}(t_s)$, and $\bar{A}'_{110m}(t_e)$ for *all* CUORE crystals are provided in the last row. Uncertainties are given in parentheses.

Batch Delivery ID	Batch Arrival Date	N	$\bar{t}_{irrad}$ (d)	$\bar{A}'_{110m}(t_s)$ (Bq/kg)	$\bar{A}'_{110m}(t_e)$ (Bq/kg)
US_01-s	2/6/2009	7	88	$2.54(96) \times 10^{-9}$	$1.60(61) \times 10^{-11}$
INFN_01	5/12/2009	25	109	$3.98(151) \times 10^{-9}$	$2.51(95) \times 10^{-11}$
INFN_02	6/4/2009	36	94	$3.73(142) \times 10^{-9}$	$2.35(89) \times 10^{-11}$
INFN_03	6/22/2009	32	89	$3.74(142) \times 10^{-9}$	$2.36(89) \times 10^{-11}$
INFN_04	9/29/2009	60	63	$3.60(137) \times 10^{-9}$	$2.27(86) \times 10^{-11}$
INFN_05	10/27/2009	34	67	$4.12(156) \times 10^{-9}$	$2.60(99) \times 10^{-11}$
INFN_06	11/25/2009	33	65	$4.34(165) \times 10^{-9}$	$2.74(104) \times 10^{-11}$
INFN_07	1/14/2010	34	90	$6.68(254) \times 10^{-9}$	$4.21(160) \times 10^{-11}$
INFN_08	1/19/2010	32	70	$5.41(205) \times 10^{-9}$	$3.41(130) \times 10^{-11}$
INFN_09	2/12/2010	27	74	$6.08(231) \times 10^{-9}$	$3.84(146) \times 10^{-11}$
INFN_10	5/11/2010	32	99	$1.00(38) \times 10^{-8}$	$6.34(241) \times 10^{-11}$
INFN_11	6/12/2010	32	94	$1.05(40) \times 10^{-8}$	$6.62(251) \times 10^{-11}$
INFN_12	7/14/2010	32	79	$9.76(371) \times 10^{-9}$	$6.16(234) \times 10^{-11}$
INFN_13	8/31/2010	32	90	$1.26(48) \times 10^{-8}$	$7.96(302) \times 10^{-11}$
INFN_14	10/11/2010	28	99	$1.54(58) \times 10^{-8}$	$9.69(368) \times 10^{-11}$
INFN_15	11/12/2010	32	90	$1.54(59) \times 10^{-8}$	$9.74(370) \times 10^{-11}$
INFN_16	12/21/2010	30	85	$1.64(62) \times 10^{-8}$	$1.03(39) \times 10^{-10}$
INFN_17	1/25/2011	30	88	$1.86(71) \times 10^{-8}$	$1.17(45) \times 10^{-10}$
US_01	3/1/2011	28	98	$2.25(85) \times 10^{-8}$	$1.42(54) \times 10^{-10}$
US_02	5/6/2011	28	69	$1.98(75) \times 10^{-8}$	$1.25(47) \times 10^{-10}$
US_03	6/24/2011	32	93	$2.96(112) \times 10^{-8}$	$1.87(71) \times 10^{-10}$
US_04	7/21/2011	31	82	$2.85(108) \times 10^{-8}$	$1.80(68) \times 10^{-10}$
US_05	9/5/2011	28	88	$3.45(131) \times 10^{-8}$	$2.18(83) \times 10^{-10}$
US_06	11/21/2011	28	75	$3.71(141) \times 10^{-8}$	$2.34(89) \times 10^{-10}$
US_07	2/7/2012	27	127	$7.28(276) \times 10^{-8}$	$4.59(174) \times 10^{-10}$
US_08	2/20/2012	26	110	$6.68(254) \times 10^{-8}$	$4.21(160) \times 10^{-10}$
US_09	4/11/2012	30	128	$8.75(332) \times 10^{-8}$	$5.52(209) \times 10^{-10}$
US_10	9/3/2012	32	104	$1.10(42) \times 10^{-7}$	$6.92(263) \times 10^{-10}$
US_11	11/5/2012	33	131	$1.59(60) \times 10^{-7}$	$1.00(38) \times 10^{-9}$
US_12	11/5/2012	32	101	$1.27(48) \times 10^{-7}$	$8.03(305) \times 10^{-10}$
US_13	12/10/2012	31	102	$1.42(54) \times 10^{-8}$	$8.93(339) \times 10^{-10}$
US_14	2/15/2013	30	101	$1.69(64) \times 10^{-7}$	$1.07(40) \times 10^{-9}$
US_15	4/23/2013	24	146	$2.77(105) \times 10^{-7}$	$1.75(66) \times 10^{-9}$
US_16	11/14/2013	24	288	$8.02(305) \times 10^{-7}$	$5.06(192) \times 10^{-9}$
All Crystals	—	1032	97	$6.23(237) \times 10^{-8}$	$3.93(149) \times 10^{-10}$

Table 6.4: ^{110}Ag contamination levels in CUORE crystals. The identification code and LNGS-arrival date of each batch of crystals are given in columns one and two. The number of crystals (N) is given in column three. The average irradiation time ($\bar{t}_{irrad}$) and average contamination levels at the start ($\bar{A}'_{110}(t_s)$) and end ($\bar{A}'_{110}(t_e)$) of CUORE are provided in the last three columns. The values of N, $\bar{t}_{irrad}$, $\bar{A}'_{110}(t_s)$, and $\bar{A}'_{110}(t_e)$ for *all* CUORE crystals are provided in the last row. Uncertainties are given in parentheses.

Batch Delivery ID	Batch Arrival Date	N	$\bar{t}_{irrad}$ (d)	$\bar{A}'_{110}(t_s)$ (Bq/kg)	$\bar{A}'_{110}(t_e)$ (Bq/kg)
US_01-s	2/6/2009	7	88	$3.37(130) \times 10^{-11}$	$2.13(82) \times 10^{-13}$
INFN_01	5/12/2009	25	109	$5.29(203) \times 10^{-11}$	$3.34(128) \times 10^{-13}$
INFN_02	6/4/2009	36	94	$4.96(191) \times 10^{-11}$	$3.13(120) \times 10^{-13}$
INFN_03	6/22/2009	32	89	$4.97(191) \times 10^{-11}$	$3.13(120) \times 10^{-13}$
INFN_04	9/29/2009	60	63	$4.79(184) \times 10^{-11}$	$3.02(116) \times 10^{-13}$
INFN_05	10/27/2009	34	67	$5.48(211) \times 10^{-11}$	$3.46(133) \times 10^{-13}$
INFN_06	11/25/2009	33	65	$5.78(222) \times 10^{-11}$	$3.64(140) \times 10^{-13}$
INFN_07	1/14/2010	34	90	$8.89(342) \times 10^{-11}$	$5.60(215) \times 10^{-13}$
INFN_08	1/19/2010	32	70	$7.20(277) \times 10^{-11}$	$4.54(174) \times 10^{-13}$
INFN_09	2/12/2010	27	74	$8.09(311) \times 10^{-11}$	$5.10(196) \times 10^{-13}$
INFN_10	5/11/2010	32	99	$1.34(51) \times 10^{-10}$	$8.43(324) \times 10^{-13}$
INFN_11	6/12/2010	32	94	$1.40(54) \times 10^{-10}$	$8.80(338) \times 10^{-13}$
INFN_12	7/14/2010	32	79	$1.30(50) \times 10^{-10}$	$8.19(315) \times 10^{-13}$
INFN_13	8/31/2010	32	90	$1.68(64) \times 10^{-10}$	$1.06(41) \times 10^{-12}$
INFN_14	10/11/2010	28	99	$2.04(79) \times 10^{-10}$	$1.29(50) \times 10^{-12}$
INFN_15	11/12/2010	32	90	$2.05(79) \times 10^{-10}$	$1.30(50) \times 10^{-12}$
INFN_16	12/21/2010	30	85	$2.18(84) \times 10^{-10}$	$1.37(53) \times 10^{-12}$
INFN_17	1/25/2011	30	88	$2.47(95) \times 10^{-10}$	$1.56(60) \times 10^{-12}$
US_01	3/1/2011	28	98	$3.00(115) \times 10^{-10}$	$1.89(73) \times 10^{-12}$
US_02	5/6/2011	28	69	$2.63(101) \times 10^{-10}$	$1.66(64) \times 10^{-12}$
US_03	6/24/2011	32	93	$3.94(151) \times 10^{-10}$	$2.48(95) \times 10^{-12}$
US_04	7/21/2011	31	82	$3.80(146) \times 10^{-10}$	$2.39(92) \times 10^{-12}$
US_05	9/5/2011	28	88	$4.59(176) \times 10^{-10}$	$2.90(111) \times 10^{-12}$
US_06	11/21/2011	28	75	$4.93(189) \times 10^{-10}$	$3.11(119) \times 10^{-12}$
US_07	2/7/2012	27	127	$9.68(372) \times 10^{-10}$	$6.10(235) \times 10^{-12}$
US_08	2/20/2012	26	110	$8.88(341) \times 10^{-10}$	$5.60(215) \times 10^{-12}$
US_09	4/11/2012	30	128	$1.16(45) \times 10^{-9}$	$7.34(282) \times 10^{-12}$
US_10	9/3/2012	32	104	$1.46(56) \times 10^{-9}$	$9.20(354) \times 10^{-12}$
US_11	11/5/2012	33	131	$2.11(81) \times 10^{-9}$	$1.33(51) \times 10^{-11}$
US_12	11/5/2012	32	101	$1.69(65) \times 10^{-9}$	$1.07(41) \times 10^{-11}$
US_13	12/10/2012	31	102	$1.88(72) \times 10^{-9}$	$1.19(46) \times 10^{-11}$
US_14	2/15/2013	30	101	$2.25(86) \times 10^{-9}$	$1.42(54) \times 10^{-11}$
US_15	4/23/2013	24	146	$3.69(142) \times 10^{-9}$	$2.33(89) \times 10^{-11}$
US_16	11/14/2013	24	288	$1.07(41) \times 10^{-8}$	$6.73(259) \times 10^{-11}$
All Crystals	—	1032	97	$8.29(319) \times 10^{-10}$	$5.23(201) \times 10^{-12}$

Table 6.5: Background rates in the $0\nu\beta\beta$ decay region due to ^{110m}Ag contamination in the CUORE crystals. The identification code and LNGS-arrival date of each batch of crystals are given in columns one and two. The number of crystals (N) is given in column three. The average irradiation time ($\bar{t}_{irrad}$) and average background rates at the start ($\bar{R}'_{0\nu\beta\beta}(t_s)$) and end ($\bar{R}'_{0\nu\beta\beta}(t_e)$) of CUORE are provided in the last three columns. The values of N, $\bar{t}_{irrad}$, $\bar{R}'_{0\nu\beta\beta}(t_s)$, and $\bar{R}'_{0\nu\beta\beta}(t_e)$ for *all* CUORE crystals are provided in the last row. Uncertainties are given in parentheses.

Batch Delivery ID	Batch Arrival Date	N	$\bar{t}_{irrad}$ (d)	$\bar{R}'_{0\nu\beta\beta}(t_s)$ (cts·keV^{-1}·kg^{-1}·y^{-1})	$\bar{R}'_{0\nu\beta\beta}(t_e)$ (cts·keV^{-1}·kg^{-1}·y^{-1})
US_01-s	2/6/2009	7	88	$2.86(138) \times 10^{-6}$	$1.81(87) \times 10^{-8}$
INFN_01	5/12/2009	25	109	$4.49(216) \times 10^{-6}$	$2.83(136) \times 10^{-8}$
INFN_02	6/4/2009	36	94	$4.21(202) \times 10^{-6}$	$2.66(127) \times 10^{-8}$
INFN_03	6/22/2009	32	89	$4.22(203) \times 10^{-6}$	$2.66(128) \times 10^{-8}$
INFN_04	9/29/2009	60	63	$4.07(195) \times 10^{-6}$	$2.56(123) \times 10^{-8}$
INFN_05	10/27/2009	34	67	$4.65(223) \times 10^{-6}$	$2.93(141) \times 10^{-8}$
INFN_06	11/25/2009	33	65	$4.91(235) \times 10^{-6}$	$3.09(148) \times 10^{-8}$
INFN_07	1/14/2010	34	90	$7.55(362) \times 10^{-6}$	$4.76(228) \times 10^{-8}$
INFN_08	1/19/2010	32	70	$6.11(293) \times 10^{-6}$	$3.85(185) \times 10^{-8}$
INFN_09	2/12/2010	27	74	$6.87(330) \times 10^{-6}$	$4.33(208) \times 10^{-8}$
INFN_10	5/11/2010	32	99	$1.13(54) \times 10^{-5}$	$7.16(343) \times 10^{-8}$
INFN_11	6/12/2010	32	94	$1.19(57) \times 10^{-5}$	$7.47(359) \times 10^{-8}$
INFN_12	7/14/2010	32	79	$1.10(53) \times 10^{-5}$	$6.95(334) \times 10^{-8}$
INFN_13	8/31/2010	32	90	$1.42(68) \times 10^{-5}$	$8.98(431) \times 10^{-8}$
INFN_14	10/11/2010	28	99	$1.73(83) \times 10^{-5}$	$1.09(53) \times 10^{-7}$
INFN_15	11/12/2010	32	90	$1.74(84) \times 10^{-5}$	$1.10(53) \times 10^{-7}$
INFN_16	12/21/2010	30	85	$1.85(89) \times 10^{-5}$	$1.17(56) \times 10^{-7}$
INFN_17	1/25/2011	30	88	$2.10(101) \times 10^{-5}$	$1.32(64) \times 10^{-7}$
US_01	3/1/2011	28	98	$2.54(122) \times 10^{-5}$	$1.60(77) \times 10^{-7}$
US_02	5/6/2011	28	69	$2.23(107) \times 10^{-5}$	$1.41(68) \times 10^{-7}$
US_03	6/24/2011	32	93	$3.34(160) \times 10^{-5}$	$2.11(101) \times 10^{-7}$
US_04	7/21/2011	31	82	$3.22(155) \times 10^{-5}$	$2.03(98) \times 10^{-7}$
US_05	9/5/2011	28	88	$3.90(187) \times 10^{-5}$	$2.46(118) \times 10^{-7}$
US_06	11/21/2011	28	75	$4.19(201) \times 10^{-5}$	$2.64(127) \times 10^{-7}$
US_07	2/7/2012	27	127	$8.21(394) \times 10^{-5}$	$5.18(249) \times 10^{-7}$
US_08	2/20/2012	26	110	$7.54(362) \times 10^{-5}$	$4.76(228) \times 10^{-7}$
US_09	4/11/2012	30	128	$9.88(474) \times 10^{-5}$	$6.23(299) \times 10^{-7}$
US_10	9/3/2012	32	104	$1.24(59) \times 10^{-4}$	$7.81(375) \times 10^{-7}$
US_11	11/5/2012	33	131	$1.79(86) \times 10^{-4}$	$1.13(54) \times 10^{-7}$
US_12	11/5/2012	32	101	$1.44(69) \times 10^{-4}$	$9.07(435) \times 10^{-7}$
US_13	12/10/2012	31	102	$1.60(77) \times 10^{-4}$	$1.01(48) \times 10^{-6}$
US_14	2/15/2013	30	101	$1.91(92) \times 10^{-4}$	$1.20(58) \times 10^{-6}$
US_15	4/23/2013	24	146	$3.13(150) \times 10^{-4}$	$1.98(95) \times 10^{-6}$
US_16	11/14/2013	24	288	$9.06(435) \times 10^{-4}$	$5.71(274) \times 10^{-6}$
All Crystals	—	1032	97	$7.04(338) \times 10^{-5}$	$4.44(213) \times 10^{-7}$

[110]. The flux is inversely correlated with the solar activity; when the solar activity reaches a maximum, the flux reaches a minimum, and vice versa. The geomagnetic rigidity is a parameter that describes how strongly a particle interacts with the Earth's magnetic field. It is defined as the momentum of the particle divided by its charge, and is usually presented in units of GV [79]. Due to the Lorentz force, galactic cosmic-ray particles are deflected away from the Earth by the geomagnetic field; particles with larger rigidities are deflected more strongly than those with smaller rigidities. The vertical cut-off rigidity is the minimum rigidity required for a particle vertically incident on the Earth to penetrate the geomagnetic field and reach a specific location [79].

The function $F_{\rm alt}(d)$ is given by [81]

$$F_{\rm alt}(d) = \exp\left[\frac{(d_{\rm SL} - d)}{L_n}\right], \tag{6.13}$$

where $d_{\rm SL}$ (= 1033.7 g/cm^2) is the atmospheric depth at sea-level and L_n (= 131.3 g/cm^2) is the effective attenuation length in the atmosphere for neutrons above 10 MeV. The value of L_n was determined from a fit to the flux data collected in Ref. [81]. At sea-level, $d = d_{\rm SL}$ and $F_{\rm alt} = 1$.

To determine the value of $F_{\rm BSYD}(R_c, d_{SL}, I)$ during crystal transportation, the route taken by the cargo ship (Figure 6.3) was used. In Figure 6.3, the latitude and longitude of several locations along the shipping route are tabulated. The value of R_c at each location was obtained using the vertical cut-off rigidity calculator from the website Geomagsphere.org [111, 112]. The calculator assumes that the Earth's magnetosphere is comprised of an internal geomagnetic field, described by the International Geomagnetic Reference Field (IGRF) model [113], and an external geomagnetic field, described by the Tsyganenko96 model [114]. The vertical cut-off rigidity at a specific location is determined by solving the equation of motion for a charged particle moving in these two fields. Before running the rigidity calculation, the user must provide a location, the time of year, and the altitude at which primary cosmic rays hit the Earth's atmosphere. The location is specified by giving latitude and longitude coordinates. The altitude was chosen to be the top of the Earth's atmosphere, which is commonly taken to be 100 km [115]. For each location, the time of year was chosen to be January 1, 2011. Looking at Tables 6.3 - 6.5, one can see that this date is an approximate average of all the crystal arrival dates. Calculated values of R_c are given in Figure 6.3

Once R_c is known, the following equations from Ref. [81] can be used to obtain $F_{\rm BSYD}$ at minimum solar activity ($F_{\rm BSYD,Smin}$) and maximum solar activity ($F_{\rm BSYD,Smax}$):

$$F_{\rm BSYD,Smin}(R_c, h) = 1.098\left[1 - \exp\left(\frac{-\alpha_1}{R_c^{k_1}}\right)\right], \tag{6.14}$$

$$F_{\rm BSYD,Smax}(R_c, h) = 1.098\left[1 - \exp\left(\frac{-\alpha_2}{R_c^{k_2}}\right)\right] \times \left[1 - \exp\left(\frac{-\alpha_1}{50^{k_1}}\right)\right] / \left[1 - \exp\left(\frac{-\alpha_2}{50^{k_2}}\right)\right], \tag{6.15}$$

where

$$\alpha_1 = \exp\left[1.84 + 0.094h - 0.09\exp(-11h)\right], \tag{6.16}$$

$$k_1 = 1.4 - 0.56h + 0.24\exp(-8.8h), \tag{6.17}$$

$$\alpha_2 = \exp\left[1.93 + 0.15h - 0.18\exp(-10h)\right], \tag{6.18}$$

$$k_2 = 1.32 - 0.49h + 0.18\exp(-9.5h). \tag{6.19}$$

In Figure 6.2, the times of the first and last crystal shipments are indicated by two thick dashed lines. During this time period the solar activity (or sunspot number) transitions from a minimum to almost a maximum. As an approximation, we assume that all crystals were shipped when the solar activity was exactly between its minimum and maximum levels (i.e., mid-level solar modulation). The value of F_{BSYD} in Equation 6.12 can then be approximated as the mean of $F_{\mathrm{BSYD,Smin}}$ and $F_{\mathrm{BSYD,Smax}}$. F_{BSYD} at locations along the crystal shipment route are given in Figure 6.3. The uncertainties quoted have been chosen so that F_{BSYD} plus (minus) the uncertainty gives $F_{\mathrm{BSYD,Smax}}$ ($F_{\mathrm{BSYD,Smin}}$). For the cosmogenic activation background analysis, F_{BSYD} is taken to be 0.73 ± 0.22 along the entire shipment route; this covers the entire range of F_{BSYD} values (including their uncertainties) given in Figure 6.3.

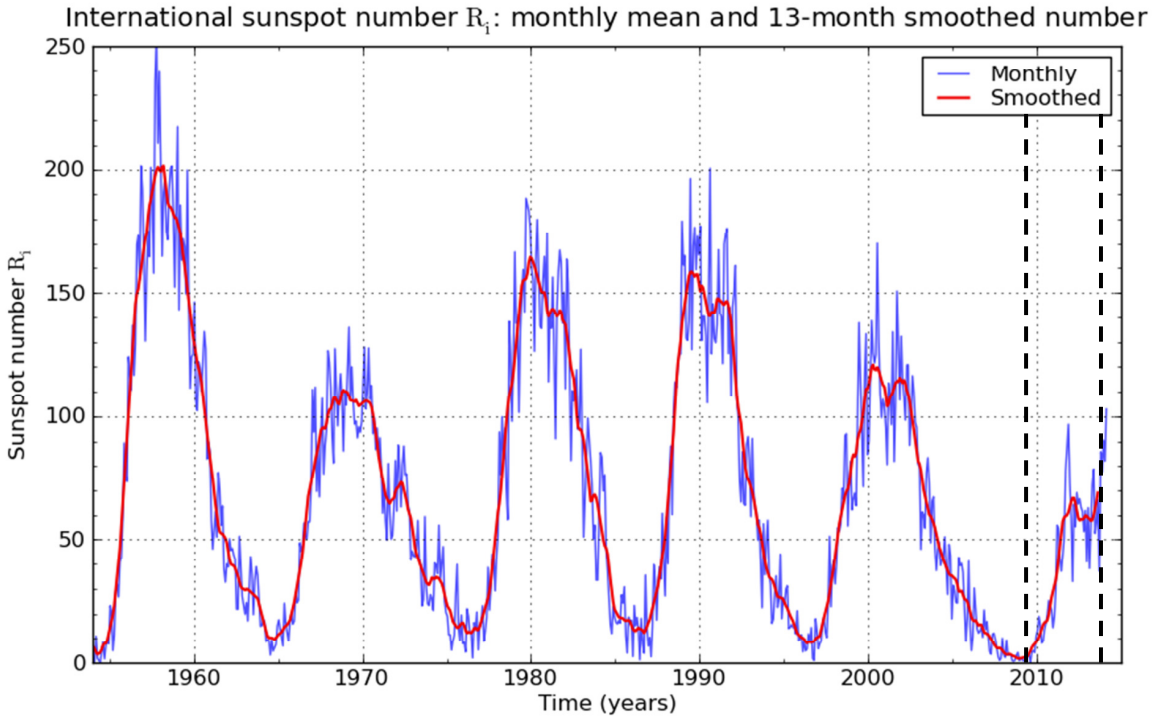

Figure 6.2: Monthly sunspot number for the past six (11-year) solar cycles. Sunspot number is a measure of solar activity; when the sunspot number of high, so is the solar activity, and vice versa. The figure was taken from the Solar Influences Data Analysis Center website, which is run by the Royal Observatory of Belgium [116]. The two thick dashed lines in the plot indicate the times of the first and last CUORE crystal shipments from Shanghai, China to LNGS.

The four integrated fluxes from Equation 6.7 were estimated using Equation 6.12 and Table A.1 [81], which reports neutron energy, E, in column two and $\varphi_0(E)$ in column three. Integrated fluxes were obtained by first creating a set of energy bins for the neutron energies in Table A.1. The ith bin was centered on E_i, the ith energy in the table, and had

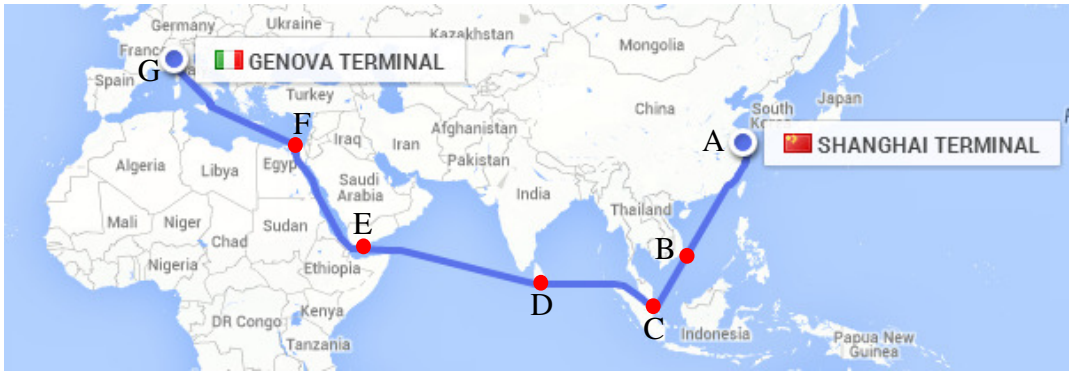

Location Label	Location	Latitude, Longitude	R_c (GV)	F_{BSYD}
A	Shanghai, China	31.2° N, 121.5° E	12.8	0.60 ± 0.02
B	Ho Chi Minh City, Vietnam	10.8° N, 106.6° E	16.8	0.52 ± 0.01
C	Singapore	1.3° N, 103.8° E	16.7	0.52 ± 0.01
D	Colombo, Sri Lanka	6.9° N, 79.9° E	16.9	0.52 ± 0.01
E	Ta'izz, Yemen	13.6° N, 44.0° E	15.4	0.55 ± 0.01
F	Port Said, Egypt	31.3° N, 32.3° E	10.4	0.67 ± 0.02
G	Genova, Italy	44.4° N, 8.9° E	4.7	0.89 ± 0.05

Figure 6.3: Shipping route from Shanghai, China to Genova, Italy. Several locations along the route have been labeled with the letters A-G. The latitude and longitude of each location is given in the table, along with the corresponding vertical geomagnetic cut-off rigidity, R_c, and F_{BSYD} value.

a width of ΔE_i. The bins used in this analysis are provided in column one of Table A.1. The value of $\varphi_0(E)$ in the entire energy range spanned by bin i was assumed to be $\varphi_0(E_i)$. Each integrated flux was then determined by numerically integrating over the relevant energy bins:

$$\begin{aligned}\int_{E_{min}}^{E_{max}} \varphi_{CR}(E)\mathrm{d}E &= F_{\mathrm{alt}} \cdot F_{\mathrm{BSYD}} \cdot \int_{E_{min}}^{E_{max}} \varphi_0(E)\mathrm{d}E \\ &\simeq F_{\mathrm{alt}} \cdot F_{\mathrm{BSYD}} \cdot \Big\{\varphi_0(E_i)[(E_i + \Delta E_i/2) - E_{min}] \\ &\quad + \sum_{j=i+1}^{k-1} \varphi_0(E_j)\Delta E_j \\ &\quad + \varphi_0(E_k)[E_{max} - (E_k - \Delta E_k/2)]\Big\}, \end{aligned} \tag{6.20}$$

where E_{min} and E_{max} are in bins i and k, respectively, $F_{\mathrm{alt}} = 1$, and $F_{\mathrm{BSYD}} = 0.73 \pm 0.22$. An uncertainty of 20% was assumed for the quantity in the square brackets. This takes into account the $\sim 4 - 15\%$ uncertainty in the neutron response functions used to obtain $\varphi_0(E)$ and the $\sim 4\%$ uncertainty in ignoring the slight dependence $\varphi_0(E)$ has on R_c [81].

6.2 GEANT4 simulations of ^{110m}Ag and ^{110}Ag contaminations in CUORE crystals

The GEANT4-based code qshields was used to determine the efficiencies $\epsilon_{110m}^{0\nu\beta\beta}$ and $\epsilon_{110}^{0\nu\beta\beta}$. The code was developed by the CUORE collaboration and is able to simulate the entire structure of the CUORE detector. The following components are included in the code:

- borated PET shield;
- external lead shield;
- six nested copper vessels of the cryostat along with their top plates;
- internal lead shields;
- copper plates inside the 10 mK shield, i.e., tower support plate, top and bottom plates enclosing detector array, etc.;
- copper frames that hold the TeO_2 crystals;
- copper columns that hold the copper frames together;
- TeO_2 crystals;
- wire trays;
- Cu-PEN cables;
- all the small parts such as copper screws, copper pins, PTFE parts, NTD thermistors, gold wires.

Figure 6.4a shows the detector geometry simulated in qshields; the PET shields and external lead shield have been excluded from the illustration. Figure 6.4b provides a detailed closeup of the simulated TeO_2 array.

For the simulations performed in this analysis, GEANT4 version 4.9.6 was used to run qshields. To obtain $\epsilon_{110m}^{0\nu\beta\beta}$ (or $\epsilon_{110}^{0\nu\beta\beta}$), a uniform contamination of ^{110m}Ag (^{110}Ag) was simulated by generating 10 million ^{110m}Ag (^{110}Ag) nuclei in the TeO_2 crystals. Each nucleus was created at a random position within one of the 988 crystals and allowed to decay. A histogram of the energy deposited in the crystals by each decay was recorded. Then, to take into account the ∼5-keV resolution of the CUORE bolometers, the histogram was convoluted with a Gaussian function that had a σ value of (5 keV)/2.35. The histograms for both Ag contaminations are shown in Figures 6.5a and 6.5b and are each labeled "Total."

The value of $\epsilon_{110m}^{0\nu\beta\beta}$ (or $\epsilon_{110}^{0\nu\beta\beta}$) can be obtained from the "Total" histogram using the following equation:

$$\epsilon_{110m(110)}^{0\nu\beta\beta} = \frac{C_{0\nu\beta\beta}}{N_D}, \tag{6.21}$$

where $C_{0\nu\beta\beta}$ is the number of counts in the $0\nu\beta\beta$ decay region of the histogram, i.e., 2497 - 2558 keV, and N_D is the number of ^{110m}Ag (^{110}Ag) decays that were simulated.

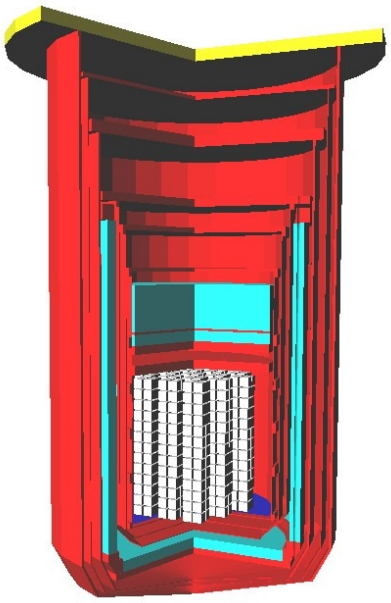

(a) CUORE detector geometry simulated in qshields. In red and yellow are the copper vessels and top plates of the cryostat. The copper plates inside the 10 mK shield are in red and blue. The internal lead shields are in cyan, and the TeO_2 array is in white. The PET shield and external lead shield have been excluded from this illustration.

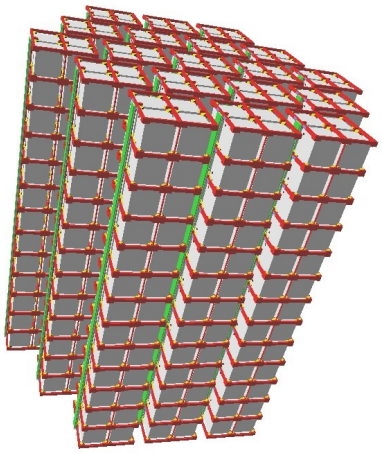

(b) Detailed closeup of the TeO_2 array. The copper frames and copper columns that hold the array together are in red. The TeO_2 crystals are in white. The wire trays are in green, and the PTFE parts are in yellow. Other small parts such as the copper screws and NTD thermistors are also shown, but are too small to be seen in the figure.

Figure 6.4: CUORE detector geometry simulated in qshields.

Table 6.6: Values for $\epsilon_{110m}^{0\nu\beta\beta}$ $\epsilon_{110}^{0\nu\beta\beta}$, and $\epsilon_{60}^{0\nu\beta\beta}$. In the row labeled "Total" are the efficiencies obtained from the "Total" histograms in Figures 6.5 and 6.7. In the row labeled "M1" are the efficiencies obtained from the "M1" histograms in Figures 6.5 and 6.7. The statistical uncertainties for the efficiencies ranged between ∼0.3 - 0.7 %, and the systematic uncertainties were assumed to be 10% [118]. The total uncertainties were determined by adding the statistical and systematic uncertainties in quadrature.

	$\epsilon_{110m}^{0\nu\beta\beta}$	$\epsilon_{110}^{0\nu\beta\beta}$	$\epsilon_{60}^{0\nu\beta\beta}$
Total	0.0049 ± 0.0005	0.0039 ± 0.0004	0.013 ± 0.001
M1	0.0021 ± 0.0002	0.0039 ± 0.0004	0.012 ± 0.001

The efficiencies obtained are provided in Table 6.6 in the row labeled "Total." It turns out that these two values are overestimations of the efficiencies because they do not account for CUORE's ability to veto, or identify, multi-site events. A multi-site event is one in which energy is deposited in multiple crystals. In CUORE, approximately 86% of ^{130}Te $0\nu\beta\beta$ decay events will be single-site, or so-called multiplicity 1, events [117], which deposit energy only in the crystal the decay originated in. CUORE has therefore chosen to decrease the background in the $0\nu\beta\beta$ region by discarding all multi-site events. For the ^{110m}Ag and ^{110}Ag simulations, discarding multi-site events results in the two histograms in Figures 6.5a and 6.5b labeled "M1," for "Multiplicity 1." The efficiencies obtained by applying Equation 6.21 to the "M1" histograms are given in Table 6.6 in the row labeled "M1." These two values are used in the cosmogenic activation background analysis discussed in this chapter. The statistical uncertainties in $\epsilon_{110m}^{0\nu\beta\beta}$ and $\epsilon_{110}^{0\nu\beta\beta}$ ranged between ∼0.5 - 0.7 %, and the systematic uncertainties were assumed to be 10% [118]. The total uncertainty was obtained by adding the statistical and systematic uncertainties in quadrature.

6.3 Estimation of the background in CUORE from cosmogenically produced ^{60}Co

In Ref. [11], ^{60}Co was produced by irradiating tellurium with protons at energies 800 MeV, 1.4 GeV, and 23 GeV. At energies this high, proton-interaction and neutron-interaction cross sections with tellurium can be assumed to be the same. ^{60}Co is problematic for CUORE because it has a long half-life of 5.27 y and a Q-value of 2823 keV; if produced in the TeO_2 crystals, it will contribute background in the $0\nu\beta\beta$ decay region. The decay scheme of ^{60}Co is shown in Figure 6.6. 99.88% of the time, ^{60}Co beta decays to the 2506-keV state of ^{60}Ni and produces an electron with energy between 0 and 318 keV. The 2506-keV state then decays to the ground state by emitting gammas and, with a tiny probability, conversion electrons. If these gammas and conversion electrons deposit all or most of their energy in the crystal the decay originated in, then their energy in addition to the energy of the 0 - 318-keV electron can result in an event in the $0\nu\beta\beta$ decay region.

^{60}Co has not yet been observed in gamma spectra taken for the TeO_2 powder irradiated at LANSCE. It is possible that the presence of ^{110m}Ag (250 d half-life, 3010-keV Q-value) and ^{102m}Rh (3.74 y half-life, 2323-keV Q-value) is currently obscuring the ^{60}Co peaks expected at 1173 keV and 1332 keV. It is also possible that not enough high energy

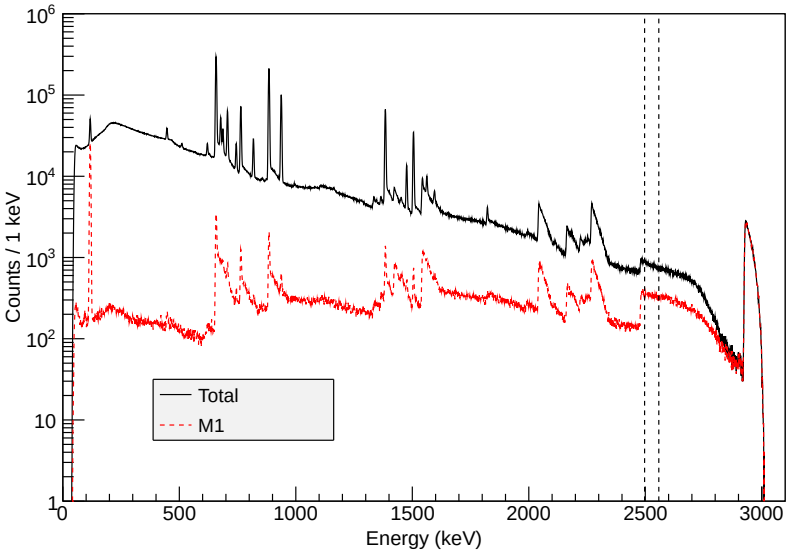

(a) Energy deposition histograms obtained from a qshields simulation of a uniform contamination of ^{110m}Ag in the TeO_2 crystals. The histogram labeled "Total" includes all ^{110m}Ag decay events, whereas the histogram labeled "M1" only includes multiplicity 1 events. The simulation had a threshold energy of 50 keV, i.e., energy depositions less than 50 keV were discarded.

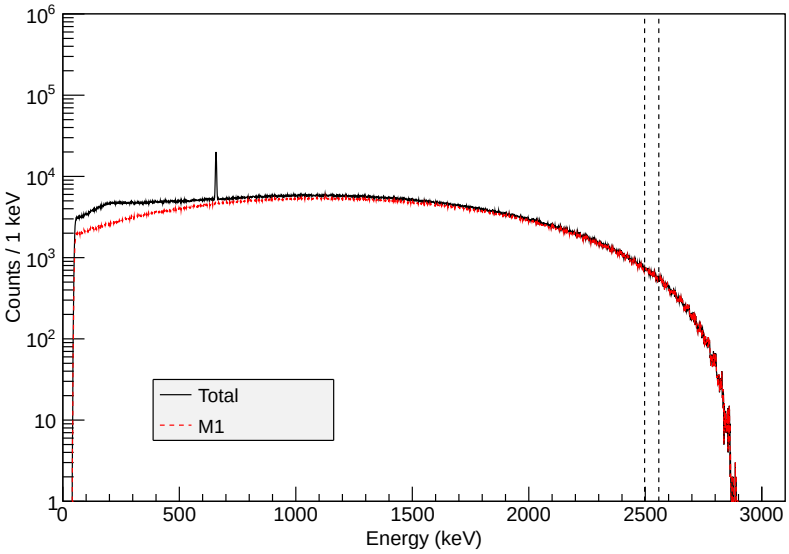

(b) Energy deposition histograms obtained from a qshields simulation of a uniform contamination of ^{110}Ag in the TeO_2 crystals. The histogram labeled "Total" includes all ^{110}Ag decay events, whereas the histogram labeled "M1" only includes multiplicity 1 events. The simulation had a threshold energy of 50 keV.

Figure 6.5: Energy deposited in the CUORE detector array by ^{110m}Ag and ^{110}Ag contaminations in the TeO_2 crystals. Results were obtained from two separate qshields simulations. In each plot, the $0\nu\beta\beta$ region (2497 - 2558 keV) is indicated with two vertical dotted lines.

neutrons interacted with tellurium to produce an observable amount of ^{60}Co. At the moment, the flux-averaged cross section for ^{60}Co, defined by Equation 5.21, is taken to be zero.

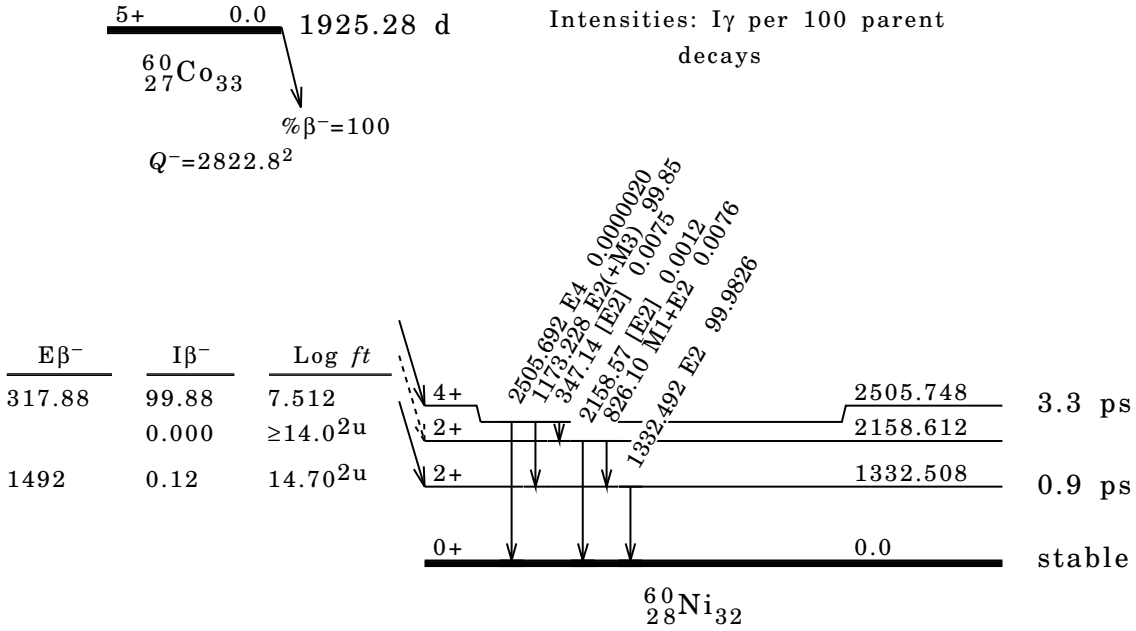

Figure 6.6: Decay scheme for ^{60}Co. Figure was obtained from Ref. [119]

To obtain an estimate of the background contribution in the $0\nu\beta\beta$ decay region from cosmogenically produced ^{60}Co in TeO_2, the three experimental Te(p,X)^{60}Co cross sections from Ref. [11] were used. These cross sections are given in Table 6.7. Equation 6.7 was used to determine the ^{60}Co production rate in a single TeO_2 crystal at sea-level; however in this case, $\bar{\sigma}_{30R} = 0$ mb and $\sigma_{0.8}$, $\sigma_{1.4}$, and σ_{23} are the Te(p,X)^{60}Co cross sections at 800 MeV, 1.4 GeV, and 23 GeV, respectively. The contamination level of ^{60}Co in a single crystal was then determined using the production rate, R_{CR}:

$$A'_{60}(t) = \frac{R_{CR}\left[1 - \exp(-\lambda_{60} t_{irrad})\right] \exp(-\lambda_{60} t)}{m_{xtal}}, \tag{6.22}$$

where λ_{60} is the decay constant for ^{60}Co, t_{irrad} is the time the crystal spends at sea-level, t is the time the crystal spends underground, and m_{xtal} is the mass of the crystal (0.750 kg). The average contamination levels of each batch of crystals at the start and end of CUORE are given in Table 6.8 and were obtained using

$$\bar{A}'_{60}(t_{s(e)}) = \frac{\sum_{i=1}^{N} A'_{60,i}(t_{s(e)})}{N}, \tag{6.23}$$

where $A'_{60,i}(t_{s(e)})$ is the contamination level in the ith crystal of the batch at the start (end) of counting and N is the total number of crystals in the batch. The contamination levels averaged over all the CUORE crystals are provided in the last row of Table 6.8.

The background rate $R'_{0\nu\beta\beta}(t)$ in the $0\nu\beta\beta$ decay region was determined from $A'_{60}(t)$:

Table 6.7: Measured cross sections for the reaction Te(p,X)^{60}Co. The energy, E, of the incoming proton is given in column one.

E	Cross-section (mb) [11]
800 MeV	0.09 ± 0.04
1.4 GeV	0.20 ± 0.04
23 GeV	0.75 ± 0.08

$$R'_{0\nu\beta\beta}(t) = \frac{A'_{60}(t)\epsilon_{60}^{0\nu\beta\beta}}{\Delta E_{0\nu\beta\beta}}, \tag{6.24}$$

where $\epsilon_{60}^{0\nu\beta\beta}$ is the probability that a ^{60}Co decay will result in a count in the $0\nu\beta\beta$ decay region and $\Delta E_{0\nu\beta\beta}$ is the width of the $0\nu\beta\beta$ decay region (2497 - 2558 keV). The parameter $\epsilon_{60}^{0\nu\beta\beta}$ was obtained by using qshields to simulate a uniform contamination of ^{60}Co in the TeO_2 crystals. A histogram of the energy deposited in the crystals by each decay was recorded and then convoluted with a Gaussian function to take into account the ∼5-keV resolution of the CUORE bolometers. The convoluted histogram is shown in Figure 6.7 and labeled "Total." Also in the figure is the histogram obtained after discarding all multi-site events; this is labeled "M1." The efficiency $\epsilon_{60}^{0\nu\beta\beta}$ can be obtained from each plot using

$$\epsilon_{60}^{0\nu\beta\beta} = \frac{C_{0\nu\beta\beta}}{N_D}, \tag{6.25}$$

where $C_{0\nu\beta\beta}$ is the number of counts in the $0\nu\beta\beta$ decay region, and N_D is the number of ^{60}Co decays, which was 10 million for the qshields simulation. Efficiencies determined from the "Total" and "M1" histograms are given in Table 6.6. Average background rates for each batch of crystals were obtained using Equation 6.11 and are listed in Table 6.9. The background rates averaged over all the CUORE crystals are given in the last row of the table. These two rates are orders of magnitude lower than CUORE's goal background, which demonstrates that ^{60}Co will not be problematic for CUORE.

Once again, a more pessimistic rate estimate can be obtained by assuming that no ^{60}Co was removed during crystal growth and that the activity of ^{60}Co had reached secular equilibrium. This gives rates that are ∼29 times higher than those in the last row of Table 6.9, but still orders of magnitude lower than CUORE's goal background.

Table 6.8: ^{60}Co contamination levels in CUORE crystals. The identification code and LNGS-arrival date of each batch of crystals are given in columns one and two. The number of crystals (N) is given in column three. The average irradiation time ($\bar{t}_{irrad}$) and average contamination levels at the start ($\bar{A}'_{60}(t_s)$) and end ($\bar{A}'_{60}(t_e)$) of CUORE are provided in the last three columns. The values of N, $\bar{t}_{irrad}$, $\bar{A}'_{60}(t_s)$, and $\bar{A}'_{60}(t_e)$ for *all* CUORE crystals are provided in the last row. Uncertainties are given in parentheses.

Batch Delivery ID	Batch Arrival Date	N	$\bar{t}_{irrad}$ (d)	$\bar{A}'_{60}(t_s)$ (Bq/kg)	$\bar{A}'_{60}(t_e)$ (Bq/kg)
US_01-s	2/6/2009	7	88	$5.52(269) \times 10^{-10}$	$2.86(139) \times 10^{-10}$
INFN_01	5/12/2009	25	109	$7.04(344) \times 10^{-10}$	$3.65(178) \times 10^{-10}$
INFN_02	6/4/2009	36	94	$6.14(300) \times 10^{-10}$	$3.18(155) \times 10^{-10}$
INFN_03	6/22/2009	32	89	$5.86(286) \times 10^{-10}$	$3.04(148) \times 10^{-10}$
INFN_04	9/29/2009	60	63	$4.32(211) \times 10^{-10}$	$2.24(109) \times 10^{-10}$
INFN_05	10/27/2009	34	67	$4.63(226) \times 10^{-10}$	$2.40(117) \times 10^{-10}$
INFN_06	11/25/2009	33	65	$4.54(222) \times 10^{-10}$	$2.35(115) \times 10^{-10}$
INFN_07	1/14/2010	34	90	$6.38(311) \times 10^{-10}$	$3.31(161) \times 10^{-10}$
INFN_08	1/19/2010	32	70	$4.99(243) \times 10^{-10}$	$2.58(126) \times 10^{-10}$
INFN_09	2/12/2010	27	74	$5.31(259) \times 10^{-10}$	$2.75(134) \times 10^{-10}$
INFN_10	5/11/2010	32	99	$7.31(356) \times 10^{-10}$	$3.79(185) \times 10^{-10}$
INFN_11	6/12/2010	32	94	$7.02(343) \times 10^{-10}$	$3.64(178) \times 10^{-10}$
INFN_12	7/14/2010	32	79	$5.96(291) \times 10^{-10}$	$3.09(151) \times 10^{-10}$
INFN_13	8/31/2010	32	90	$6.93(338) \times 10^{-10}$	$3.59(175) \times 10^{-10}$
INFN_14	10/11/2010	28	99	$7.72(377) \times 10^{-10}$	$4.00(195) \times 10^{-10}$
INFN_15	11/12/2010	32	90	$7.11(347) \times 10^{-10}$	$3.68(180) \times 10^{-10}$
INFN_16	12/21/2010	30	85	$6.82(333) \times 10^{-10}$	$3.53(172) \times 10^{-10}$
INFN_17	1/25/2011	30	88	$7.14(348) \times 10^{-10}$	$3.70(181) \times 10^{-10}$
US_01	3/1/2011	28	98	$8.04(392) \times 10^{-10}$	$4.17(203) \times 10^{-10}$
US_02	5/6/2011	28	69	$5.83(284) \times 10^{-10}$	$3.02(147) \times 10^{-10}$
US_03	6/24/2011	32	93	$7.96(388) \times 10^{-10}$	$4.13(201) \times 10^{-10}$
US_04	7/21/2011	31	82	$7.10(346) \times 10^{-10}$	$3.68(180) \times 10^{-10}$
US_05	9/5/2011	28	88	$7.74(378) \times 10^{-10}$	$4.01(196) \times 10^{-10}$
US_06	11/21/2011	28	75	$6.80(332) \times 10^{-10}$	$3.52(172) \times 10^{-10}$
US_07	2/7/2012	27	127	$1.17(57) \times 10^{-9}$	$6.08(297) \times 10^{-10}$
US_08	2/20/2012	26	110	$1.02(50) \times 10^{-9}$	$5.31(259) \times 10^{-10}$
US_09	4/11/2012	30	128	$1.21(59) \times 10^{-9}$	$6.27(306) \times 10^{-10}$
US_10	9/3/2012	32	104	$1.04(51) \times 10^{-9}$	$5.39(263) \times 10^{-10}$
US_11	11/5/2012	33	131	$1.33(65) \times 10^{-9}$	$6.91(337) \times 10^{-10}$
US_12	11/5/2012	32	101	$1.03(50) \times 10^{-9}$	$5.36(261) \times 10^{-10}$
US_13	12/10/2012	31	102	$1.06(52) \times 10^{-9}$	$5.48(267) \times 10^{-10}$
US_14	2/15/2013	30	101	$1.07(52) \times 10^{-9}$	$5.56(271) \times 10^{-10}$
US_15	4/23/2013	24	146	$1.58(77) \times 10^{-9}$	$8.16(398) \times 10^{-10}$
US_16	11/14/2013	24	288	$3.26(159) \times 10^{-9}$	$1.69(82) \times 10^{-9}$
All Crystals	—	1032	97	$8.31(405) \times 10^{-10}$	$4.30(210) \times 10^{-10}$

Table 6.9: Background rates in the $0\nu\beta\beta$ decay region due to ^{60}Co contamination in the CUORE crystals. The identification code and LNGS-arrival date of each batch of crystals are given in columns one and two. The number of crystals (N) is given in column three. The average irradiation time ($\bar{t}_{irrad}$) and average background rates at the start ($\bar{R}'_{0\nu\beta\beta}(t_s)$) and end ($\bar{R}'_{0\nu\beta\beta}(t_e)$) of CUORE are provided in the last three columns. The values of N, $\bar{t}_{irrad}$, $\bar{R}'_{0\nu\beta\beta}(t_s)$, and $\bar{R}'_{0\nu\beta\beta}(t_e)$ for *all* CUORE crystals are provided in the last row. Uncertainties are given in parentheses.

Batch Delivery ID	Batch Arrival Date	N	$\bar{t}_{irrad}$ (d)	$\bar{R}'_{0\nu\beta\beta}(t_s)$ (cts·keV^{-1}·kg^{-1}·y^{-1})	$\bar{R}'_{0\nu\beta\beta}(t_e)$ (cts·keV^{-1}·kg^{-1}·y^{-1})
US_01-s	2/6/2009	7	88	$3.38(199) \times 10^{-6}$	$1.75(103) \times 10^{-6}$
INFN_01	5/12/2009	25	109	$4.32(254) \times 10^{-6}$	$2.24(132) \times 10^{-6}$
INFN_02	6/4/2009	36	94	$3.77(222) \times 10^{-6}$	$1.95(115) \times 10^{-6}$
INFN_03	6/22/2009	32	89	$3.59(211) \times 10^{-6}$	$1.86(110) \times 10^{-6}$
INFN_04	9/29/2009	60	63	$2.65(156) \times 10^{-6}$	$1.37(81) \times 10^{-6}$
INFN_05	10/27/2009	34	67	$2.84(167) \times 10^{-6}$	$1.47(87) \times 10^{-6}$
INFN_06	11/25/2009	33	65	$2.79(164) \times 10^{-6}$	$1.45(85) \times 10^{-6}$
INFN_07	1/14/2010	34	90	$3.91(230) \times 10^{-6}$	$2.03(119) \times 10^{-6}$
INFN_08	1/19/2010	32	70	$3.06(180) \times 10^{-6}$	$1.59(93) \times 10^{-6}$
INFN_09	2/12/2010	27	74	$3.26(192) \times 10^{-6}$	$1.69(99) \times 10^{-6}$
INFN_10	5/11/2010	32	99	$4.48(264) \times 10^{-6}$	$2.32(137) \times 10^{-6}$
INFN_11	6/12/2010	32	94	$4.31(253) \times 10^{-6}$	$2.23(131) \times 10^{-6}$
INFN_12	7/14/2010	32	79	$3.66(215) \times 10^{-6}$	$1.90(112) \times 10^{-6}$
INFN_13	8/31/2010	32	90	$4.25(250) \times 10^{-6}$	$2.20(129) \times 10^{-6}$
INFN_14	10/11/2010	28	99	$4.74(279) \times 10^{-6}$	$2.45(144) \times 10^{-6}$
INFN_15	11/12/2010	32	90	$4.36(257) \times 10^{-6}$	$2.26(133) \times 10^{-6}$
INFN_16	12/21/2010	30	85	$4.18(246) \times 10^{-6}$	$2.17(127) \times 10^{-6}$
INFN_17	1/25/2011	30	88	$4.38(258) \times 10^{-6}$	$2.27(134) \times 10^{-6}$
US_01	3/1/2011	28	98	$4.93(290) \times 10^{-6}$	$2.56(150) \times 10^{-6}$
US_02	5/6/2011	28	69	$3.58(210) \times 10^{-6}$	$1.85(109) \times 10^{-6}$
US_03	6/24/2011	32	93	$4.89(287) \times 10^{-6}$	$2.53(149) \times 10^{-6}$
US_04	7/21/2011	31	82	$4.36(256) \times 10^{-6}$	$2.26(133) \times 10^{-6}$
US_05	9/5/2011	28	88	$4.75(279) \times 10^{-6}$	$2.46(145) \times 10^{-6}$
US_06	11/21/2011	28	75	$4.17(245) \times 10^{-6}$	$2.16(127) \times 10^{-6}$
US_07	2/7/2012	27	127	$7.20(423) \times 10^{-6}$	$3.73(219) \times 10^{-6}$
US_08	2/20/2012	26	110	$6.28(369) \times 10^{-6}$	$3.26(191) \times 10^{-6}$
US_09	4/11/2012	30	128	$7.42(436) \times 10^{-6}$	$3.85(226) \times 10^{-6}$
US_10	9/3/2012	32	104	$6.38(375) \times 10^{-6}$	$3.31(194) \times 10^{-6}$
US_11	11/5/2012	33	131	$8.18(481) \times 10^{-6}$	$4.24(249) \times 10^{-6}$
US_12	11/5/2012	32	101	$6.34(373) \times 10^{-6}$	$3.29(193) \times 10^{-6}$
US_13	12/10/2012	31	102	$6.49(381) \times 10^{-6}$	$3.36(198) \times 10^{-6}$
US_14	2/15/2013	30	101	$6.58(387) \times 10^{-6}$	$3.41(200) \times 10^{-6}$
US_15	4/23/2013	24	146	$9.67(568) \times 10^{-6}$	$5.01(294) \times 10^{-6}$
US_16	11/14/2013	24	288	$2.00(118) \times 10^{-5}$	$1.04(61) \times 10^{-5}$
All Crystals	—	1032	97	$5.10(300) \times 10^{-6}$	$2.64(155) \times 10^{-6}$

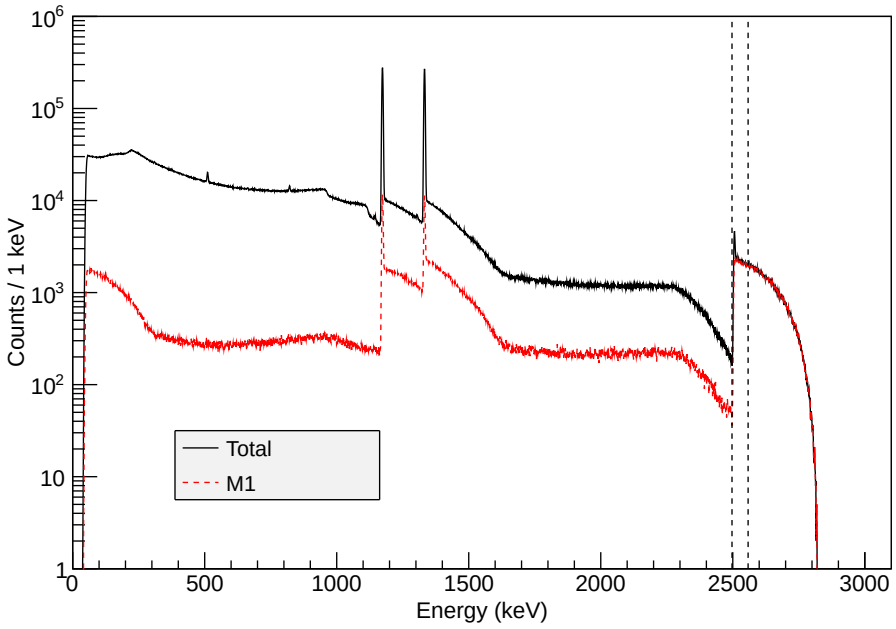

Figure 6.7: Energy deposited in the CUORE detector array by a ^{60}Co contamination in the TeO_2 crystals. Results were obtained from a qshields simulation of a uniform contamination of ^{60}Co in the TeO_2 array. The histogram labeled "Total" includes all ^{60}Co decay events, whereas the histogram labeled "M1" only includes multiplicity 1 events. The simulation had a threshold energy of 50 keV, i.e., energy depositions less than 50 keV were discarded. The $0\nu\beta\beta$ region (2497 - 2558 keV) is indicated with two vertical dotted lines.

Chapter 7

Conclusions

CUORE is one of the leading next-generation $0\nu\beta\beta$ decay experiments. It will search for the $0\nu\beta\beta$ decay of ^{130}Te using an array of 988 high-resolution, low-background cryogenic bolometers. The signature of $0\nu\beta\beta$ decay in CUORE is a peak at the Q-value of 2528 keV. Because $0\nu\beta\beta$ decay is expected to be extremely rare, it is essential that background sources that can mimic the decay signal be minimized. CUORE is aiming for a 1σ $0\nu\beta\beta$ decay half-life sensitivity of 1.6×10^{26} y, which can be obtained with a background rate of 10^{-2} counts/(keV·kg·y) at the decay peak and a live-time of five years. Achieving and maintaining a sufficiently low background rate requires comprehensive knowledge of all possible background sources. The CUORE Collaboration has successfully identified and analyzed a number of these. However, there are still a few sources that require further study, one of which is sea-level cosmogenic activation of the TeO_2 crystals that comprise the bolometers.

This dissertation discusses how the background from cosmogenic activation of TeO_2 was characterized using a cross-section measurement performed at the Los Alamos Neutron Science Center. In this measurement, a TeO_2 powder sample was irradiated with a spectrum of neutrons similar in shape to the cosmic-ray neutron spectrum at sea-level. ^{110m}Ag and its daughter ^{110}Ag were the only isotopes observed that can contribute background in the $0\nu\beta\beta$ decay region due to their decay Q-values being greater than 2528 keV and the half-life of ^{110m}Ag (250 d) being relatively long. A good estimate of the contribution to the $0\nu\beta\beta$ decay region from these two isotopes was obtained. The background rates at the beginning and end of CUORE were determined to be $(7.04 \pm 3.38) \times 10^{-5}$ counts/(keV·kg·y) and $(4.44 \pm 2.13) \times 10^{-7}$ counts/(keV·kg·y), respectively. While ^{60}Co was not observed in the measurement, it has been seen previously in proton activation experiments for tellurium. Therefore an estimate of its background contribution was also obtained. At the beginning and end of CUORE, the rates will be $(5.10 \pm 3.00) \times 10^{-6}$ counts/(keV·kg·y) and $(2.64 \pm 1.55) \times 10^{-6}$ counts/(keV·kg·y), respectively. The rates obtained for (^{110m}Ag + ^{110}Ag) and ^{60}Co are both much smaller than CUORE's goal background of 10^{-2} counts/(keV·kg·y) and will therefore not be an issue for CUORE.

Bibliography

[1] B. Kayser, Journal of Physics: Conference Series **173**, 012013 (2009).

[2] S. R. Elliot *et al.*, Physical Review Letters **59**, 2020 (1987).

[3] J. D. Vergados *et al.*, Reports on Progress in Physics **75**, 106301 (2012).

[4] F. Alessandria *et al.*, submitted to Astroparticle Physics (2011), `arXiv:1109.0494v2`.

[5] N. D. Scielzo *et al.*, Physical Review C **80**, 025501 (2009).

[6] F. Bellini *et al.*, Astroparticle Physics **33**, 169 (2010).

[7] F. Alessandria *et al.*, Astroparticle Physics **35**, 839 (2010).

[8] CUORE Collaboration, CUORE background budget, in preparation (2014).

[9] G. Heusser, Annual Review of Nuclear and Particle Science **45**, 543 (1995).

[10] *Experimental Nuclear Reaction Data (EXFOR), database version 4/22/2014*, URL `https://www-nds.iaea.org/exfor/exfor.htm`.

[11] A. F. Barghouty *et al.*, Nuclear Instruments and Methods in Physics Research B **295**, 16 (2013).

[12] J. Back *et al.*, Nuclear Instruments and Methods in Physics Research Section A: Accelerators, Spectrometers, Detectors and Associated Equipment **586**, 286 (2008).

[13] R. Silberberg *et al.*, The Astrophysical Journal Supplement Series No. 220(I) **25**, 315 (1973a).

[14] R. Silberberg *et al.*, The Astrophysical Journal Supplement Series No. 220(II) **25**, 335 (1973b).

[15] GALLEX Collaboration, W. Hampel *et al.*, Physics Letters B **447**, 127 (1999).

[16] SAGE Collaboration, J. N. Abdurashitov *et al.*, Physical Review C **60**, 055801 (1999).

[17] Super-Kamiokande Collaboration, Y. Fukuda *et al.*, Physical Review Letters **81**, 1158 (1998).

[18] KamLAND Collaboration, S. Abe *et al.*, Physical Review Letters **100**, 221803 (2008).

[19] M. H. Ahn *et al.*, Physical Review D **74**, 072003 (2006).

[20] P. Adamson *et al.*, Physical Review Letters **101**, 131802 (2008).

[21] Daya Bay Collaboration, F. P. An *et al.*, Physical Review Letters **108**, 171803 (2012).

[22] RENO Collaboration, J. K. Ahn *et al.*, Physical Review Letters **108**, 191802 (2012).

[23] G. L. Fogli *et al.*, Physical Review D **86**, 013012 (2012).

[24] V. N. Aseev *et al.*, Physics of Atomic Nuclei **75**, 464 (2012).

[25] J. Beringer *et al.*, Physical Review D **86**, 010001 (2012).

[26] A. P. Meshik *et al.*, Physical Review C **64**, 035205 (2001).

[27] M. Goeppert-Mayer, Physical Review **48**, 512 (1935).

[28] L. P. Ekstrom *et al.*, *WWW Table of Radioactive Isotopes, database version 2/28/99*, URL `http://ie.lbl.gov/toi/index.htm`.

[29] A. S. Barabash, Physical Review C **81**, 035501 (2010).

[30] KamLAND-Zen Collaboration, A. Gando *et al.*, Physical Review C **85**, 045504 (2012).

[31] H. V. Klapdor-Kleingrothaus *et al.*, Modern Physics Letters A **16**, 2409 (2001a).

[32] F. T. Avignone III *et al.*, Reviews of Modern Physics **80**, 481 (2008).

[33] S. M. Bilenky *et al.*, Modern Physics Letters A **27**, 1230015 (2012).

[34] T. Schwetz *et al.*, New Journal of Physics **13**, 109401 (2011).

[35] K. N. Abazajian *et al.*, Astroparticle Physics **35**, 177 (2011).

[36] KATRIN Collaboration, A. Osipowicz *et al.* (2001), `arXiv:hep-ex/0109033`.

[37] J. Wolf, Nuclear Instruments and Methods in Physics Research A **623**, 442 (2010).

[38] EXO Collaboration, M. Auger *et al.*, Physical Review Letters **109**, 032505 (2012).

[39] T. Bernatowicz *et al.*, Physical Review C **47**, 806 (1993).

[40] G. Audi *et al.*, Nuclear Physics A **729**, 337 (2003).

[41] S. Umehara *et al.*, Physical Review C **78**, 058501 (2008).

[42] B. J. Mount *et al.*, Physical Review C **81**, 032501 (2010).

[43] H. V. Klapdor-Kleingrothaus *et al.*, The European Physical Journal A **12**, 147 (2001b).

[44] W. Rodejohann, International Journal of Modern Physics E **20**, 1833 (2011).

[45] J. N. Nxumalo *et al.*, Physics Letters B **302**, 13 (1993).

[46] NEMO-3 Collaboration, R. Arnold *et al.*, Physical Review Letters **95**, 182302 (2005).

[47] NEMO-3 Collaboration, J. Argyriades *et al.*, Nuclear Physics A **847**, 168 (2010).

[48] S. Rahaman *et al.*, Physics Letters B **662**, 111 (2008).

[49] S. Rahaman *et al.*, Physics Letters B **703**, 412 (2011).

[50] F. Danevich *et al.*, Physical Review C **68**, 035501 (2003).

[51] M. A. Fehr *et al.*, International Journal of Mass Spectrometry **232**, 83 (2004).

[52] M. Redshaw *et al.*, Physical Review Letters **102**, 212502 (2009).

[53] C. Arnaboldi *et al.*, Physical Review C **78**, 035502 (2008).

[54] M. Redshaw *et al.*, Physical Review Letters **98**, 053003 (2007).

[55] R. Bernabei *et al.*, Physics Letters B **546**, 23 (2002).

[56] M. Zhao *et al.*, International Journal of Mass Spectrometry **245**, 36 (2005).

[57] NEMO-3 Collaboration, J. Argyriades *et al.*, Physical Review C **80**, 032501 (2009).

[58] H. V. Klapdor-Kleingrothaus *et al.*, Physics Letters B **586**, 198 (2004).

[59] H. V. Klapdor-Kleingrothaus *et al.*, Modern Physics Letters A **21**, 1547 (2006).

[60] GERDA Collaboration, M. Agostini *et al.*, Physical Review Letters **111**, 122503 (2013).

[61] GERDA Collaboration, K.-H. Ackermann *et al.*, The European Physical Journal C **73:2330**, 1 (2013).

[62] C. E. Aalseth *et al.*, Physics of Atomic Nuclei **63**, 1225 (2000).

[63] IGEX Collaboration, C. E. Aalseth *et al.*, Physical Review C **59**, 2108 (1999).

[64] MAJORANA Collaboration, E. Aguayo *et al.* (2011), `arXiv:1109.6913v1`.

[65] P. N. Luke *et al.*, IEEE Transactions on Nuclear Science **32**, 457 (1985).

[66] P. N. Luke, Nuclear Instruments and Methods in Physics Research A **271**, 567 (1988).

[67] CUORE Collaboration, C. Arnaboldi *et al.*, Nuclear Instruments and Methods in Physics Research Section A **518**, 775 (2004).

[68] SNO+ Collaboration, J. Hartnell, Journal of Physics: Conference Series **375** (2012), `doi:10.1088/1742-6596/375/4/042015`.

[69] SNO+ Collaboration, *SNO+*, URL `snoplus.phy.queensu.ca`.

[70] SuperNEMO Collaboration, A. Barabash, Journal of Physics: Conference Series **375** (2012), doi:10.1088/1742-6596/375/4/042012.

[71] C. Kittel, *Introduction to Solid State Physics* (John Wiley & Sons, Inc., 2005), 8th ed.

[72] C. Brofferio *et al.*, Nuclear Instruments and Methods in Physics Research Section A **718**, 211 (2013), ISSN 01689002.

[73] D. McCammon, Cryogenic Particle Detection, Topics in Applied Physics **99** (2005).

[74] D. R. Artusa *et al.*, submitted to Advances in High Energy Physics (2014), arXiv:1402.6072v1.

[75] M. Pavan, Nuclear Physics B - Proceedings Supplements **168**, 60 (2007).

[76] M. Ambrosio *et al.*, Astroparticle Physics **19**, 313 (2003).

[77] D.-M. Mei *et al.*, Physical Review D **73**, 053004 (2006).

[78] V. A. Kudryavtsev *et al.*, The European Physical Journal A **36**, 171 (2008).

[79] T. J. Dunai, *Cosmogenic Nuclides: Principles, Concepts and Applications in the Earth Surface Sciences* (Cambridge University Press, 2010).

[80] K. S. Krane, *Introductory Nuclear Physics* (John Wiley & Sons, 1988).

[81] M. Gordon *et al.*, IEEE Transactions on Nuclear Science **51**, 3427 (2004).

[82] J. J. Duderstadt *et al.*, *Nuclear Reactor Analysis* (John Wiley & Sons, 1976).

[83] S. A. Wender *et al.*, Nuclear Instruments and Methods in Physics Research A **336**, 226 (1993).

[84] R. E. Slovacek *et al.*, Nuclear Science and Engineering **62**, 455 (1977).

[85] O. A. Shcherbakov *et al.*, International Seminar on Interactions of Neutrons with Nuclei **9**, 257 (2001).

[86] V. I. Goldansky *et al.*, Doklady Akademii Nauk **101**, 1027 (1955).

[87] S. A. Wender, private communication (2012).

[88] G. F. Knoll, *Radiation Detection and Measurement* (John Wiley & Sons, Inc., 2000), 3rd ed.

[89] K. Thomas *et al.*, Nuclear Instruments and Methods in Physics Research A **724**, 47 (2013).

[90] D. Radford, *RadWare*, URL radware.phy.ornl.gov.

[91] S. G. Prussin, *Nuclear Physics for Applications* (WILEY-VCH Verlag GmbH & Co. KGaA, 2007).

[92] T-2 Nuclear Information Service, *Qtool: Calculation of Reaction Q-values and Thresholds* (1997), URL `http://t2.lanl.gov/nis/data/qtool.html`.

[93] D. J. Griffiths, *Introduction to Quantum Mechanics* (Pearson Prentice Hall, 2005), 2nd ed.

[94] G. Gilmore, *Practical Gamma-ray Spectroscopy* (John Wiley & Sons, Ltd, 2008), 2nd ed.

[95] S. Agostinelli *et al.*, Nuclear Instruments and Methods in Physics Research Section A **506**, 250 (2003).

[96] J. Allison *et al.*, IEEE Transactions on Nuclear Science **53**, 270 (2006).

[97] J. Taylor, *An introduction to error analysis: The study of uncertainties in physical measurements* (University Science Books, 1997), 2nd ed.

[98] M. C. Perillo Isaac *et al.*, Nuclear Instruments and Methods in Physics Research A **397**, 310 (1997).

[99] R. R. Kinsey *et al.*, paper submitted to the 9th International Symposium of Capture Gamma-Ray Spectroscopy and Related Topics, Budapest, Hungary (1996), URL `http://www.nndc.bnl.gov/nudat2/chartNuc.jsp`.

[100] P. R. Bevington, *Data Reduction and Error Analysis for the Physical Sciences* (McGraw-Hill Inc., 1969).

[101] R. Brun *et al.*, Nuclear Instruments and Methods in Physics Research A **389**, 81 (1997).

[102] J. Katakura *et al.*, Nuclear Data Sheets **97**, 765 (2002).

[103] C. P. Robert *et al.*, *Monte Carlo statistical methods* (Springer Science+Business Media Inc., 2004), 2nd ed.

[104] *GA-MA and Associates, Inc.*, URL `www.ga-maassociates.com`.

[105] J. Boson *et al.*, Nuclear Instruments and Methods in Physics Research A **587**, 304 (2008).

[106] R. Helmer *et al.*, Nuclear Instruments and Methods in Physics Research A **511**, 360 (2003).

[107] Z. Wang *et al.*, IEEE Transactions on Nuclear Science **49**, 1925 (2002).

[108] B. Quiter, Masters, University of California, Berkeley (2005).

[109] C. Arnaboldi *et al.*, Journal of Crystal Growth **312**, 2999 (2010).

[110] D. Lal *et al.*, in *Cosmic Rays II* (Springer Berlin Heidelberg, 1967), p. 551.

[111] *Geomagsphere*, URL `http://www.geomagsphere.org/geomag/`.

[112] P. Bobik *et al.*, Journal of Geophysical Research **111** (2006).

[113] C. C. Finlay *et al.*, Geophysical Journal International **183**, 1216 (2010).

[114] N. A. Tsyganenko *et al.*, Journal of Geophysical Research **101**, 27187 (1996).

[115] A. Darrin *et al.*, *Handbook of Space Engineering, Archaeology, and Heritage* (Taylor & Francis, 2010).

[116] *SILSO, Royal Observatory of Belgium, Brussels*, URL `http://sidc.be/silso/home`.

[117] A. Bryant, Ph.D. thesis, University of California, Berkeley (2010).

[118] L. Pandola *et al.*, Nuclear Instruments and Methods in Physics Research Section A **570**, 149 (2007).

[119] Nuclear Data Sheets **114**, 1849 (2013).

[120] D. Filges *et al.*, *Handbook of Spallation Research: Theory, Experiments and Applications* (WILEY-VCH Verlag GmbH & Co. KGaA, Weinheim, 2009).

[121] Super-Kamiokande Collaboration, Y. Fukuda *et al.*, Physical Review Letters **81**, 1562 (1998).

[122] X. Huang, Nuclear Data Sheets **110**, 2533 (2009).

[123] B. Quiter, private communication (2013).

[124] J. K. Tuli, Nuclear Data Sheets **100**, 347 (2003).

[125] *Evaluated Nuclear Data File (ENDF), database version 3/14/2014*, URL `https://www-nds.iaea.org/exfor/endf.htm`.

Appendix A

Neutron flux tables

Table A.1: The differential cosmic-ray neutron flux, $\varphi_0(E)$, in New York City, New York at sea-level and at mid-level solar modulation. The neutron energy, E, is listed in column two. The information in this table was taken from Ref. [81]. The spectrum was not measured; however, it was derived from neutron spectrum measurements taken at five different locations of varying altitudes. Energy bins used in the cosmogenic activation background analysis from Chapter 6 are listed in column one.

Bin Range (MeV)	E (MeV)	$\varphi_0(E)$ ($cm^{-2} \cdot s^{-1} \cdot MeV^{-1}$)
0.9985 - 1.110	1.054	6.83×10^{-4}
1.110 - 1.221	1.165	8.19×10^{-4}
1.221 - 1.354	1.287	7.61×10^{-4}
1.354 - 1.493	1.423	7.02×10^{-4}
1.493 - 1.652	1.572	6.00×10^{-4}
1.652 - 1.825	1.738	5.72×10^{-4}
1.825 - 2.016	1.920	5.06×10^{-4}
2.016 - 2.229	2.122	5.02×10^{-4}
2.229 - 2.464	2.346	5.44×10^{-4}
2.464 - 2.721	2.592	4.30×10^{-4}
2.721 - 3.010	2.865	3.34×10^{-4}
3.010 - 3.323	3.166	2.65×10^{-4}
3.323 - 3.676	3.499	1.86×10^{-4}
3.676 - 4.059	3.867	1.64×10^{-4}
4.059 - 4.490	4.274	1.73×10^{-4}
4.490 - 4.959	4.724	1.88×10^{-4}
4.959 - 5.482	5.220	1.53×10^{-4}
5.482 - 6.057	5.769	1.25×10^{-4}
6.057 - 6.696	6.376	1.16×10^{-4}
6.696 - 7.399	7.047	8.90×10^{-5}
7.399 - 8.178	7.788	7.16×10^{-5}
8.178 - 9.037	8.607	6.73×10^{-5}
9.037 - 9.988	9.512	5.53×10^{-5}

Continued on next page

Table A.1 – continued from previous page

Bin Range (MeV)	E (MeV)	$\varphi_0(E)$ ($cm^{-2}{\cdot}s^{-1}{\cdot}MeV^{-1}$)
9.988 - 11.03	10.51	4.58×10^{-5}
11.03 - 12.21	11.62	4.09×10^{-5}
12.21 - 13.47	12.84	3.80×10^{-5}
13.47 - 14.91	14.19	3.44×10^{-5}
14.91 - 17.41	16.16	3.02×10^{-5}
17.41 - 19.63	18.52	3.22×10^{-5}
19.63 - 31.77	25.70	2.59×10^{-5}
31.77 - 56.61	44.19	2.09×10^{-5}
56.61 - 95.35	75.98	1.53×10^{-5}
95.35 - 166.0	130.7	9.64×10^{-6}
166.0 - 283.2	224.6	4.30×10^{-6}
283.2 - 489.4	386.3	1.33×10^{-6}
489.4 - 839.0	664.2	3.99×10^{-7}
839.0 - 1445	1.142×10^{3}	1.02×10^{-7}
1.445×10^{3} - 2.483×10^{3}	1.964×10^{3}	2.24×10^{-8}
2.483×10^{3} - 4.269×10^{3}	3.376×10^{3}	3.36×10^{-9}
4.269×10^{3} - 7.341×10^{3}	5.805×10^{3}	4.71×10^{-10}
7.341×10^{3} - 1.262×10^{4}	9.982×10^{3}	9.87×10^{-11}
1.262×10^{4} - 2.170×10^{4}	1.716×10^{4}	3.83×10^{-11}
2.170×10^{4} - 3.732×10^{4}	2.951×10^{4}	8.60×10^{-12}
3.732×10^{4} - 6.416×10^{4}	5.074×10^{4}	2.17×10^{-12}
6.416×10^{4} - 1.103×10^{5}	8.725×10^{4}	6.97×10^{-13}
1.103×10^{5} - 1.897×10^{5}	1.500×10^{5}	1.88×10^{-13}

Table A.2: The LANSCE 30R differential neutron flux, $\varphi_{30R}(E)$, at the location of the ^{238}U fission ionization chamber. The neutron-energy-bin ranges used to record the flux are listed in column one, and the average energy, E, of each bin is given in column two.

Bin Range (MeV)	E (MeV)	$\varphi_{30R}(E)$ ($cm^{-2}{\cdot}s^{-1}{\cdot}MeV^{-1}$)
1.25 - 1.5	1.375	2.14×10^{5}
1.5 - 1.75	1.625	2.36×10^{5}
1.75 - 2	1.875	2.04×10^{5}
2 - 2.25	2.125	1.82×10^{5}
2.25 - 2.5	2.375	1.67×10^{5}
2.5 - 2.75	2.625	1.50×10^{5}
2.75 - 3	2.875	1.36×10^{5}
3 - 3.5	3.25	1.20×10^{5}
3.5 - 4	3.75	1.02×10^{5}
4 - 4.5	4.25	8.80×10^{4}
4.5 - 5	4.75	7.75×10^{4}
5 - 5.5	5.25	6.59×10^{4}

Continued on next page

Table A.2 – continued from previous page

Bin Range (MeV)	E (MeV)	$\varphi_{30R}(E)$ ($cm^{-2} \cdot s^{-1} \cdot MeV^{-1}$)
5.5 - 6	5.75	5.60×10^4
6 - 7	6.5	4.56×10^4
7 - 8	7.5	3.59×10^4
8 - 9	8.5	2.82×10^4
9 - 10	9.5	2.28×10^4
10 - 12.5	11.25	1.61×10^4
12.5 - 15	13.75	1.05×10^4
15 - 17.5	16.25	8.52×10^3
17.5 - 20	18.75	7.05×10^3
20 - 22.5	21.25	6.25×10^3
22.5 - 25	23.75	5.73×10^3
25 - 27.5	26.25	5.20×10^3
27.5 - 30	28.75	4.89×10^3
30 - 35	32.5	4.62×10^3
35 - 40	37.5	4.18×10^3
40 - 45	42.5	3.84×10^3
45 - 50	47.5	3.66×10^3
50 - 55	52.5	3.42×10^3
55 - 60	57.5	3.21×10^3
60 - 70	65	2.91×10^3
70 - 80	75	2.58×10^3
80 - 90	85	2.31×10^3
90 - 100	95	2.10×10^3
100 - 125	112.5	1.82×10^3
125 - 150	137.5	1.48×10^3
150 - 175	162.5	1.22×10^3
175 - 200	187.5	1.03×10^3
200 - 225	212.5	8.80×10^2
225 - 250	237.5	7.70×10^2
250 - 275	262.5	6.75×10^2
275 - 300	287.5	6.06×10^2
300 - 350	325	5.27×10^2
350 - 400	375	4.48×10^2
400 - 450	425	3.78×10^2
450 - 500	475	3.02×10^2
500 - 550	525	2.09×10^2
550 - 600	575	1.22×10^2
600 - 700	650	3.94×10^1
700 - 800	750	4.65×10^0

Appendix B

Neutron flux below 1.25 MeV

At LANSCE, 800 MeV protons bombard a tungsten target and create spallation neutrons with energies up to ∼800 MeV. Figure B.1 shows the neutron spectrum, or more specifically the neutron yield versus neutron energy, for a typical spallation neutron source. Most of the neutrons are produced with energies above ∼0.01 MeV. Below this threshold, the neutron yield becomes increasingly small.

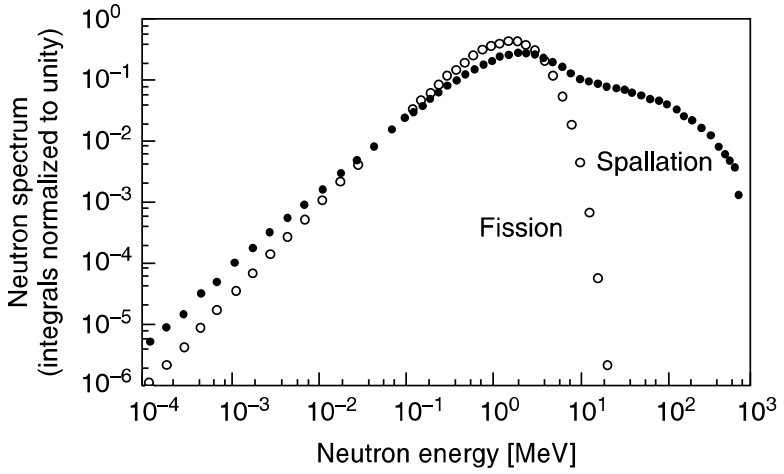

Figure B.1: Figure taken from Ref. [120]. Typical "neutron yield versus neutron energy" plots for spallation and thermal neutron fission of ^{235}U. The spallation neutrons were created by 800 MeV protons bombarding a 10-cm-diameter, 30-cm-long tungsten target. The spallation spectrum was measured at an angle 90° relative to the direction of the proton beam.

During the TeO_2 irradiation, there was a measureable neutron flux below 0.01 MeV; these neutrons had energies that extended all the way down to thermal. Most of this flux was due to fast neutrons (0.1 MeV - 10 MeV) [79] slowing down after colliding with nuclei in surrounding materials. Since these neutrons and all other neutrons with energies less than 1.25 MeV were not recorded by the fission ionization chamber during the irradiation, gold foils (Au1 and Au2 from Figure 5.2) were placed outside and inside the cadmium layer of the TeO_2 target stack to monitor the flux.

The neutron flux below 1.25 MeV can be estimated by looking at the production rate of ^{198}Au in each foil. ^{198}Au is generated by the reaction ^{197}Au(n,γ). The production

rate, R, can be obtained using the gamma spectra collected for the foils. As was done for the TeO_2 powder spectra, RadWare was used to fit each peak in the gold foil spectra with a Gaussian or Gaussian-like function summed with a quadratic function, and peaks belonging to ^{198}Au were identified. For each foil, only one ^{198}Au peak was observed. It corresponded to the 411.8-keV gamma that is emitted with a 95.62% branching ratio [122]. The first step to obtaining R is to use the number of counts, $C_{411.8}$, in the 411.8-keV peak to get the number of ^{198}Au decays, N_d, that occurred during gamma counting:

$$N_d = \frac{C_{411.8}}{B_{411.8}\epsilon_{411.8}}, \tag{B.1}$$

Here, $B_{411.8}$ and $\epsilon_{411.8}$ are respectively the branching ratio (divided by 100%) and photopeak efficiency of the 411.8-keV gamma. Since the 411.8-keV gamma is emitted in coincidence with another gamma less than 1% of the time, $\epsilon_{411.8}$ can be taken to be

$$\epsilon_{411.8} = \frac{\text{number of 411.8-keV gammas depositing full energy in detector}}{\text{number of 411.8-keV gammas emitted by gold foil}}. \tag{B.2}$$

The next step in the analysis is to express N_d in terms of R:

$$N_d = \frac{R[1-\exp(-\lambda t_{irrad})]}{\lambda}[\exp(-\lambda t_s) - \exp(-\lambda t_e)], \tag{B.3}$$

Here, λ is the decay constant for ^{198}Au, t_{irrad} is the neutron irradiation time, and t_s and t_e are respectively the start time and end time of gamma counting relative to the end of the irradiation. Now, using Equations B.1 and B.3, the production rate for ^{198}Au can be expressed as

$$R = \frac{\lambda C_{411.8}}{B_{411.8}\epsilon_{411.8}[\exp(-\lambda t_s) - \exp(-\lambda t_e)][1-\exp(-\lambda t_{irrad})]} \tag{B.4}$$

In Equation B.4, every parameter except for $\epsilon_{411.8}$ is known. $\epsilon_{411.8}$ can be obtained by using several point sources to map out the photopeak efficiency as a function of gamma energy for the gold foils. The two gold foils have essentially identical dimensions (2.54 cm in diameter, 0.005 cm thick), and each foil was gamma counted 12 cm away from the face of the HPGe detector. For this foil size and counting distance, it is sufficient to approximate each gold foil as a point source. To obtain the photopeak efficiency, ϵ_γ, as a function of gamma energy, E_γ, ^{133}Ba, ^{54}Mn, and ^{60}Co point sources were each gamma counted 12 cm away from the face of the HPGe detector. Each point source was configured so that the center of the source was aligned with the center of the detector. ^{54}Mn emits only a single 834.8-keV gamma when it decays. ^{133}Ba and ^{60}Co emit multiple gammas in coincidence, which means that there is a probability for more than one gamma to enter the detector at the same time. However, at 12 cm this probability is small enough to be ignored. Thus, for all three point sources, it is sufficient to assume that all gammas entering the detector do so one at a time. The photopeak efficiency at E_γ can then be expressed as

$$\epsilon_\gamma = \frac{\text{Number of gammas with energy } E_\gamma \text{ depositing full energy in detector}}{\text{Number of gammas with energy } E_\gamma \text{ emitted by point source}}. \tag{B.5}$$

Table B.1: Values of parameters from Equation B.6 for gammas emitted by ^{133}Ba, ^{54}Mn, and ^{60}Co point sources. Errors have been added in quadrature to get error on ϵ_γ.

Source	A (Bq)	t (s)	E_γ (keV)	B_γ (%)	C_γ	ϵ_γ
^{133}Ba	31094 ± 933	1200	276.4	7.16 ± 0.05	22750 ± 165	$(8.5 \pm 0.3) \times 10^{-3}$
			302.9	18.34 ± 0.13	55317 ± 242	$(8.1 \pm 0.3) \times 10^{-3}$
			356	62.05 ± 0	169883 ± 415	$(7.3 \pm 0.2) \times 10^{-3}$
			383.8	8.94 ± 0.06	23606 ± 155	$(7.1 \pm 0.2) \times 10^{-3}$
^{54}Mn	2486 ± 75	12000.02	834.8	99.976 ± 0.001	130560 ± 363	$(4.4 \pm 0.1) \times 10^{-3}$
^{60}Co	9212 ± 294	6000	1173	99.85 ± 0.03	193461 ± 446	$(3.5 \pm 0.1) \times 10^{-3}$
			1332	99.9826 ± 0.0006	178987 ± 424	$(3.2 \pm 0.1) \times 10^{-3}$

Table B.2: Parameters used to obtain the ^{198}Au production rate, R, in each gold foil. Also shown are the lower and upper limits on the neutron flux below 1.25 MeV that were derived from an alternative expression of R.

Parameter	Value for Foil Au1	Value for Foil Au2
λ	2.98×10^{-6} s^{-1}	2.98×10^{-6} s^{-1}
$C_{411.8}$	13551 ± 119	15270 ± 128
$B_{411.8}$	95.62%	95.62%
$\epsilon_{411.8}$	$(6.7 \pm 0.2) \times 10^{-3}$	$(6.7 \pm 0.2) \times 10^{-3}$
t_{irrad}	154487 s	154487 s
t_s	349190 s	633153 s
t_e	373190 s	696153 s
R	700 ± 23 s^{-1}	740 ± 24 s^{-1}
$\phi_{<1.25,lo}$	$\sim$16 n/(cm^2·s)	$\sim$17 n/(cm^2·s)
$\phi_{<1.25,hi}$	$\sim 4.1 \times 10^7$ n/(cm^2·s)	$\sim 4.4 \times 10^7$ n/(cm^2·s)

Alternatively, Equation B.5 can be written as

$$\epsilon_\gamma = \frac{C_\gamma}{AB_\gamma t}, \tag{B.6}$$

where C_γ is the number of counts in the peak centered at E_γ, A is the activity of the point source during gamma counting, B_γ is the branching ratio (expressed as a fraction of 100%) for emitting gammas with energy E_γ, and t is the total live time of the measurement. The values of C_γ, A, B_γ, t, and ϵ_γ are given in Table B.1 for all E_γ considered in this analysis. The photopeak efficiency as a function of gamma energy is shown in Figure B.2. The points in the plot have been fit with the equation

$$\epsilon_\gamma = \exp\left[a + b\ln(E_\gamma)\right], \tag{B.7}$$

which is a common choice of function to describe efficiency curves [94]. The fit was performed by implementing the least squares method in ROOT. The results are also shown in the figure. Plugging $E_\gamma = 411.8$ keV into Equation B.7, with $a = -1.29 \pm 0.12$ and $b = -0.62 \pm 0.02$, gives a photopeak efficiency of $(6.7 \pm 0.2) \times 10^{-3}$.

Now, using Equation B.4 and values from Table B.2 we get $R = 700 \pm 23$ s^{-1} for foil Au1 and $R = 740 \pm 24$ s^{-1} for foil Au2.

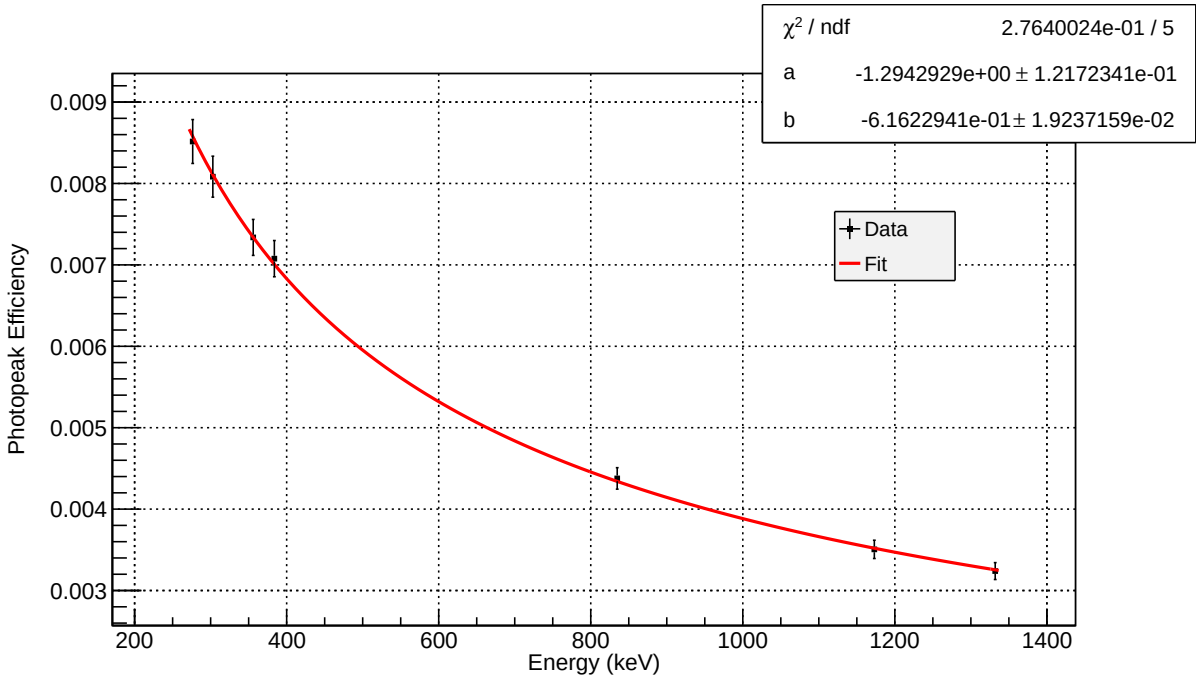

Figure B.2: Photopeak efficiencies for ^{133}Ba, ^{54}Mn and ^{60}Co point sources placed 12 cm away from HPGe detector face. The data points have been fit with Equation B.7.

To get an estimate of the neutron flux below 1.25 MeV, R needs to be expressed in an alternative way:

$$R = N \int_0^{800} \sigma(E)\varphi(E)\mathrm{d}E, \tag{B.8}$$

where N is the number of ^{197}Au nuclei in the foil, E is the neutron energy, $\sigma(E)$ is the ^{197}Au(n,γ)^{198}Au cross section, $\varphi(E)$ is the differential neutron flux in units of [neutrons/(cm^2·s·MeV)] at the location of the foil, and the limits of the integral are in units of [MeV]. Equation B.8 can then be rewritten as

$$\frac{R}{N} = \int_0^{800} \sigma(E)\varphi(E)\mathrm{d}E \simeq \int_0^{1.25} \sigma(E)\varphi(E)\mathrm{d}E + \sum_{i=1}^{N_{bin}} \sigma(E_i)\varphi_{30R}(E_i)\Delta E_i, \tag{B.9}$$

where the second term on the right-hand side of the equation is the discrete form of $\int_{1.25}^{800} \sigma(E)\varphi(E)\mathrm{d}E$. The summation has been carried out over all the neutron-energy bins used by the fission chamber to record the flux. Here, it is assumed that the differential neutron flux above 1.25 MeV does not change while neutrons travel from the fission chamber to both gold foils. This assumption is valid because the target components lying between the fission chamber and the two gold foils are not thick enough to significantly alter the neutron beam above 1.25 MeV; refer to Figure 5.10. The parameter $\varphi_{30R}(E_i)$ in Equation B.9 is the 30R differential neutron flux in energy bin i recorded by the fission chamber, E_i is the central energy of bin i, ΔE_i is the width of bin i, $\sigma(E_i)$ is the cross section at energy E_i, and N_{bin} is the total number of energy bins used to record the flux at the fission chamber.

The ^{197}Au(n,γ)^{198}Au cross section has been measured over a large neutron-energy range, from thermal up to ∼15 MeV [10]. In Figure B.3, measured cross sections are compared with evaluated cross sections from the Evaluated Nuclear Data File (ENDF) website [125]. The ENDF data is consistent with the measured data, and because it also covers energies up to 200 MeV, the ENDF data is used in Equation B.9 to get an estimate of the neutron flux below 1.25 MeV. To obtain each $\sigma(E_i)$, linear interpolation was performed between the pair of ENDF data points bracketing E_i. In Figure B.3, the highest ENDF cross section, σ_{hi}, and lowest ENDF cross section, σ_{lo}, for $E < 1.25$ MeV are indicated by a solid line and a dotted line, respectively. By assuming $\sigma(E < 1.25) = \sigma_{hi}$, one gets a lower limit on the neutron flux below 1.25 MeV, $\phi_{<1.25,lo}$:

$$\phi_{<1.25,lo} = \frac{1}{\sigma_{hi}} \left(\frac{R}{N} - \sum_{i=1}^{N_{bin}} \sigma(E_i)\varphi_{30R}(E_i)\Delta E_i \right). \tag{B.10}$$

Likewise, by assuming $\sigma(E < 1.25) = \sigma_{lo}$, one gets an upper limit on the flux, $\phi_{<1.25,hi}$:

$$\phi_{<1.25,hi} = \frac{1}{\sigma_{lo}} \left(\frac{R}{N} - \sum_{i=1}^{N_{bin}} \sigma(E_i)\varphi_{30R}(E_i)\Delta E_i \right). \tag{B.11}$$

Both $\phi_{<1.25,lo}$ and $\phi_{<1.25,hi}$ are in units of [neutrons/(cm^2·s·MeV)]. For each gold foil, the flux limits are given in Table B.2. The actual flux at each gold foil is probably on the order of 10^5-10^6 n/(cm^2·s). This is because, assuming a smooth neutron flux-shape at low energies, most of the flux for $E < 1.25$ MeV should be above 0.01 MeV, and the average cross section for $0.01 < E < 1.25$ MeV is around 0.1-1 b.

Examining the flux limits for Au1 and Au2, it is apparent that the fluxes at both foils are comparable, even though neutrons with $E \lesssim 0.3$ eV were almost completely removed by cadmium before the neutron beam reached Au2. This effect should be due to higher energy neutrons slowing down after interacting with nuclei in the cadmium foil and the plastic container.

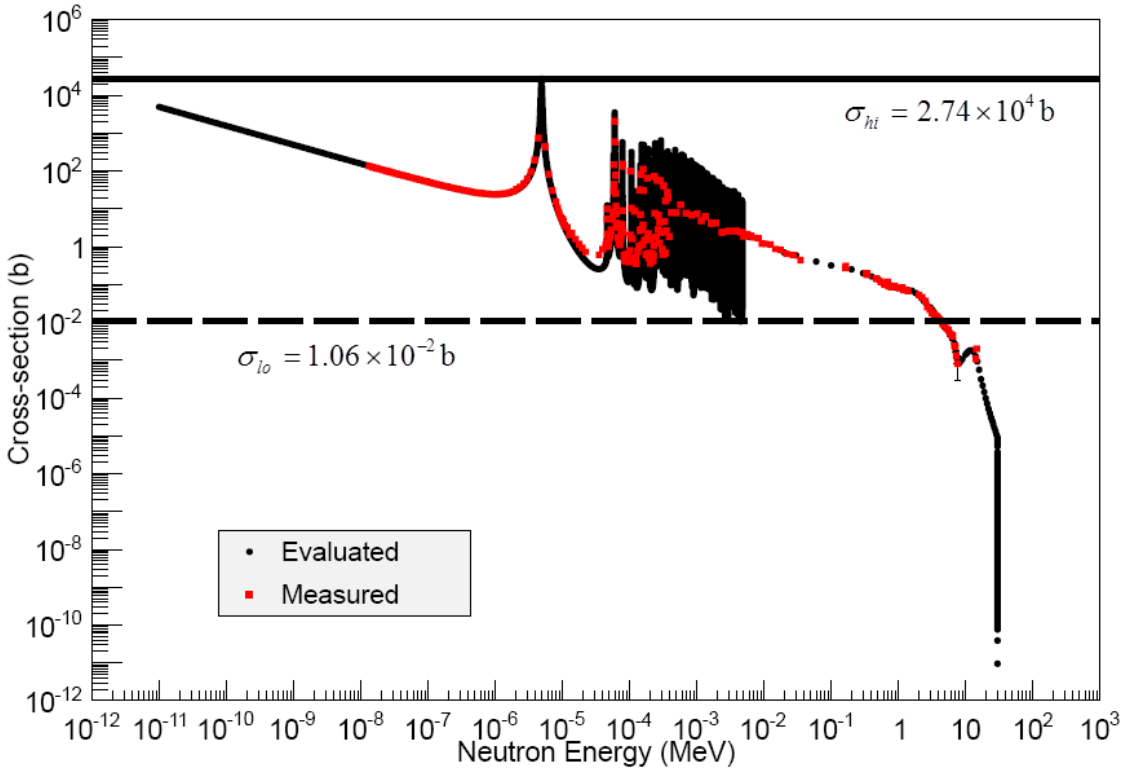

Figure B.3: Measured [10] and evaluated [125] cross sections for the reaction ^{197}Au(n,γ)^{198}Au. Error bars for the measured data points are shown; however, most of the error bars cannot be seen because they are smaller in size than the data points. For neutron energies less than 1.25 MeV, the highest evaluated cross section, σ_{hi}, and lowest evaluated cross section, σ_{lo}, are indicated with a solid line and a dotted line, respectively.

Appendix C

HPGe detector: manufacturer's schematic

A 115%, n-type HPGe detector was used to count the irradiated TeO_2 powder. The detector schematic provided by the manufacturer, ORTEC, is given in Figure C.1. Additional information on the copper contact pin is given in Table C.1.

Table C.1: Additional information on the copper contact pin from Figure C.1

Parameter	Value
Pin radius	3.175 mm
Pin length	78 mm
Pin material	Cu (60%), Zn (39.25%), Sn (0.75%)
Pin density	8.41 g/cm^3

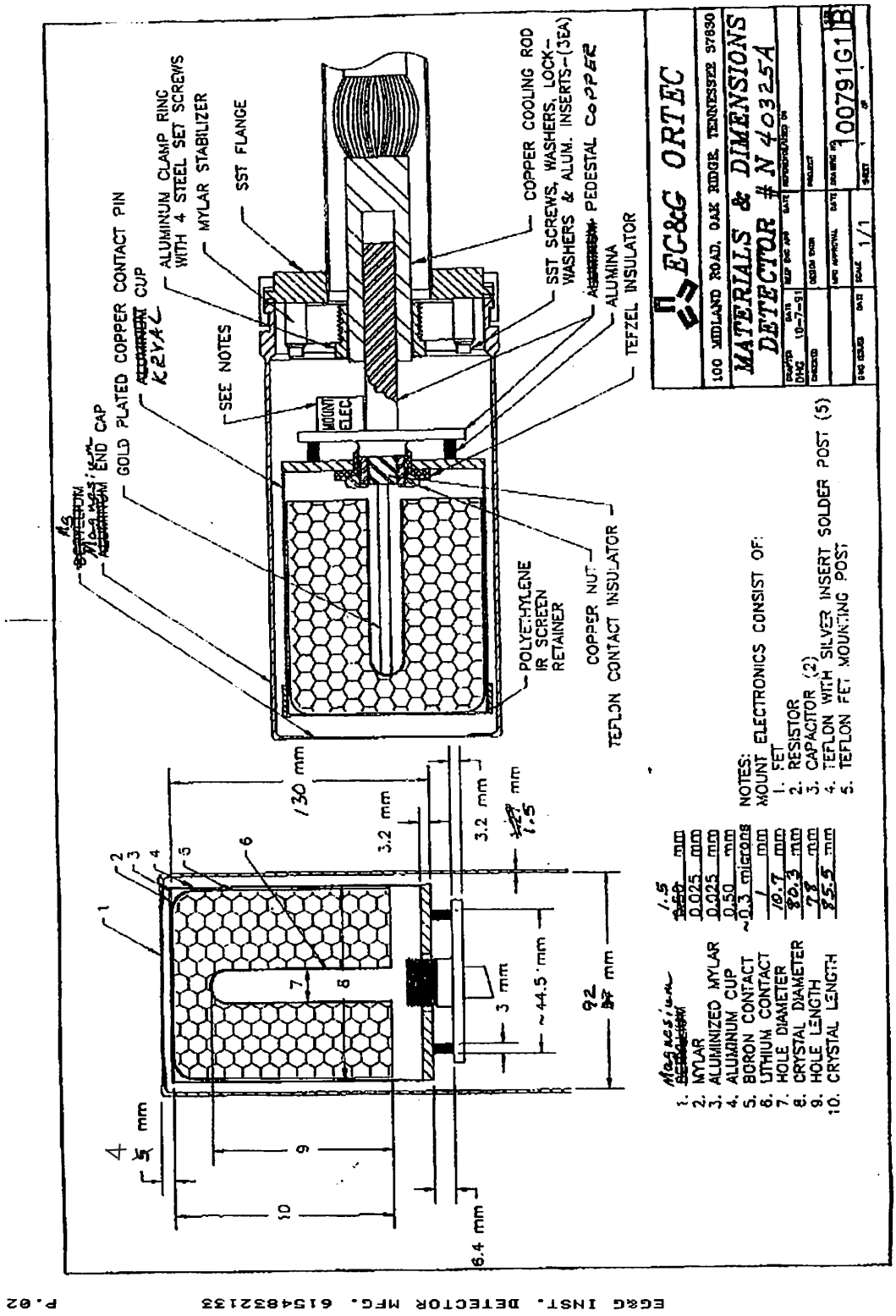

Figure C.1: Manufacturer's schematic of the 115%, n-type HPGe detector used to count the irradiated TeO_2 powder.

Appendix D

Gamma spectra used in analysis

Table D.1: Gamma spectra used in the cross-section analysis are listed below. Each spectrum's name is given in column one. The date gamma counting was begun and the live time of counting are provided in columns two and three.

Spectrum Name	Date Gamma Counting Started	Live Time (s)
27769	3/5/2012	3599.72
27804	3/16/2012	7199.94
28033	5/4/2012	89999.86
28229S	6/26/2012	254999.00

Table D.2: Gamma lines used to obtain the cross-sections for neutron activation of TeO_2. The activated isotopes are listed in column one. The branching ratios of the gamma lines and the gamma spectra used are provided in columns three and four. The gamma lines in this table are shown in Figures D.1 - D.23 and are indicated with red arrows.

Isotope	Gamma Energy (keV)	Branching Ratio (%)	Gamma Spectrum
^{118}Te	1229.33	2.5	27769
^{119m}Te	153.59	66(3)	27804
^{121m}Te	212.19	81.5	28229S
^{123m}Te	159	84	28229S
^{125m}Te	109.28	0.280(3)	28229S
^{127m}Te	417.9	0.99(14)	28229S
^{129m}Te	105.5	0.14(4)	28033
^{120m}Sb	1171.7	100	27804
^{122}Sb	564.24	70.67	27804
^{124}Sb	602.73	97.8(3)	28229S
^{125}Sb	427.87	29.6	28229S
^{126}Sb	720.7	53.8(24)	27804
^{127}Sb	473	25.8(16)	27804
^{113}Sn	391.70	64.97(17)	28229S
^{117m}Sn	156.02	2.113(12)	27804

Continued on next page

Table D.2 – continued from previous page

Isotope	Gamma Energy (keV)	Branching Ratio (%)	Gamma Spectrum
^{111}In	171.28	90.7(9)	27769
^{114m}In	190.27	15.56(15)	28229S
^{105}Ag	344.52	41.4	28229S
^{106m}Ag	450.98	28.2(7)	27769
^{110m}Ag	884.68	75.0(11)	28229S
^{111}Ag	342.13	6.7	27769
^{101m}Rh	306.86	81(4)	27769
^{7}Be	477.60	10.44(4)	28229S

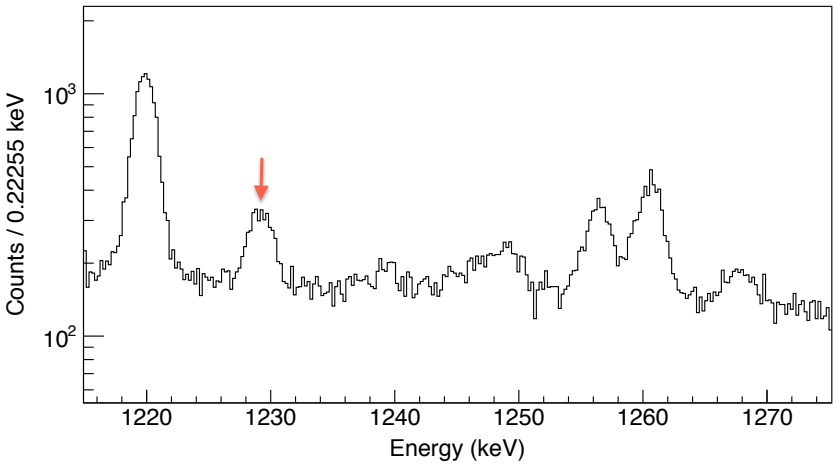

Figure D.1: ^{118}Te.

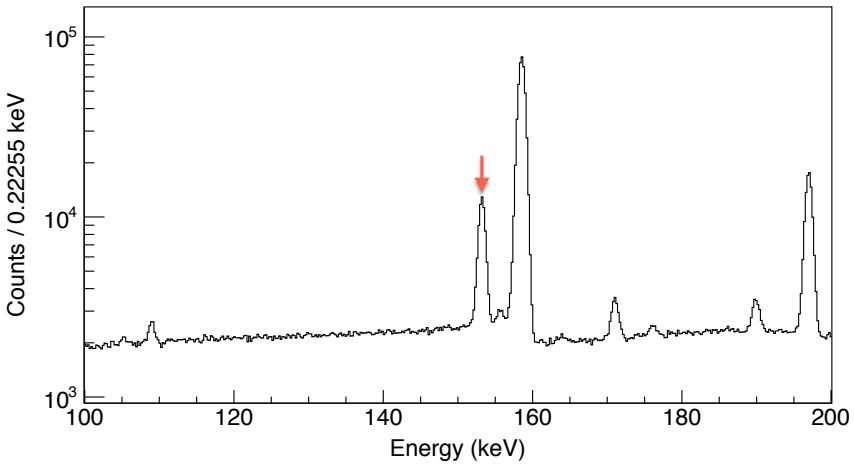

Figure D.2: ^{119m}Te.

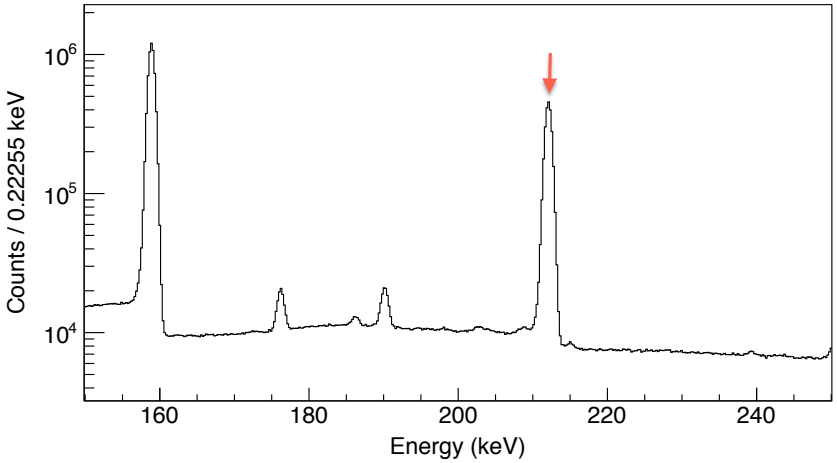

Figure D.3: ^{121m}Te.

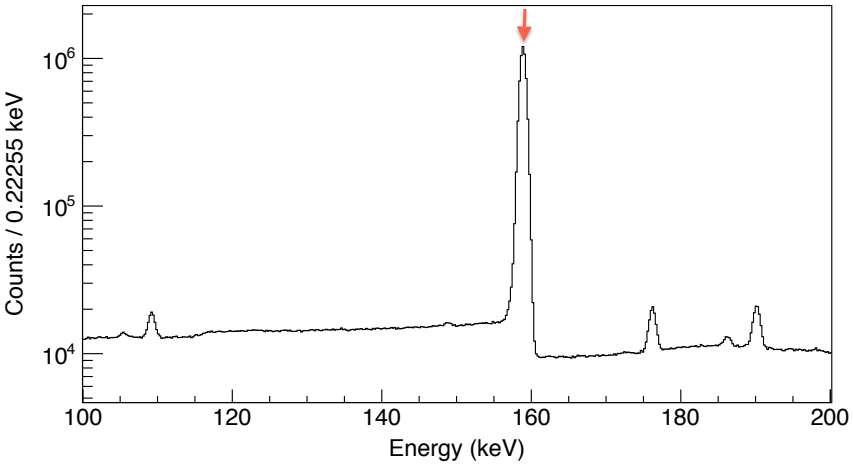

Figure D.4: ^{123m}Te.

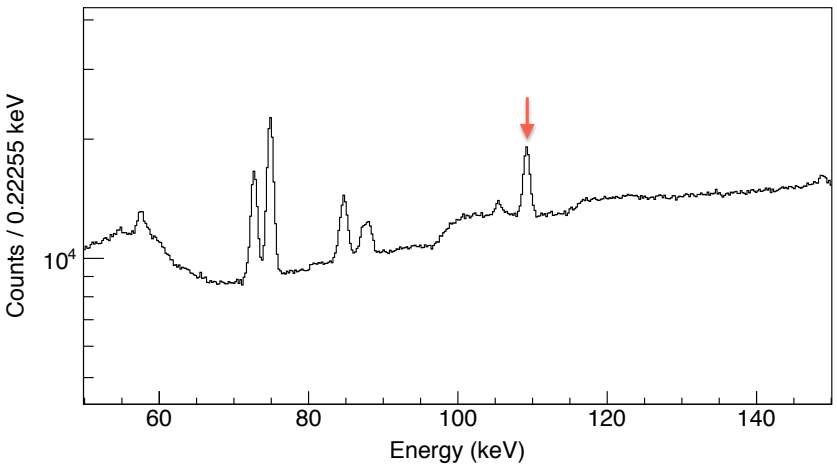

Figure D.5: ^{125m}Te.

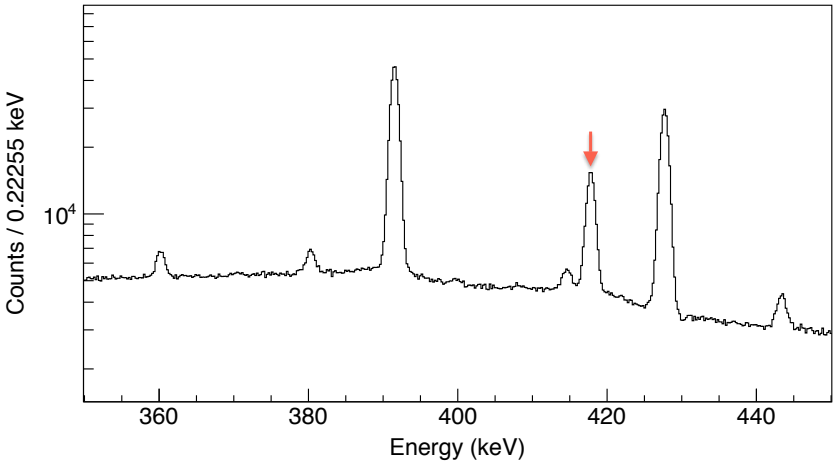

Figure D.6: ^{127m}Te.

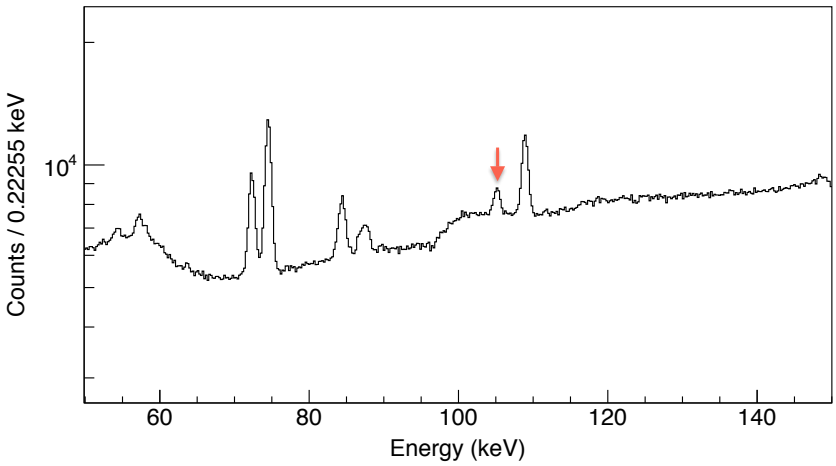

Figure D.7: ^{129m}Te.

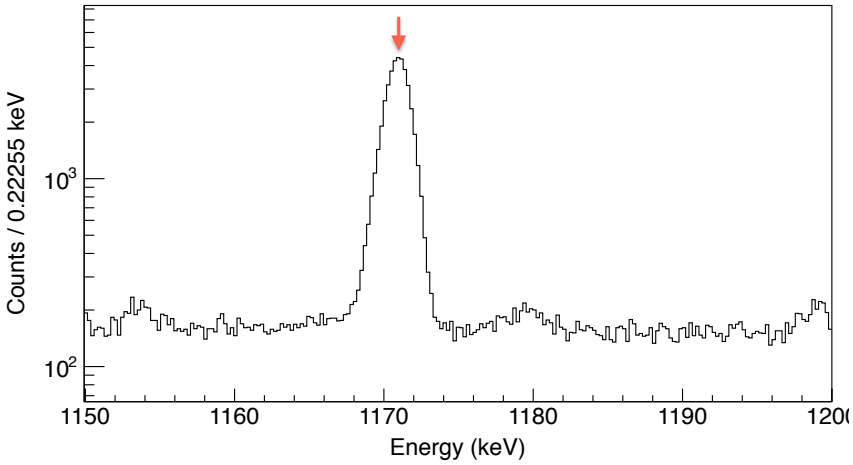

Figure D.8: ^{120m}Sb.

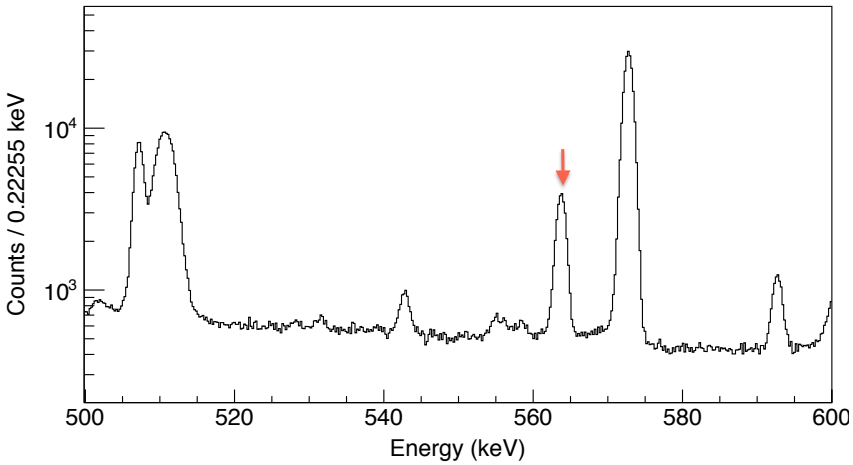

Figure D.9: ^{122}Sb.

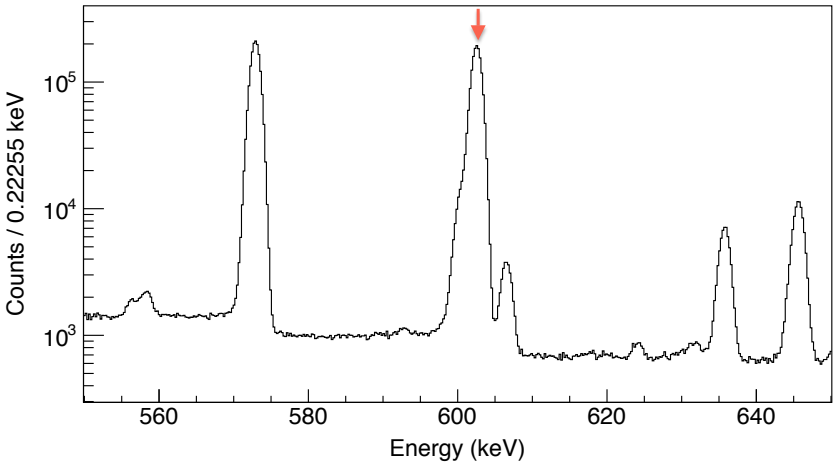

Figure D.10: ^{124}Sb.

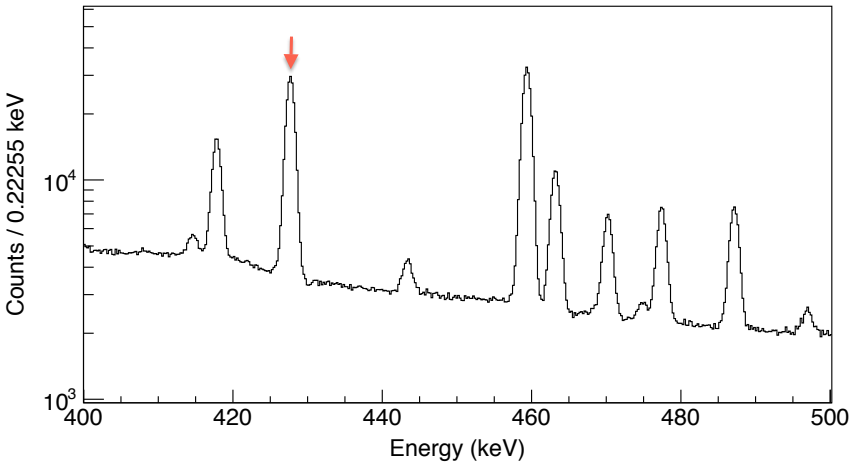

Figure D.11: ^{125}Sb.

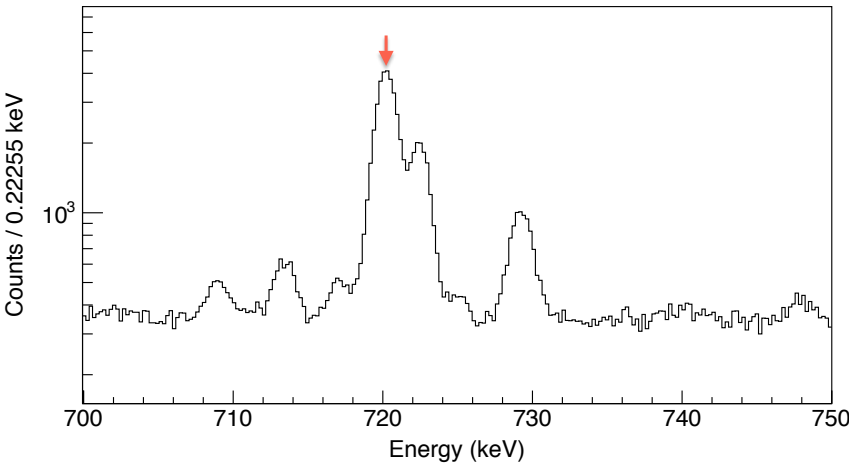

Figure D.12: ^{126}Sb.

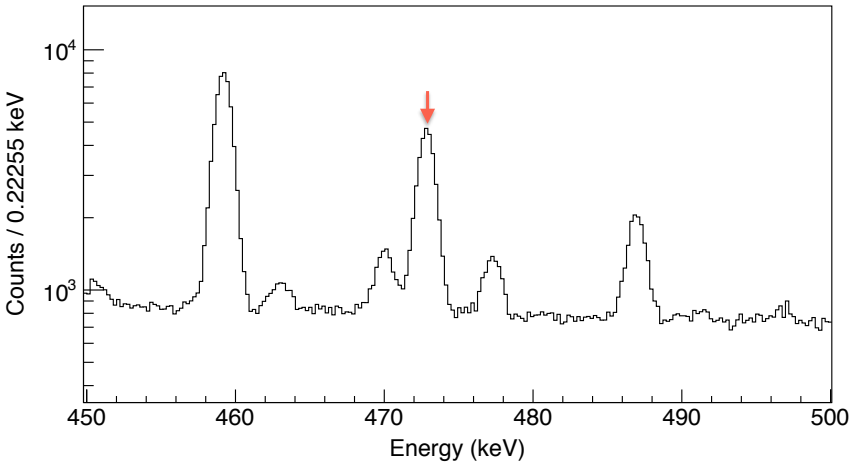

Figure D.13: ^{127}Sb.

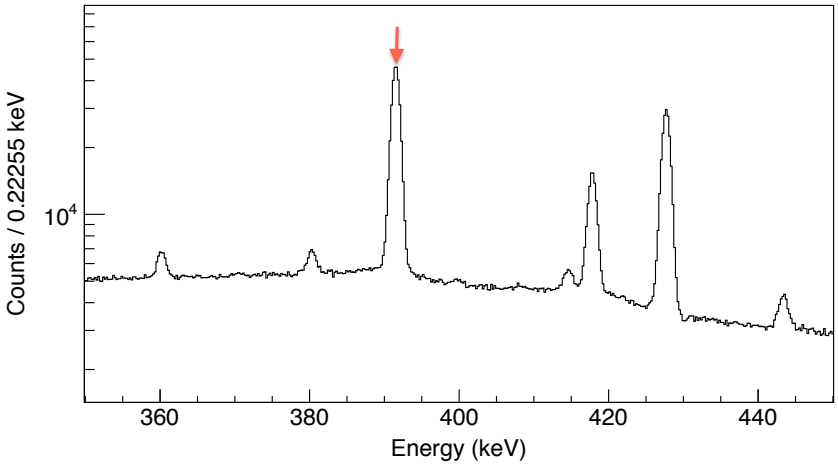

Figure D.14: ^{113}Sn.

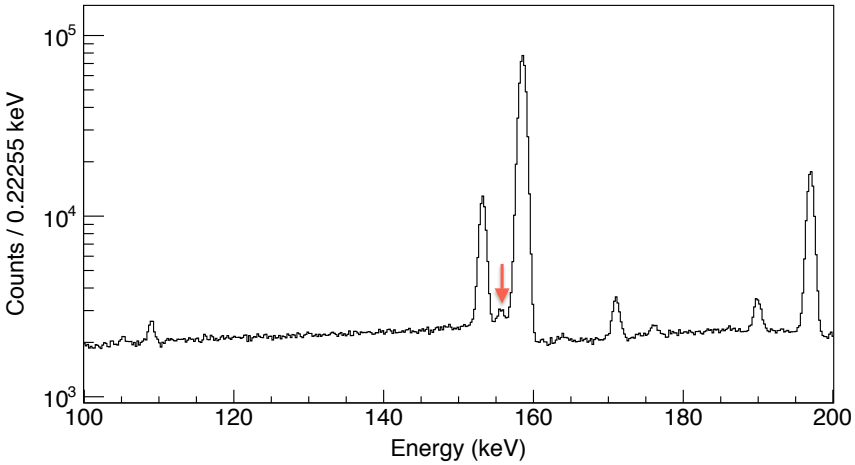

Figure D.15: ^{117m}Sn.

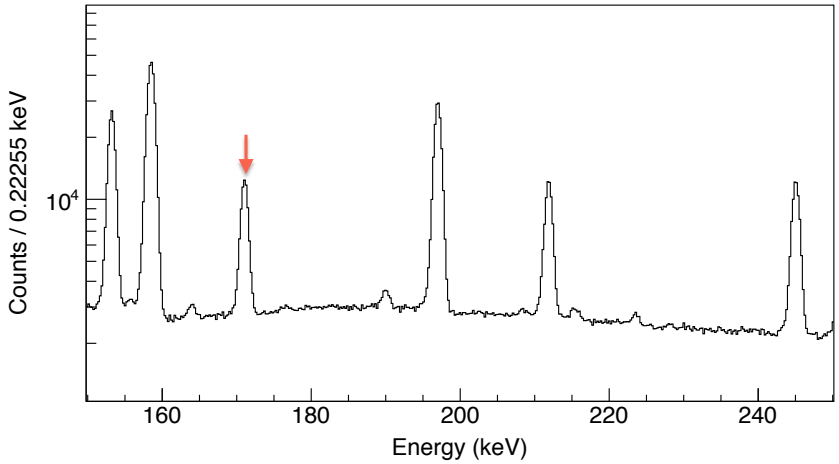

Figure D.16: ^{111}In.

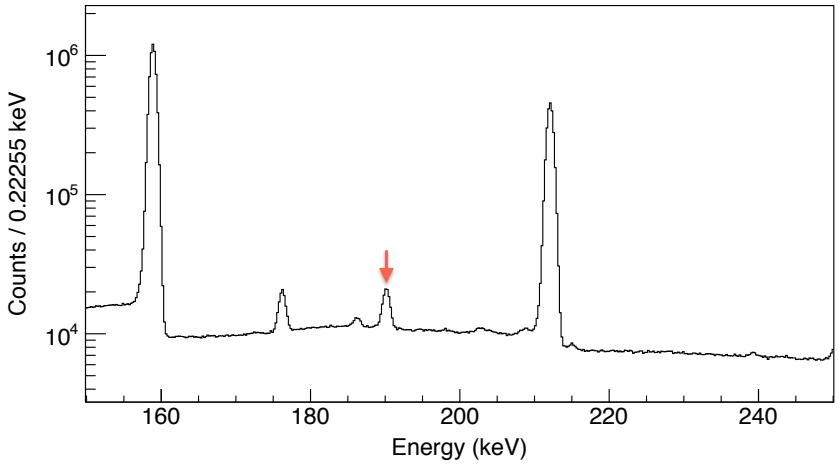

Figure D.17: ^{114m}In.

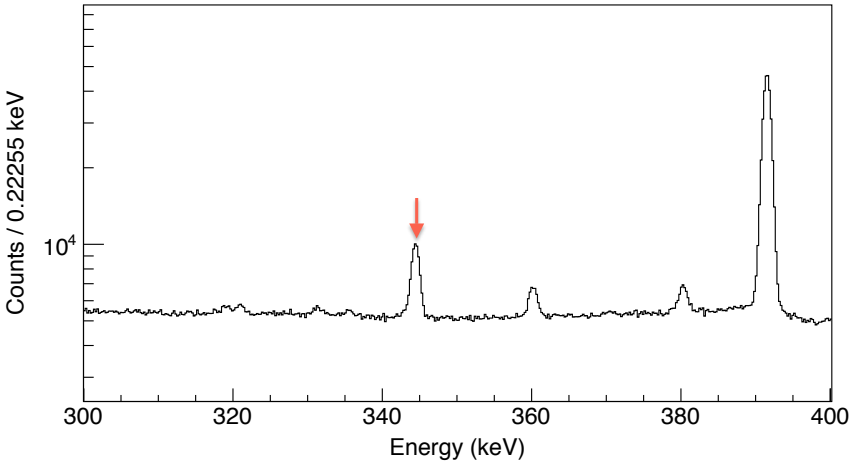

Figure D.18: ^{105}Ag.

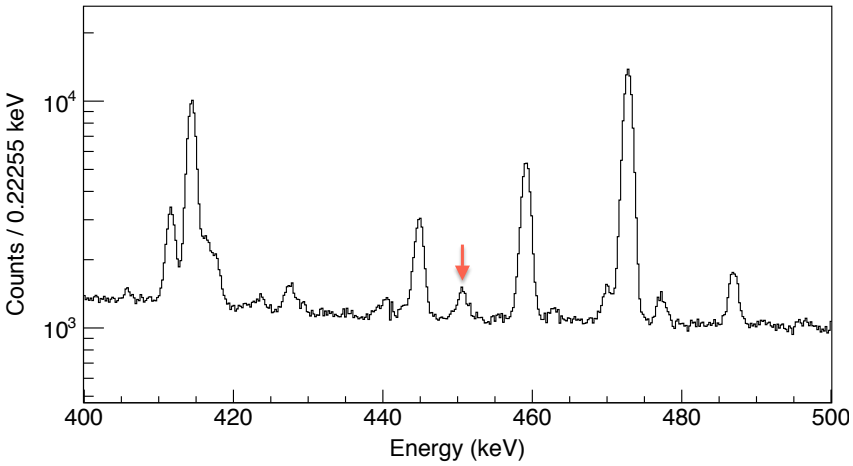

Figure D.19: ^{106m}Ag.

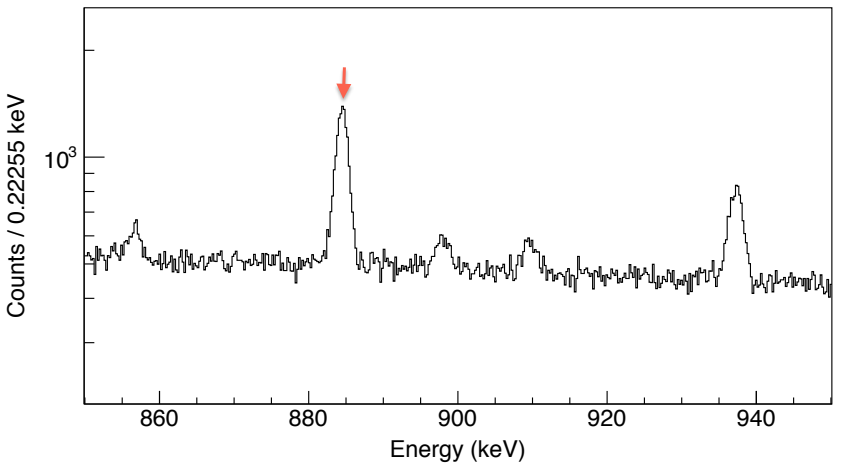

Figure D.20: ^{110m}Ag.

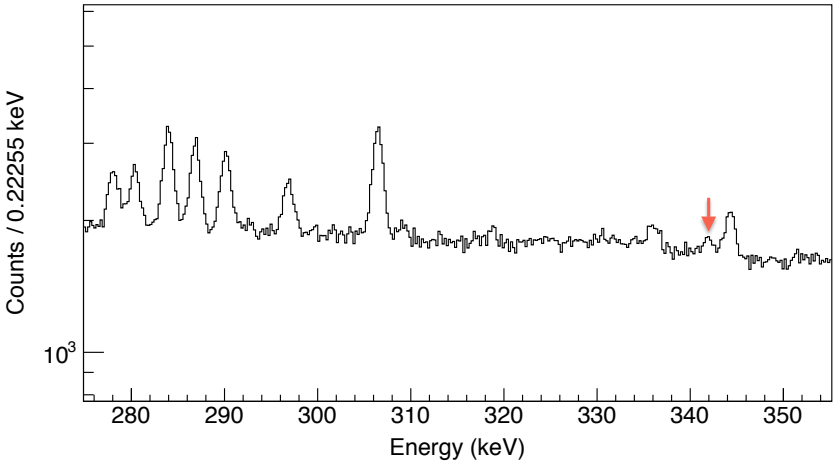

Figure D.21: ^{111}Ag.

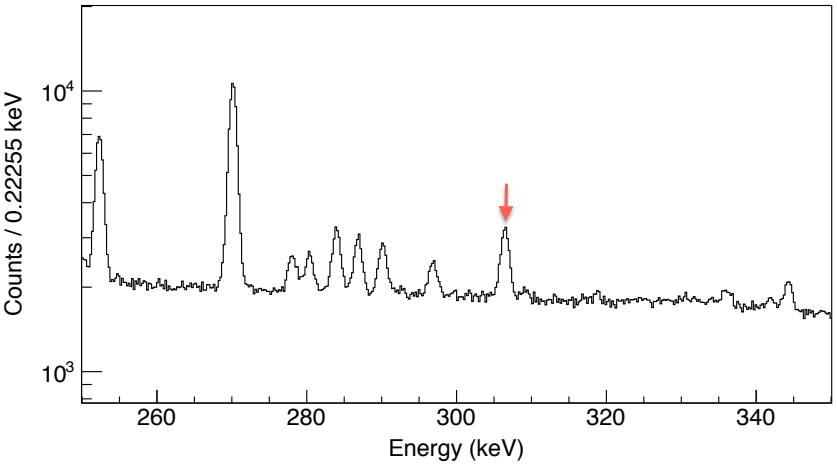

Figure D.22: ^{101m}Rh.

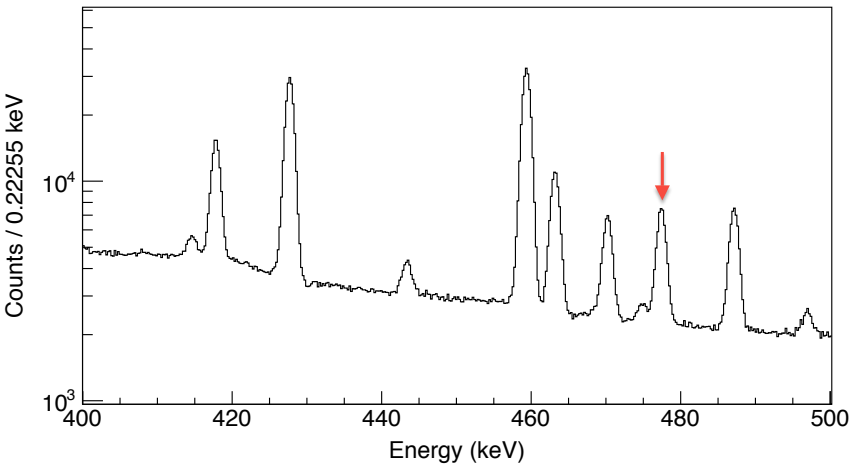

Figure D.23: ^{7}Be.